Links between Galaxy Structure and Stellar Populations

Tania Maria Barone

A thesis submitted for the degree of

Doctor of Philosophy

of the Australian National University

Australian National University

Research School of Astronomy & Astrophysics

June 2022

Although the Universe is under no obligation to make sense, students in pursuit of the PhD are.
– Robert Kirshner 1991

Disclaimer

I declare that the work in this thesis is that of the candidate alone, except where indicated below or in the text of the thesis. The work was undertaken between July 2017 and June 2022 at the Australian National University, Canberra. It has not been submitted in whole or in part for any other degree at this or any other university.

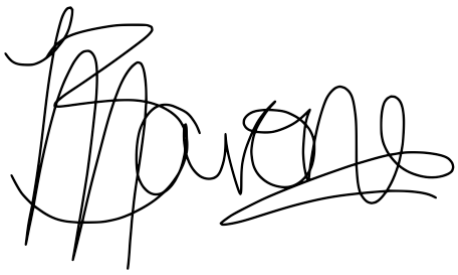

Tania Maria Barone

22nd June 2022

Acknowledgments

Firstly thank you to my supervisors Matthew Colless, Francesco D'Eugenio, Nic Scott and Scott Croom for been unwavering in your support, guidance, and compassion throughout this whole journey. Thank you for encouraging my curiosity and independence while ensuring I stayed on course.

I am extremely lucky to have spent time during my PhD within two departments, and have always felt welcomed and a part of both communities. In particular, I'm thankful for the strong sense of belonging to our research group (*"Matthew's Minions"*), thanks to fellow minions Dilyar, Francesco, Khaled and Sree.

I am incredibly grateful for my family, who have always been supportive and proud of my goals and achievements. A special mention to my brother Thomas, who had the original idea at 8 years old to become an astronomer. Not having a better idea myself at the time age 9, I co-opted yours. I still remember the interest and wonder I felt reading your astronomy books, which undoubtably helped lead me to where I am today.

Lastly, to Sam. For your belief in me even when my self-belief wavered.

Abstract

In this thesis we analyse the observational relations between galaxy structure and global stellar population properties to determine the dependencies between a galaxy's star formation and mass assembly histories. Stellar population parameters correlate with a range of galaxy properties, but it is unclear which relations are causal and which are the result of another underlying trend. The well-established correlations between mass and other galaxy properties are often considered evidence for mass driving a galaxy's evolution. However, we find that, at fixed mass, stellar population properties show significant dependence on size, indicating that the size of a galaxy is also an important property tracing, and possibly influencing, its evolution. The focus of the thesis is to quantitatively compare trends between various stellar population properties and key galaxy structural parameters — in particular the galaxy's mass (M), gravitational potential ($\Phi \propto M/R$) and surface density ($\Sigma \propto M/R^2$) — in order to determine which relations are intrinsically tighter and are therefore more likely to reflect a causal relation. We divide our work into three parts focusing on early-type galaxies, star-forming galaxies and intermediate-redshift galaxies, respectively. This division reflects both the physical differences between these samples, as well as technical differences in measuring their stellar population properties.

We start by analysing a sample of 625 early-type galaxies (ETGs) with integral field spectroscopy from the SAMI galaxy survey. We show that, compared to correlations with mass, broadband optical $g-i$ colour and mean stellar metallicity [Z/H] correlate more strongly with gravitational potential, while mean stellar age correlates best with surface density. Specifically, the $g-i$–Φ, [Z/H]–Φ, and age–Σ relations show both lower scatter and smaller residual trends with galaxy size than other relations do. For [α/Fe], a proxy for star formation duration, we find comparable results for Φ and Σ, with both being significantly stronger correlations than the [α/Fe]–M relation. Taken together, these results lead us to the following inferences and interpretations. First, we concur with previous studies in finding that gravitational potential is the primary regulator of global stellar metallicity by determining the escape velocity required for metal-rich stellar and supernova ejecta to escape the system and avoid being recycled into later stellar generations. Second, to explain the age and [α/Fe] correlations with Σ, we propose two possible mechanisms: (a) the correlations arise as results of compactness-driven quenching mechanisms, and/or (b) as fossil records of the $\Sigma_{\rm SFR} \propto \Sigma_{\rm gas}$ relation in their disk-dominated progenitors.

In order to test these conclusions, we studied the ages and metallicities of 2085 star-forming galaxies (SFGs) from the SDSS Legacy survey. By investigating whether these scaling relations are also present in earlier phases of galaxy evolution, we narrow the range of possible physical mechanisms responsible for producing them. As with the trends found in ETGs, we find that in SFGs age correlates best with surface density and [Z/H] correlates best with gravitational potential. Importantly, showing that the age–Σ relation exists in star-forming galaxies demonstrates it must originate *before* quenching. We conclude that the age–Σ relation is consistent with compact galaxies forming earlier, perhaps driven by higher gas fractions in the early Universe causing older galaxies to form more compactly during their *in-situ* formation phase.

Lastly we investigate the change in stellar age and metallicity scaling relations for quiescent

galaxies from intermediate redshift ($0.60 \leq z \leq 0.76$), using the LEGA-C survey, to low redshift ($0.04 \leq z \leq 0.11$), using the SAMI survey. We find that, as for their low-redshift counterparts, the stellar metallicity of quiescent galaxies at $0.60 \leq z \leq 0.76$ closely correlates with the depth of the gravitational potential. This supports the hypothesis that the relation arises because the gravitational potential regulates the escape velocity of metal-rich gas. On the other hand, we find no correlation between stellar age and surface density in the intermediate-redshift sample, despite there being a strong relation at low redshift. We consider this change in the age–Σ relation in the context of the redshift evolution of the star-forming and quiescent populations in the mass–size plane and find our results can be explained as a consequence of galaxies forming more compactly at higher redshift, and remaining compact throughout their evolution. In particular, galaxies appear to quench above a characteristic surface density threshold that decreases with decreasing redshift. The age–Σ relation at $z \sim 0$ results from the build-up of the quiescent and star-forming populations from galaxies that formed over a range of redshifts and therefore with a range of surface densities.

Contents

List of Figures

List of Tables

List of Publications

First Author

The LEGA-C and SAMI Galaxy Surveys: Quiescent Stellar Populations and the Mass-Size Plane across 6 Gyr
Barone, Tania M.; D'Eugenio, Francesco; Scott, Nicholas; Colless, Matthew; and 21 others.
2022, *Monthly Notices of the Royal Astronomical Society*, ADS

Gravitational Potential and Surface Density Drive Stellar Populations – II. Star-Forming Galaxies
Barone, Tania M.; D'Eugenio, Francesco; Colless, Matthew; Scott, Nicholas.
2020, *The Astrophysical Journal*, ADS

The SAMI Galaxy Survey: Gravitational potential and surface density drive stellar populations–I. early-type galaxies
Barone, Tania M.; D'Eugenio, Francesco; Colless, Matthew; Scott, Nicholas; and 14 others.
2018, *The Astrophysical Journal*, ADS

Co-Author

The MAGPI Survey – science goals, design, observing strategy, early results and theoretical framework
Foster, C.; Mendel, J. T.; Lagos, C. D. P.; Wisnioski, E.; Yuan, T.; D'Eugenio, F.; **Barone, T. M.**; and 36 others.
2021, *Publications of the Astronomical Society of Australia*, ADS

The SAMI Galaxy Survey: the third and final data release
Croom, Scott M.; Owers, Matt S.; Scott, Nicholas; Poetrodjojo, Henry; Groves, Brent; van de Sande, Jesse; **Barone, Tania M.**; and 34 others.
2021, *Monthly Notices of the Royal Astronomical Society*, ADS

The SAMI Galaxy Survey: Stellar Populations of Passive Spiral Galaxies in Different Environments
Pak, Mina; Oh, Sree; Lee, Joon Hyeop; Scott, Nicholas; Smith, Rory; van de Sande, Jesse; Croom, Scott M.; D'Eugenio, Francesco; Bekki, Kenji; Brough, Sarah; Foster, Caroline; **Barone, Tania M.**; and 8 others.
2021, *The Astrophysical Journal*, ADS

Inverse stellar population age gradients of post-starburst galaxies at z = 0.8 with LEGA-C
D'Eugenio, Francesco; van der Wel, Arjen; Wu, Po-Feng; **Barone, Tania M.**; and 12 others.
2020, *Monthly Notices of the Royal Astronomical Society*, ADS

The SAMI galaxy survey: stellar population radial gradients in early-type galaxies
Ferreras, Ignacio; Scott, Nicholas; La Barbera, Francesco; Croom, Scott; van de Sande, Jesse; Hopkins, Andrew; Colless, Matthew; **Barone, Tania M.**; and 11 others.
2019, *Monthly Notices of the Royal Astronomical Society*, ADS

The SAMI Galaxy Survey: Data Release Two with absorption-line physics value-added products
Scott, Nicholas; van de Sande, Jesse; Croom, Scott M.; Groves, Brent; Owers, Matt S.; Poetrodjojo, Henry; D'Eugenio, Francesco; Medling, Anne M.; Barat, Dilyar; **Barone, Tania M.**; and 27 others.
2018, *Monthly Notices of the Royal Astronomical Society*, ADS

The gas-phase metallicities of star-forming galaxies in aperture-matched SDSS samples follow potential rather than mass or average surface density
D'Eugenio, Francesco; Colless, Matthew; Groves, Brent; Bian, Fuyan; **Barone, Tania M.**
2018, *Monthly Notices of the Royal Astronomical Society*, ADS

CHAPTER 1

Introduction

1.1. Ancient and Early Astronomy

Astronomy has existed for as long as humans and our ancestors have observed and contemplated the night sky. Astronomy has particular cultural significance in Australia, with Indigenous Australians being among the earliest astronomers to observe and maintain knowledge, through oral tradition, of a range of subtle and rare astronomical phenomena, including pulsating and varying stars (Hamacher & Frew 2010; Hamacher 2018), the movement of the planets (Hamacher & Banks 2018), eclipses (Hamacher & Norris 2011b), comets (Hamacher & Norris 2011a), and meteors (Hamacher & Norris 2010). Beyond the solar system and solar neighbourhood, Indigenous knowledge also included the Milky

Way, Magellanic clouds, and Andromeda (see Norris 2016 and references therein). This knowledge not only served an immediate practical benefit by, for example, predicting tides based on lunar phases (Berndt 1948), aiding with navigation (Norris 2016), and forecasting meteorological changes based on stellar scintillation (Hamacher et al. 2019), but also formed an integral part of Aboriginal spirituality and culture (see Norris & Hamacher 2015 for an overview)[1]. Similarly, this influence of astronomy on science, religion, philosophy, and spirituality is found in many, if not all, early cultures around the world (see e.g Selin & Sun 2000). It is clear that curiosity about the world and our place within it is a common and uniting thread throughout human history.

Over the last 500 years, our concept of the extent of the Universe has grown monumentally, with each paradigm shift symbolic of both broader cultural and scientific change. In Europe, the geocentric model of Greek, Roman and Egyptian antiquity, attributed to Aristotle and Ptolemy, was gradually superseded in the late 16th and early 17th century by the heliocentric model, championed and underpinned by the work of Copernicus, Brahe, Kepler, and Galileo[2]. The next significant paradigm shift came in the late 1600s with Newton's laws of gravity (Newton 1687). Newton's work revolutionised celestial mechanics, by showing for the first time that planetary motions can be explained using the same laws of physics experienced on Earth and providing a mathematical model for gravity that could be applied to other phenomena, such as tides. Another key moment in astronomy history came in the 1800s, when for the first time accurate distances to nearby stars were measured using the parallax method (Bessel 1838). These distances indicated stars have comparable intrinsic brightness to the sun but are simply much further away, extending our understanding of the Universe to beyond our own solar system. However, the concept of galaxies other than our own, and the distinction between the Galaxy and the Universe, didn't gain mainstream attention until the early 1900s. At this time, the nature of spiral galaxies was fiercely contested (The Great Debate; Shapley & Curtis 1921), with rival explanations as either nebulae situated within our own Galaxy ('spiral nebulae'; Shapley & Shapley 1919), or distant independent galaxies ('island universes'; Curtis 1917). By measuring the distance to the Andromeda galaxy using Cepheid variables, Hubble (1929b) settled the debate and firmly established spiral 'nebulae' as distant, independent galaxies. Since this symbolic beginning of extra-galactic astronomy, we now understand that our Milky Way is but a single fairly typical, though individual, (e.g. Boardman et al. 2020) example of the >500 million galaxies so far observed (Abbott et al. 2021). These discoveries set the stage for the next wave of key astrophysical discoveries regarding the composition and nature of the Universe itself.

[1] Due to the significant cultural loss as a result of European arrival in 1788, current ethnographic research into Indigenous Australian traditions is still recovering vast, previously unwritten historical knowledge (Norris & Hamacher 2015).

[2] Although Aristarchus of Samos proposed the heliocentric model in the 3rd century BC, it was rejected by his contemporaries in favour of the geocentric model (Kish 1978).

1.2. Galaxies and Cosmology

1.2.1. The Flat ΛCDM Universe

During the 1900s our understanding of the nature and physics of the Universe developed rapidly and substantially, eventually leading to our current physically-motivated mathematical model. The flat ΛCDM universe has three key elements summarised in its name: (i) it has Euclidean geometry on cosmological scales ('flat'); (ii) it is expanding at an accelerating rate ('Λ'); and (iii) it has matter content dominated by cold (non-relativistic), dark (electromagnetically non-interacting) matter ('CDM').

The theory of an expanding rather than static (e.g. Einstein 1917) universe was formalised independently by Friedmann (1924), Lemaître (1927), Robertson (1928) and Walker (1937), as solutions to the recently developed field equations of the General Theory of Relativity formulated by Einstein (1916). Their hypothesis was supported by the results of Hubble (1929a) who noticed a relation between the distance and the recessional velocity of galaxies. Lemaître (1931) and Gamow (1946) further proposed our expanding Universe originated in a Big Bang, however the strongest piece of observational evidence supporting this theory only came with the incidental discovery of the cosmic microwave background (CMB) radiation by Penzias & Wilson (1965). The accelerating aspect of this expansion was later discovered independently by Riess et al. (1998) and Perlmutter et al. (1999), when both teams used the standard luminosity of Type Ia supernova to measure the redshift–distance relation for distant galaxies. This accelerated expansion is conventionally explained by the presence of 'dark energy', parameterised by a non-zero cosmological constant Λ in Einstein's field equations.

Key studies leading to the hypothesis of cold dark matter include analyses of cluster dynamics and of galaxy rotation curves. Zwicky (1937) studied galaxy velocities in the Coma cluster and found that the mass of the cluster inferred from the virial theorem is significantly higher than the observed total stellar mass. He concluded that most of the matter in the cluster is dark rather than luminous. Further observational evidence for the existence of dark matter came from the shape of galaxy rotation curves out to large radii, which cannot be explained solely by the observed luminous matter (Freeman 1970; Rubin & Ford 1970). The scale at which dark matter forms halos is indicative of its temperature, providing additional constrains on cosmological models. Dark matter, by definition, does not interact with photons and therefore cannot radiatively cool. Therefore, the extent to which a dark matter cloud can condense due to gravity is limited by the kinetic energy (temperature) of its constituent particles. The smallest observed dark matter structures are on the scale of dwarf galaxies (Strigari et al. 2008). This rules out hot (relativistic) and warm (semi-relativistic) dark matter, leaving cold (non-relativistic) dark matter as the most likely candidate (e.g. Bertone & Tait 2018).

The last crucial piece of the puzzle is the geometric curvature of the Universe, which determines whether it is flat (in the case of zero curvature), open (negative curvature), or closed (positive curvature). While observations of large-scale galaxy clustering supported a flat universe model (e.g. Percival et al. 2001), the strongest constraints on this flatness come from observations of the temperature fluctuations of the CMB, first by the Cosmic

Background Explorer (COBE; Smoot et al. 1992), then the Wilkinson Microwave Anisotropy Probe (WMAP; Bennett et al. 2003) and further refined most recently by the Planck satellite (Planck Collaboration et al. 2020a). These CMB observations, combined with observations of large-scale structure (notably the baryon acoustic oscillations), constrain the Universe to be flat (have a curvature of zero) to within 0.4% (Planck Collaboration et al. 2020a).

While there remain innumerable unanswered questions, the combination of all these key studies have lead to a succinct, physically-motivated, mathematical model of a flat universe expanding under the influence of dark energy and containing cold dark matter (flat ΛCDM). Although there is tension surrounding the precise values of some key cosmological parameters depending on the method used to measure them (Riess et al. 2019; Planck Collaboration et al. 2020a; Said et al. 2020), fortunately most galaxy evolution studies, including those presented here, are insensitive to this level of imprecision in the cosmological model. Throughout the work presented here we adopt current standard practice within the galaxy evolution community and use a cosmological model where the fraction of the total energy of the Universe in dark energy is $\Omega_\Lambda = 0.7$, the fraction in both dark and ordinary matter is $\Omega_M = 0.3$, and the Hubble constant is $H_0 = 70\,\mathrm{km\,s^{-1}\,Mpc^{-1}}$.

1.2.2. Galaxy Formation

In the flat ΛCDM paradigm the formation of galaxies is primarily a consequence of quantum fluctuations in the early Universe and the attractive force of gravity. In this model the Universe formed in the Big Bang 13.8 billion years ago, followed by a period of rapid inflation (Guth 1981; Linde 1982; Planck Collaboration et al. 2020b). Quantum fluctuations that existed when inflation began were amplified to cosmic scales by the rapidly expanding Universe and led to large-scale variations in the density distribution of matter, of which 84% is dark matter (Planck Collaboration et al. 2020a)[3]. It was these large-scale dark matter density variations that provided the foundations from which the first galaxies formed. As matter (both dark and ordinary) attracts due to self-gravity, initial over-densities become amplified as additional matter is attracted from nearby under-dense regions. Therefore the initial density fluctuations in the matter distribution become amplified over time, leading to over-dense sheets, filaments and clusters, and under-dense voids, in what is known as the 'cosmic web' (e.g. Peacock et al. 2001). While dark matter was forming halos and large-scale structure, ordinary matter was in thermal equilibrium with the surrounding high-energy photons, preventing it from gravitationally condensing. As the Universe continued to expand, interactions between ordinary matter and photons decreased, eventually leading to matter and radiation falling out of thermal equilibrium in a process known as 'decoupling'. By decoupling from the surrounding radiation (that now forms the CMB; Hinshaw et al. 2009) the ordinary matter was able to cool and coalesce in the deep gravitational potential wells of the dark matter halos (Navarro et al. 1996). Unlike dark matter, ordinary matter can radiatively cool and so gas clouds were able to continue to condense further than the dark matter halos and gravitationally collapse to form the first stars. While many aspects of how the first galaxies formed remain unclear, including such major components as supermassive black holes (Kormendy & Ho 2013), the broadly-accepted formation scenario is

[3]These pre-inflation quantum fluctuations are also imprinted in the temperature variations of the CMB (e.g. Tegmark et al. 2006)

that individual star-forming gas clouds merged together within the dark matter structures, forming gravitationally-bound, galaxy-sized structures of stars and gas situated within dark matter halos (White & Rees 1978).

1.2.3. Galaxy Evolution

A galaxy's evolution is influenced by a wide range of internal and external processes, many of which interrelate. The strength and effect of external processes is determined predominantly by the galaxy's environment. Such processes include inflows of pristine gas from the cosmic web (Dekel et al. 2009), tidal torques (Doroshkevich 1970; White 1984), interactions and mergers with neighbours and satellites (Moore et al. 1996), and ram-pressure gas removal and the cutting-off of cold gas inflows as a result of infall to a group or cluster (Gunn & Gott 1972). On the other hand, the effect of internal processes is much more strongly dependent on the properties of the galaxy itself, such as mass and rotation. Internal processes include star formation, the injection of energy and momentum into the surrounding interstellar medium from supernovae (McKee & Ostriker 1977), active galactic nuclei (AGN; Brüggen & Kaiser 2002), stellar winds in strongly star-forming regions (Ceverino & Klypin 2009), and stellar migration due to the presence of bars and gravitational instabilities (Sellwood & Binney 2002). Given the stochastic nature and timescales of millions to billions of years of these processes, it is incredibly difficult to determine the precise combination of processes that acted over the history of any particular galaxy, leading to how we observe it today. Therefore, rather than trying to map the detailed evolutionary path of a single galaxy, we investigate the overall impact of different mechanisms by using large, representative samples and analysing how galaxy populations as a whole evolve across redshift.

While galaxies show a wide diversity of properties, at low redshift they can be loosely separated into two categories. Early-types are in general quiescent, bulge-dominated, have little cold gas content and old, metal-rich stars. Late-types are still star-forming, tend to be disk-dominated, have significant interstellar gas and young, metal-poor stars. While there are exceptions to each of these descriptors, e.g. rejuvenated early-types (Thomas et al. 2010; Chauke et al. 2019), quiescent disks (van den Bergh 1976; Pak et al. 2021), and 'transitional' galaxies that cannot be neatly categorised, this dichotomy represents well the overall low-redshift population. A major focus of galaxy evolution studies is identifying the mechanisms and processes responsible for the significant transformation in stellar population, morphology, kinematics, and gas properties, as a galaxy evolves from its 'main-sequence' late-type phase, characterised by stellar mass buildup via star formation, to the quiescent early-type phase. In particular, it is unclear how the transition from star-forming to quiescent correlates with differences in kinematics and structure. Thus a crucial tool for studying galaxy evolution is analysis of the connection between star-formation history and structural/dynamical changes.

By comparing the local Universe with high-redshift galaxy populations, studies have shown that the dominant processes influencing galaxy evolution must change with time (e.g. Barro et al. 2013). Galaxies observed at $z \sim 0.7$ (7 Gyr lookback time) are remarkably different to those observed in the local Universe, as well as having some features in common (e.g. Stott et al. 2016; van der Wel et al. 2016; Wisnioski et al. 2019). Compared to nearby galaxies at fixed stellar mass, at intermediate redshifts ($z \sim 1$–3) galaxies are more compact (Ferguson

et al. 2004; Trujillo et al. 2007; Buitrago et al. 2008; Williams et al. 2010; van der Wel et al. 2014; Mowla et al. 2019), more highly star-forming (with a peak in star formation at $z \approx 2$; Lilly et al. 1996; Madau et al. 1998; Daddi et al. 2007; Madau & Dickinson 2014), have dynamically hotter turbulent gas (Förster Schreiber et al. 2006; Weiner et al. 2006; Law et al. 2007; Förster Schreiber et al. 2009; Law et al. 2009; Wright et al. 2009; Wisnioski et al. 2011; Epinat et al. 2012; Swinbank et al. 2012; Kassin et al. 2012; Wisnioski et al. 2015), and have higher molecular gas fractions (Tacconi et al. 2010; Daddi et al. 2010; Tacconi et al. 2013; Morokuma-Matsui & Baba 2015). However, a significant issue affecting comparisons of low- and high-redshift populations is sample bias: galaxies at greater distances appear fainter, and so at high redshift we are only able to observe the most massive and brightest galaxies, which can lead to a mischaracterisation of the population as a whole (Malmquist 1922). However, with careful consideration of selection effects and the resulting sample bias, galaxy evolution studies have led to a broad evolutionary scenario referred to as the 'two-phase build-up' of galaxies.

In the two-phase build-up scenario (e.g. Oser et al. 2010), the initial phase is characterised by rapid in-situ star formation at $z \gtrsim 2$ followed by a comparatively extended slow build-up by ex-situ accretion from $z \lesssim 3$. The two-phase build-up scenario successfully explains the broad features of galaxies at high redshift and the dichotomy of galaxies at low redshift. The peak of the cosmic star-formation rate occurred at $z \approx 2$ (Madau & Dickinson 2014), up to which time galaxies underwent a rapid build-up via in-situ star formation, producing highly star-forming, compact galaxies (e.g. Cimatti et al. 2008; van Dokkum et al. 2008; van der Wel et al. 2008). Following this rapid star-forming phase, these compact galaxies continued to evolve via frequent minor and occasional major mergers (e.g. Oser et al. 2010; Barro et al. 2013; Rodriguez-Gomez et al. 2016; Wellons et al. 2016). Compared to minor mergers, which significantly increase a galaxy's half-light radius but contribute little to its overall stellar mass, major mergers significantly increase both the mass and size of the merged galaxy (Naab et al. 2009; Bezanson et al. 2009; van Dokkum et al. 2010), leading to the massive, quiescent population observed at low redshift. This two-phase evolutionary scenario also provides an explanation for the large sizes of low-redshift star-forming galaxies compared to their quiescent counterparts at fixed mass (Kriek et al. 2009; Williams et al. 2010; Wuyts et al. 2011; van der Wel et al. 2014; Whitaker et al. 2017). In this framework, today's star-forming galaxies underwent a less rapid form of this evolutionary scenario, because they formed a significant portion of their stellar mass after the cosmic star-formation rate peaked at redshift $z \approx 2$, after which the balance between gas accretion and feedback processes led to comparatively lower star-formation rates (Madau & Dickinson 2014). As a consequence of forming later, their in-situ build-up phase was less rapid, leading to less-compact galaxies compared to the progenitors of today's quiescent population. Therefore, low-redshift star-forming galaxies are expected to evolve into quiescent galaxies that are, on average, larger than the current population of early-types (Barro et al. 2013). While this two-phase build-up formation scenario explains broad features of galaxies at low and high redshift, many of the precise details leading to differences within these populations remain uncertain.

The present Universe is highly diverse, with galaxies spanning orders of magnitude in size, mass, and environmental densities, and a large range of stellar and gas properties. To resolve the detailed mechanisms responsible for different channels of galaxy evolution therefore requires understanding the link between these key galaxy properties. *In this thesis,*

we focus on the link between galaxy structure and stellar properties in order to understand what drives the evolution of, and differences between, galaxy stellar populations.

1.3. Galaxy Stellar Populations

1.3.1. Star-Formation Histories

The goal of stellar population modelling is to recover a galaxy's star-formation history, answering questions such as: When and at what rate did star formation occur? Where did the stars form (did they form within the galaxy or were they accreted in a merger)? What distribution of stellar masses were produce? And what material did they form from (pristine or metal-enriched gas)? However, modelling of detailed star-formation histories is a complicated and degenerate problem. Even with high-quality spectra, typically only available for the nearest and brightest galaxies, our models are still limited by our understanding of complex aspects of stellar physics, including certain phases of stellar evolution, binarity/multiplicity, and rotation (Charlot et al. 1996; Yi 2003; Lee et al. 2007; Conroy et al. 2009). As a result, non-parametric star-formation history models often lead to degenerate solutions (Leja et al. 2019). An alternative approach that avoids this problem is to assume a parametric form of the star-formation history.

Star-formation histories are often modelled by a star formation rate that decreases exponentially (e.g. Mortlock et al. 2017; McLure et al. 2018; Wu et al. 2018) or log-normally with time (e.g. Gladders et al. 2013; Diemer et al. 2017; Cohn 2018). However, compared to the time-smoothed star-formation histories these parameterisations provide, galaxies can undergo multiple distinct star formation bursts. High-redshift and low-mass galaxies in particular are expected to have bursty star-formation histories (e.g. Guo et al. 2016; Faisst et al. 2019)[4]. Furthermore, 10–15% of quiescent galaxies at $z < 1$ undergo rejuvenated star formation, induced by processes such as mergers (Thomas et al. 2010; Chauke et al. 2019). The multiple distinct stellar populations created by bursty star-formation histories lead to biases in commonly-used single-burst-equivalent stellar population models (Serra & Trager 2007). Therefore, the best parameters (§1.3.2) and analysis method (§1.3.3) to use in representing a galaxy's star-formation history depend not only on the available data quality, but also on the properties of the galaxy itself.

1.3.2. Stellar Population Parameters

The stellar population of a galaxy is a cumulative record of the formation and assembly history of its stars. Research into what drives differences between stellar populations is therefore crucial to understanding galaxy formation and evolution as a whole. Different stellar population parameters each provide a piece of this complex puzzle, with information encoded in various parts of the stellar light. The optical part of the electromagnetic spectrum contains detailed information, but other nearby parts of the spectrum (particularly the

[4] In simulations, smooth star formation is the result of a balance between stellar feedback and gravity, whereas bursty star formation results when this equilibrium state cannot be stably maintained (Faucher-Giguère 2018).

ultraviolet and near-infrared) help constrain properties such as the dust content and total stellar mass (see Conroy 2013 for a review).

Current stellar population analyses rely primarily on the continuum shape (colour) and absorption features in the galaxy's rest-frame optical spectrum. A star's mass and evolutionary stage predominantly determine its intrinsic brightness and temperature (Hertzsprung-Russell diagram; Hertzsprung 1911; Russell 1914). Given stars are approximate black-body radiators (so temperatures correlate with colours), a star's broadband colour and spectral continuum shape therefore also depend primarily on its mass and evolutionary stage, with short-lived, more massive stars being hotter and bluer, and long-lived, less massive stars being cooler and redder. While colours are a useful and robust tool to determine broad stellar characteristics, more detailed information on the star's chemical composition is found in the spectral absorption features. Elements in the atmospheres of stars absorb light at specific wavelengths based on atomic transitions, leading to absorption features in the spectrum, with the depth of the features depending upon both the star's surface temperature (and thus evolutionary stage) and elemental abundance. However a galaxy spectrum is composed of millions to billions of individual stars, with a range of ages and chemical abundances, making it impossible to identify individual stars except for the nearest few galaxies, in which individual stars can be spatially resolved. Therefore, rather than aiming to resolve individual stars making up the galaxy, the aim of stellar population analyses is to characterise the features of the stellar population as a whole from the galaxy's integrated light.

Stellar population analyses of integrated spectra can be expressed in two ways, either weighted by the luminosity of stars or weighted by their mass. Different stellar types have varying intrinsic luminosities, so a galaxy's spectrum is dominated by the intrinsically brightest stars. A small, recent burst of star formation can significantly outshine a much larger, older underlying population, so a galaxy spectrum and its luminosity-weighted parameters are always biased towards the properties of its youngest, most massive stars. Mass-weighted analyses, on the other hand, weight the contribution of the stars by their mass. While mass-weighted measurements are in some ways more physically meaningful, in practice they tend to be less well constrained than luminosity-weighted measurements and, depending upon the method used, may require assuming a star formation history (see §1.3.1). Therefore the best parameterisation (mass- or luminosity-weighted) will depend on the quality of the data and the science goals of the analysis.

A galaxy stellar population consists of a complex distribution in age and chemical abundance, however we have seen that determining this distribution is not feasible. Instead, to build up a picture of a galaxy's star formation history we focus on the first moments. The most relevant parameters for this thesis are mean age, mean combined abundance of metals [Z/H], and mean α-element abundance relative to iron [α/Fe]. We also introduce and briefly describe the star formation rate and the initial mass function.

Mean Age

The mean stellar age depends on when the galaxy first formed stars, when it stopped forming stars, and the rate of star formation at every time in between. As previously discussed

high-mass stars are significantly brighter than their less-massive counterparts, therefore luminosity-weighted age is highly sensitive to the most recent burst of star formation (Serra & Trager 2007) and as a result is always younger than the mass-weighted age. For quiescent galaxies, luminosity-weighted age can be viewed as a proxy for how long ago the galaxy quenched.

Metallicity

The total 'metal' content (Z) is the fraction of the total stellar mass due to elements heavier than helium (He),

$$Z = \sum_{i>H_e} \frac{m_i}{M_*} = 1 - X - Y \tag{1.1}$$

where X, Y, and Z are the mass fractions of hydrogen, helium, and all other elements respectively. Metallicity, [Z/H], is then defined as the logarithm of the ratio of the number density of metals (N_Z) to the number density of hydrogen (N_X) and normalized such that the Sun has zero metallicity:

$$[Z/H] \equiv \log_{10}\left(\frac{N_Z}{N_X}\right) - \log_{10}\left(\frac{N_{Z_\odot}}{N_{X_\odot}}\right) \tag{1.2}$$

The number density of iron (Fe) to hydrogen, [Fe/H], is related to, and often used as proxy for, the total metallicity (Tantalo et al. 1998; Trager et al. 2000b):

$$[Z/H] = [Fe/H] + A[\alpha/Fe] \tag{1.3}$$

where [α/Fe] is the abundance of α-elements relative to iron and the value of the constant A depends on the assumed α-element abundance pattern. However, equation 1.3 represents a simplified model that does not account for abundance variations between different α-elements, and should therefore be used cautiously (Conroy 2013).

During the main sequence period of a star's lifetime it will convert hydrogen to helium, while heavier elements are produced in late, short-lived stages of stellar evolution. Therefore all the heavy elements in a main sequence star were produced by earlier stars and then recycled into the interstellar medium via stellar winds and supernovae[5]. Hence the metallicity of a galaxy tells us about the number of generations of stars the galaxy has formed and the extent to which the current population formed from pristine or recycled gas.

In contrast to stellar age, there is less difference between luminosity-weighted and mass-weighted metallicity, as luminosity-weighted metallicity is less biased by the presence of young, bright stars than mean age (Serra & Trager 2007).

α Element Abundance

The α-enhancement, [α/Fe], is a measure of the relative abundance of α elements (elements such as oxygen, magnesium and calcium that are produced in stars by the alpha process; Burbidge et al. 1957) compared to the iron abundance:

$$[\alpha/Fe] = \log_{10}\left(\frac{N_\alpha}{N_{Fe}}\right)_{star} - \log_{10}\left(\frac{N_\alpha}{N_{Fe}}\right)_{Sun} \tag{1.4}$$

[5] A small but significant amount of helium and lithium were produced in big bang nucleosynthesis (Alpher et al. 1948)

α-enhancement provides a measure of star formation duration by indicating the extent to which the iron produced in Type Ia supernova by relatively long-lived stars is recycled into subsequent stellar generations (e.g. Greggio & Renzini 1983; Matteucci & Greggio 1986; Matteucci 1994; Pagel & Tautvaisiene 1995; Thomas et al. 1998). The massive stars that lead to Type II supernova have lifetimes on the order of 10^{6-7} years, compared to 10^9 years for Type Ia supernova (Tsujimoto et al. 1995). Type II and Type Ia supernovae also have distinct chemical signatures: Type II supernova produce significantly more alpha elements relative to iron compared to Type Ia supernova. Therefore, the abundance of alpha elements with respect to iron is an indication of whether the galaxy was still forming stars when Type Ia supernova enriched the interstellar medium with iron-rich ejecta.

Star Formation Rate

A galaxy's rate of star formation is the amount of stars produced per year ($M_\odot\, yr^{-1}$). In practice, however, what is measured is the average star formation rate of the most massive stars over the last $10^6 - 10^9$ years (depending upon the indicator used), with the formation rate of low-mass stars assumed based on the IMF —see Kennicutt & Evans (2012) for a review. Using multiple indicators therefore provides a more complete picture of a galaxy's star formation history compared to using a single indicator.

For stellar population and galaxy evolution analyses based on optical data, the most commonly used indicators are the H_α and H_β Balmer emission lines, due to their strength and presence in the rest-frame optical wavelength range (Calzetti 2013). The H_α line probes the average star formation over the last 3–10 Myr, a relatively short timescale compared to other common indicators (Hao et al. 2011; Murphy et al. 2011; Kennicutt & Evans 2012). The ratio of H_α to H_β then provides an estimate of the dust extinction (Calzetti 2001), by comparing the measured flux ratio to the theoretical ratio based on atomic physics ($fH_\alpha/fH_\beta = 2.86$ based on Case B recombination; Osterbrock & Ferland 2006). Although Balmer emission can also originate from gas ionised by AGN or shocks in the interstellar medium (Dopita 1976; Shull & McKee 1979), these processes lead to differences in other emission line ratios, most notably the [OIII]/H_β and [NII]/H_α flux ratios. Therefore regions dominated by star formation, AGN, and shocks can be distinguished based on the values of these flux ratios (e.g. the BPT diagram; Baldwin et al. 1981).

Another commonly used indicator of star formation rate is the 4000Å break, which measures the average star formation over Gyr timescales (Poggianti & Barbaro 1997; Kauffmann et al. 2003a; Kriek et al. 2011). It was originally defined as the ratio of the average flux at 4050–4250Å and 3750–3950Å (D4000; Bruzual 1983), but this definition was later updated to use narrower bands at 4000–4100Å and 3850–3950Å (D_n4000; Balogh et al. 1999) that are less sensitive to dust reddening. A strong 4000Å break in quiescent galaxies is caused by both the lack of young, hot stars that radiate at short wavelengths and the accumulation of ionised metals that lead to multiple absorption features in this narrow wavelength range, in particular the Ca II H and K lines. A strong D_n4000 break is highlighted in Figure 1.2 for an example quiescent galaxy from the SDSS Legacy Survey (York et al. 2000; Strauss et al. 2002).

Outside of the optical wavelength range, ultra-violet (UV) and infra-red (IR) photometry

also provide constrains on recent star-formation. UV photometry directly traces the luminosity of young hot stars while IR wavelengths constrain the dust-attenuation, as approximately half of the light produced by stars is absorbed by interstellar dust and remitted at IR wavelengths (Kennicutt & Evans 2012). X-ray and centimeter-radio emission also probe young stellar populations, however the conversion to a star formation rate relies on empirical calibrations, generally to IR luminosities (e.g. Bell 2003; Ranalli et al. 2003).

Initial Mass Function

Stars tend to form in groups from individual massive cold molecular gas clouds. The initial mass function (IMF) describes the distribution of masses at which stars form. While early studies found no strong evidence contradicting a single universal IMF (see Bastian et al. 2010 for a review), more recent evidence suggest the low-mass end (below $1\,M_{\odot}$) varies not only between galaxies (van Dokkum & Conroy 2010; Conroy & van Dokkum 2012b; Cappellari et al. 2012; Spiniello et al. 2014; Li et al. 2017) but within galaxies as well (Martín-Navarro et al. 2015a; van Dokkum et al. 2017; Parikh et al. 2018; Vaughan et al. 2018), although what drives these variations remains unclear. Detecting IMF-sensitive features in optical spectra requires extremely high S/N data, since low-mass stars contribute little to a galaxy's overall luminosity (~1% for stars below $0.4\,M_{\odot}$ for a Milky Way IMF; Conroy & van Dokkum 2012a). Therefore, unless the analysis is specifically focusing on IMF variations, stellar population studies will generally assume an IMF. Because plausible variations in the low-mass end of the IMF lead to only small changes in the observed spectrum of a galaxy, IMF selection has little effect on measured luminosity-weighted stellar population parameters. The selection does however have a greater influence on mass-weighted measurements. Throughout the work presented in this thesis, we assume a Chabrier (2003) IMF.

1.3.3. Stellar Population Analyses

The leading approach to stellar population analyses has evolved significantly over the past half century. Broadband colours formed the basis of many early works until advances in instrumentation and our understanding of stellar evolution allowed for studies based on specific absorption lines. More recently, as theoretical stellar models have progressed and data quality improves, studies are now able to take advantage of the wealth of information available in the full optical spectrum via a full spectral fitting approach.

Broadband Colours

Photometric colours provide a robust, directly observable parameter for analysing stellar populations and so formed the basis of early stellar population studies (see Tinsley 1980 for a review). They remain a valuable way to study galaxies at high redshift where high-quality spectra are difficult to obtain (e.g. Mei et al. 2006; De Lucia et al. 2007; Rogers et al. 2014). These early works established key scaling relations, in particular the colour–absolute magnitude diagram (Baum 1959; Sandage 1972; Visvanathan & Sandage 1977), in which old, metal-rich, quiescent galaxies lie in a 'red sequence' and young, star-forming galaxies lie in a separate 'blue cloud', with few galaxies in the transitional 'green valley' region (see

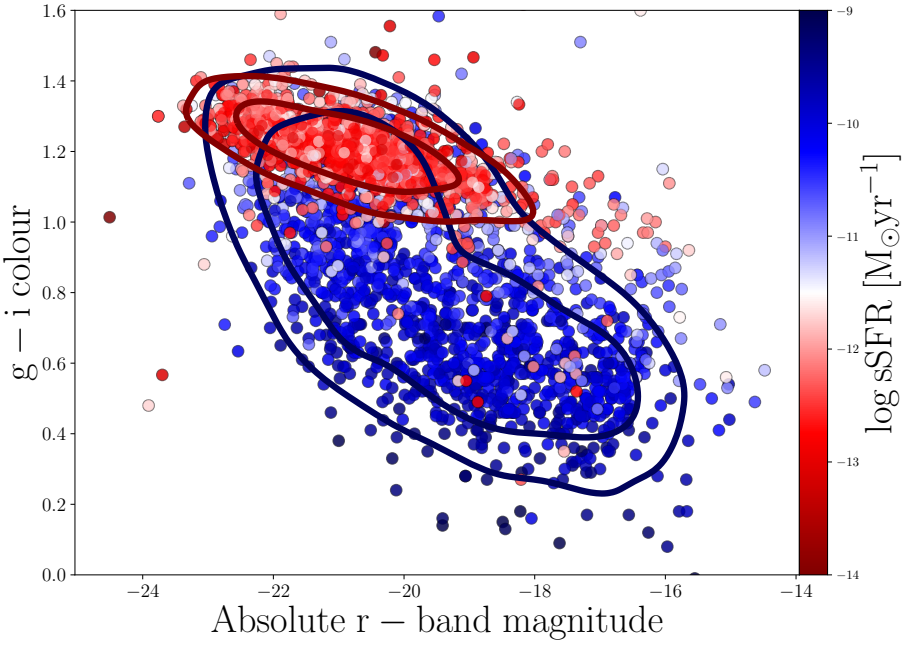

Figure 1.1 A colour–magnitude diagram using g–i colour and absolute r-band magnitude for $z \sim 0$ galaxies from the SAMI Galaxy Survey (Croom et al. 2021b). The colourscale shows specific star formation rate (sSFR), with star formation rates from Medling et al. (2018). The quiescent early-types form a tight 'red sequence', while the star-forming late-types form a 'blue cloud' (Baum 1959; Sandage 1972; Visvanathan & Sandage 1977). Here the two populations are defined by a cut at 1.0 dex below the star-forming main sequence as defined by Whitaker et al. (2012) and the contours enclose 60% and 90% of each population.

Fig. 1.1). Advances in stellar mass modelling and estimates have seen absolute magnitude replaced on the horizontal axis by stellar mass (the two are closely related; see Taylor et al. 2011).

A severe limitation of stellar population studies relying on photometric colours is that key parameters are degenerate in optical photometry. While different optical photometric bands have varying sensitivities to age and metallicity, they are all affected to some extent by both parameters (Li & Han 2007), leading to a degeneracy between age and metallicity measurements. Worthey (1992, 1994) found that a factor 2 increase in metallicity produces the same colour change as a factor 3 increase in age in $U - V$ colour. IMF variations and dust extinction can also affect integrated colour.

Absorption Line Indices

Spectroscopic observations allow the identification and measurement of specific spectral absorption features with varying dependencies on stellar population parameters. They thus resolve the problem of degeneracy between broadband colours and provide well-constrained age and metallicity measurements that established a benchmark for the analysis of early-type galaxy and globular cluster stellar populations (Faber 1973). Popular sets of absorption features include the Lick index system (based on observations from the Lick Observatory; Faber et al. 1985; Worthey et al. 1994; Worthey & Ottaviani 1997; Trager et al. 1998), Rose indices (Rose 1985, 1994), and the Line Index System (LIS; Vazdekis et al. 2010). These can be used directly in analyses or as input to stellar population models (e.g. Schiavon

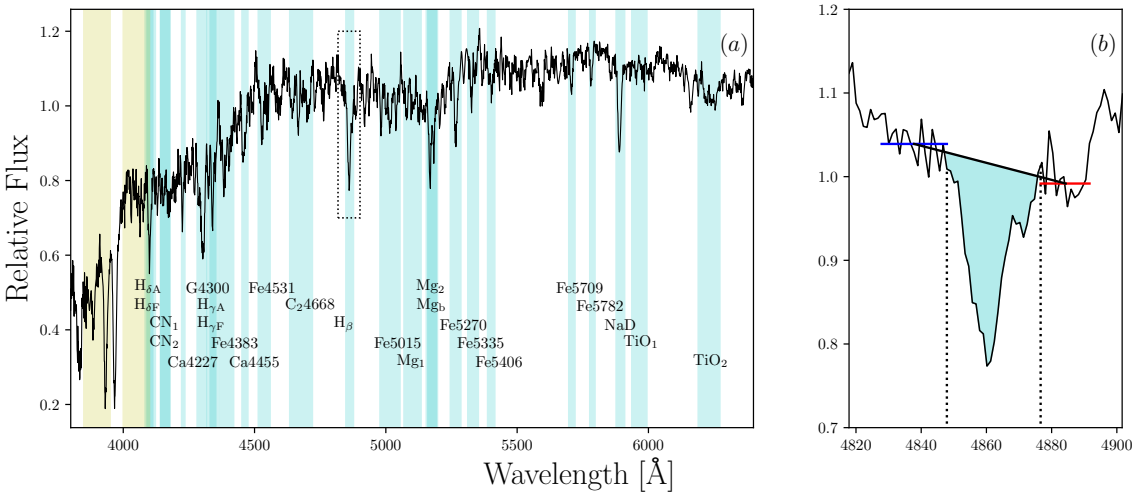

Figure 1.2 Rest-frame optical spectrum for quiescent galaxy spec-0592-52025-0308 from the SDSS Legacy Survey (York et al. 2000; Strauss et al. 2002). Panel (a) shows the entire wavelength range and panel (b) shows a close-up of the H_β index (indicated by a black dotted box in panel (a)). The cyan regions in panel (a) indicate the wavelength ranges covered by the 25 labelled Lick indices. The yellow regions indicate the D_n4000 bands (see § 1.3.2 Star Formation Rate). The red and blue horizontal lines in panel (b) indicate the measured red and blue continuum levels respectively, and the black pseudo-continuum line joins the continuum-band midpoints. The dotted vertical lines indicate the defined width of the index. The cyan shaded region corresponds to the value of the H_β index, defined as the integrated flux difference between the pseudo-continuum and the observed spectrum.

2007; Thomas et al. 2011). Index-based stellar population parameters are usually presented as luminosity-weighted, as this is what is directly observed. While it is possible to obtain mass-weighted values (e.g. Ganda et al. 2007), this requires the assumption of a specific model for the star formation history (§1.3.1).

The widely-used Lick index system is a set of 25 absorption features sensitive to a range of atomic and molecular energy transitions, selected to lie within the wavelength range of the Lick spectrograph. Faber et al. (1985) originally defined a set of 11 indices, which was extended to 21 by Worthey et al. (1994). Worthey & Ottaviani (1997) then included 4 higher-order Balmer series lines that are sensitive to mean age. The full set of indices comprises:

- Balmer series: H_β, $H_{\delta A}$, $H_{\delta F}$, $H_{\gamma A}$, $H_{\gamma F}$
- Iron-peak elements: Fe4383, Fe4531, Fe5270, Fe5335, Fe5406, Fe5709, Fe5782
- Molecular bands: CN_1, CN_2, C_24668 [6], Mg_1, Mg_2, TiO_1, TiO_2
- Various atomic absorption lines: Ca4227, G4300, Ca4455, C_24668, Mg*b*, Na D

Indices are measured by summing the total flux within a well-defined index band, relative to bands on either side defining the blue and red continuum levels. Panel (b) of Figure 1.2 shows how indices are measured using the H_β line as an example. The red and blue horizontal lines indicate the measured red and blue continuum levels respectively, and a

[6] The C_24668 index was originally labelled as Fe4668 by Worthey et al. (1994), however the convention changed after it was shown to depend strongly on the carbon abundance (Tripicco & Bell 1995; Jorgensen 1997).

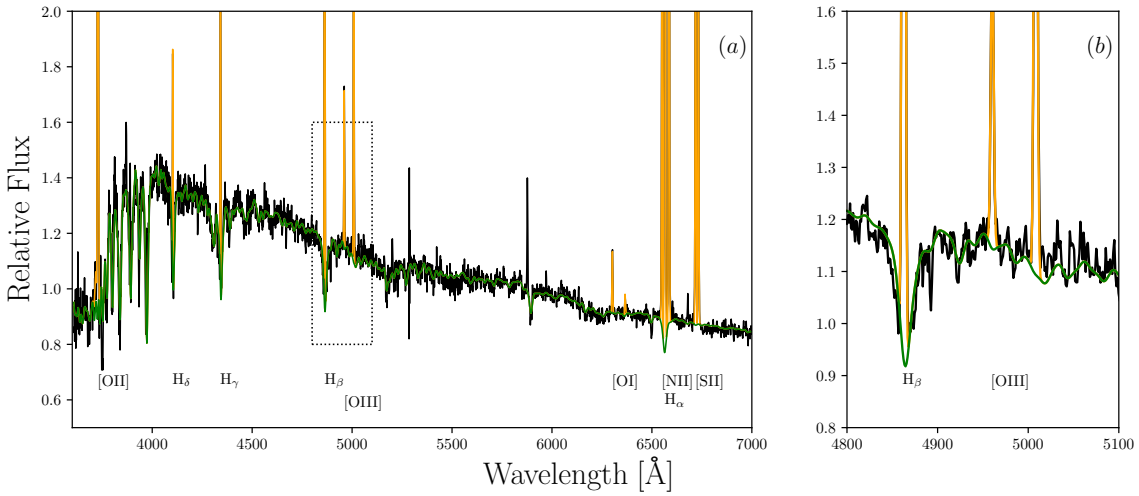

Figure 1.3 Rest-frame optical spectrum for star-forming galaxy spec-0624-52377-0031 from the SDSS Legacy Survey (York et al. 2000; Strauss et al. 2002). Panel (a) shows the entire wavelength range, and panel (b) shows a close-up of the H_β and [OIII] features highlighted by the black dotted box in panel (a). The black line is the observed spectrum, the green line is the fit to the stellar features, and the orange lines are the fits to the labelled gas emission lines. As illustrated by panel (b), a full spectral fitting approach is able to measure the depth of stellar absorption features despite them being obscured by ionised gas emission.

straight line between the continuum-band midpoints at these levels defines the 'pseudo-continuum'. The depth of the index is then the integrated flux difference between the pseudo-continuum and the observed spectrum.

The low level of ongoing star formation in early-type galaxies and globular clusters means the spectral absorption lines are relatively free of emission from ionised interstellar gas, allowing for precise measurements. Conversely, emission from ionised gas in star-forming galaxies contaminates absorption features, making it difficult to take reliable measurements. Additionally, while the single-burst parameterisation commonly used in index-based analyses is an acceptable simplification for old quiescent populations, it is inadequate for representing the continuing star formation in late-type galaxies. As a result, the stellar populations of star-forming galaxies are much less studied than those of quiescent galaxies.

Full Spectral Fitting

Recent advances in stellar evolution modelling have produced sets of theoretical spectra for single-age, single-metallicity populations, allowing a full spectral fitting approach that uses not just a limited number of absorption features but the whole spectrum, including the shape of the continuum. Widely-used models include Bruzual & Charlot (2003), Binary Population and Spectral Synthesis (BPASS; Eldridge et al. 2017; Stanway & Eldridge 2018), and those based on the Medium resolution INT Library of Empirical Spectra (MILES; Sánchez-Blázquez et al. 2006b; Vazdekis et al. 2010, 2015).

A key feature of a full spectral fitting approach is that it allows for simultaneous fitting of both the stellar spectrum and the ionised gas emission. As demonstrated in Figure 1.3, by accounting for both the gas and stellar features, a full spectral fit is able to measure the depth of absorption features despite them being obscured by gas emission lines. Depending upon the sample properties and data quality, a common alternative to explicitly fitting the

emission lines is to instead mask these regions, and use the fit to the rest of the spectrum to recover the masked absorption features. By fitting or masking emission lines, a full spectral fitting approach is better able to constrain stellar population parameters for star-forming galaxies compared to an index-based analysis.

Another useful attribute of a full spectral fitting approach is the ability to measure mass-weighted stellar population properties without assuming a parameterised star formation history. To perform a mass-weighted analysis, the templates used in the fit are scaled by their relative brightness. This effectively up-weights the brightest templates, so fewer are needed in the fit to recreate the spectrum. While mass-weighted measurements are more physically meaningful, in practice they tend to be less well constrained than luminosity-weighted measurements. For star-forming galaxies particularly, the spectra are so sensitive to young stars that the contribution from low-luminosity old stars is poorly constrained, making it difficult to recover the true mass-weighted parameters. Additionally, most stellar population results based on index measurements are luminosity-weighted, so luminosity-weighted parameters from a full spectral fit are more directly comparable to results from studies based on indices.

1.3.4. Scaling Relations

Stellar population parameters have been found to correlate with a wide range of galaxy properties. Many studies have focused on the dependence of stellar population on mass (Gallazzi et al. 2005; Nelan et al. 2005; Lian et al. 2018) and velocity dispersion σ (early-types: Graves et al. 2009a,b; Robaina et al. 2012; late-types: Ganda et al. 2007; early spirals: Peletier et al. 2007). Other works have investigated correlations with the IMF (La Barbera et al. 2013), morphological type (Ganda et al. 2007; González Delgado et al. 2015; Scott et al. 2017), central black hole mass (Martín-Navarro et al. 2016), and structural lopsidedness (Reichard et al. 2009).

However it is often unclear which (if any) of these correlations imply causation and which are the result of other underlying trends—for example, until recently it was uncertain whether the population–environment relations are causal (Thomas et al. 2005; Sánchez-Blázquez et al. 2006a; Schawinski et al. 2007b) or the result of both stellar population and environment correlating with stellar mass M_* (Thomas et al. 2010; McDermid et al. 2015). Recent studies by Liu et al. (2016) and Scott et al. (2017) have reconciled this disparity, showing that dependence on mass alone is insufficient to explain observed trends and environment plays a measurable, albeit secondary, role. Furthermore, it is unclear whether the well studied colour–magnitude relation is a consequence of both parameters correlating with σ (Bernardi et al. 2005) or M_* (Gallazzi et al. 2006). The difficulty is that these trends are often not directly comparable, due to different uncertainties in the observations and models, and different selection effects and biases—one correlation appearing stronger than another may simply reflect a higher precision in the measurements rather than underlying physics.

By quantitatively comparing scaling relations, several recent studies have demonstrated a clear effect of galaxy size R_e on stellar population for galaxies ranging from highly star-forming to quiescent. Franx et al. (2008) found that out to $z \sim 3$, M_* alone is not a good

predictor of star formation history and that colour as a function of stellar mass surface density $\Sigma \propto M_*/R_e^2$ or gravitational potential $\Phi \propto M_*/R_e$ (sometimes referred to as 'inferred velocity dispersion') shows less scatter than as a function of M_*. This was extended to low redshifts ($z < 0.11$) by Wake et al. (2012), who, by quantifying residual trends when one parameter is held fixed, asserted that $u - r$ colour correlates more strongly with σ than Σ, Sérsic index (Sersic 1968), or M_*. Using spectroscopically-derived stellar population parameters for low redshift samples, Scott et al. (2017) and Li et al. (2018) showed that for both early- and late-type galaxies much of the scatter in population–mass relations is due to variations with galaxy size by demonstrating how stellar population varies in the mass–size plane (see also McDermid et al. 2015 for early-types). Additionally, van de Sande et al. (2018) showed stellar age is tightly coupled with intrinsic ellipticity for both early- and late-type galaxies. However, without a comparative analysis of these trends, and without taking into account different measurement uncertainties, we cannot infer which empirical correlation is the tightest, and therefore cannot infer causation.

1.4. Thesis Focus

In this thesis we quantitatively compare global stellar population trends with galaxy structure and dynamics. We want to understand which relations have the lowest *intrinsic* scatter, in order to distinguish between fundamental correlations and correlations that result from some other underlying trend. We do this by analysing both the intrinsic scatter of the correlations and residual trends, focusing on the correlations between stellar population and galaxy structural parameters, specifically mass M, gravitational potential $\Phi \propto M/R$, and surface density $\Sigma \propto M/R^2$.

A key aspect of the methodology used in this thesis is the treatment and measurement of the intrinsic scatter in the correlations. The absolute intrinsic scatter is difficult to measure because it depends strongly on the assumed measurement uncertainties. Instead, we can use the necessary condition that, due to the non-zero uncertainty on radius R, M/R^x must have a higher observational uncertainty than M alone (for $x \neq 0$). Using this principle and comparing the observed scatter about the fits, we can rank the correlations between stellar population and galaxy structural parameters (mass M, gravitational potential $\Phi \propto M/R$, and surface density $\Sigma \propto M/R^2$) based on their relative intrinsic scatter. Because these three structural parameters differ only by factors of the effective radius, we can directly compare the observational uncertainties and hence infer the relative intrinsic scatter for each of these relations. We can also look at the residuals of each trend with galaxy size. This robust analysis allows us to determine which of these physical factors primarily determines various galaxy stellar population parameters and so obtain clues to the mechanisms that drive their evolution.

In Chapter 2 (published in Barone et al. 2018) we investigate low-redshift morphologically-identified early-type galaxies from the Sydney-AAO Multi-object Integral-field (SAMI) galaxy survey (Croom et al. 2012; Bryant et al. 2015). We investigate correlations between stellar population and the aforementioned structural parameters using both the stellar mass as well as a proxy for the dynamical mass M_D based on the virial theorem $M_D \equiv \sigma^2 R_e$. In Chapter 3 (published in Barone et al. 2020) we build on the results presented in Chapter 2

by studying the ages and metallicities of low-redshift star-forming galaxies selected from the legacy Sloan Digital Sky Survey (SDSS; York et al. 2000; Strauss et al. 2002). We then extend our analysis beyond the low-redshift Universe in Chapter 4 (published in Barone et al. 2022), where we analyse intermediate-redshift galaxies from the Large Early Galaxy Astrophysics Census (LEGA-C) survey (van der Wel et al. 2016). Finally, in Chapter 5 we summarise all our results and discuss future work.

CHAPTER 2

Low-Redshift Early-Type Galaxies

The work presented in this chapter has been previously published as 'The SAMI Galaxy Survey: Gravitational Potential and Surface Density Drive Stellar Populations. I. Early-type Galaxies ', Barone, Tania M.; D'Eugenio, Francesco; Colless, Matthew; Scott, Nicholas; et al., 2018, ApJ, 856, 64B.

2.1. Introduction

In this Chapter we investigate the stellar population properties of morphologically-identified early-type galaxies from the SAMI Galaxy survey (Croom et al. 2012; Bryant et al. 2015). As discussed in Section 1.4 we are interested in the correlations between global stellar population, and the galaxy parameters mass M, gravitational potential $\Phi \propto M/R$, and surface density $\Sigma \propto M/R^2$. For each structural parameter, we define two estimators, one based on spectroscopic velocity dispersion (henceforth, called the spectroscopic estimators), the other based on photometric stellar masses (the photometric estimators). Within each set of estimators (i.e., the spectroscopic or photometric), the three structural parameters differ only by factors of the effective radius, allowing us to directly compare the observational uncertainty and hence infer the relative intrinsic scatter in the relations. This Chapter is arranged as follows. In Section 2.2 we present the SAMI Galaxy survey and our sample

selection. We also describe the spectroscopic and photometric masses and subsequent structural measurements. Section 2.3 describes our analysis and results. We discuss and summarise our results in Sections 2.4 and 2.5 respectively.

2.2. The SAMI Galaxy Survey

The SAMI Galaxy Survey is an integral-field survey of 3068 unique galaxies (Scott et al. 2018; Croom et al. 2021b). The survey uses the SAMI instrument installed on the 3.9m Anglo-Australian Telescope, connected to the AAOmega spectrograph (Sharp et al. 2006; see Sharp et al. 2015 for data reduction). The sample is mass selected, however the mass limit varies depending upon the redshift range. Details of the target selection and input catalogs are described in Bryant et al. (2015), with the cluster galaxies further described in Owers et al. (2017). The SAMI spectrograph uses 13 fused-fibre hexabundles (Bland-Hawthorn et al. 2011; Bryant et al. 2014), each composed of 61 individual fibres, tightly packed to form an approximately circular grid 15 arcsec in diameter. In this Chapter we use data from internal release v0.9.1, comprising 1380 galaxies with low redshifts ($z < 0.1$) and a broad range of stellar masses $10^7 < M_* < 10^{12}$ (Allen et al. 2015; Green et al. 2018). We define a subsample of 625 ETGs having a visual morphological classification of elliptical, lenticular, or early spiral (Cortese et al. 2016). Excluding early spirals from our sample does not change our conclusions.

We experimented with different samples, including a mass-function weighted sample using weights based on the stellar mass function of Kelvin et al. (2014), which gives the effective number of galaxies per unit volume in a stellar mass interval. The weights were calculated by taking the ratio between the stellar mass function, and the actual number of observed SAMI galaxies in each stellar mass interval. The results of this analysis are summarized in Table 2.1, alongside the results of the analysis without weights. We find consistent results between the original SAMI sample (which is mass-limited in redshift bins) and the mass-function weighted sample (which approximates a sample with a single mass limit). Since the two analyses are consistent, to avoid over-dependence on this theoretical model, we focus our analysis on the results without weights.

We use $g - i$ colour as a simple, directly observable parameter for comparing SPs; we use the dust-uncorrected values to remain model-independent. For the ETG subsample, we use the single-burst equivalent, luminosity-weighted SP parameters age, metallicity [Z/H], and α-element abundance [α/Fe] from Scott et al. (2017). Stellar masses, M_*, were obtained from $g - i$ colour by Bryant et al. (2015) and Owers et al. (2017) following the method of Taylor et al. (2011):

$$\log_{10} \frac{M_*}{M_\odot} = 1.15 + 0.70(g - i)_{rest} - 0.4M_i \tag{2.1}$$

Where M_i is the rest frame i-band absolute AB magnitude, and M_* has solar mass units.

Effective radii (R_e) were measured using Multi-Gaussian Expansion modeling (Cappellari 2002) from r-band images; R_e is the projected, circularised radius enclosing half the total light. The luminosity-weighted, line-of-sight velocity dispersion (σ) within $1R_e$ was then measured as in van de Sande et al. (2017).

		Unweighted				Mass-function Weighted			
Y-axis	X-axis	RMS_G	ρ_S	$\frac{a_r}{\Delta a_r}$	RMS_{rm}	RMS_G	ρ_S	$\frac{a_r}{\Delta a_r}$	RMS_{rm}
$g-i_{all}$	M_*	0.1589 ± 0.0004	0.78	19.7	0.1586	0.1589 ± 0.0004	0.78	19.8	0.1586
$g-i_{all}$	M_*/R_e	0.1269 ± 0.0005	0.87	9.0	0.1277	0.1269 ± 0.0005	0.87	7.1	0.1277
$g-i_{all}$	M_*/R_e^2	0.1438 ± 0.0008	0.82	-13.9	0.1370	0.1438 ± 0.0008	0.82	-16.4	0.1370
$g-i_{ETG}$	M_*	0.0910 ± 0.0004	0.50	7.3	0.0896	0.0962 ± 0.0004	0.50	10.0	0.0954
$g-i_{ETG}$	M_*/R_e	0.0816 ± 0.0012	0.67	2.7	0.0786	0.0839 ± 0.0014	0.67	5.2	0.0797
$g-i_{ETG}$	M_*/R_e^2	0.0929 ± 0.0014	0.44	-11.5	0.0891	0.0961 ± 0.0015	0.45	-9.6	0.0918
[Z/H]	M_D	0.1678 ± 0.0003	0.38	4.7	0.1664	0.1866 ± 0.0004	0.37	5.0	0.1855
[Z/H]	M_D/R_e	0.1534 ± 0.0002	0.47	3.6	0.1531	0.1708 ± 0.0006	0.50	2.6	0.1719
[Z/H]	M_D/R_e^2	0.1750 ± 0.0002	0.44	-6.2	0.1738	0.1834 ± 0.0005	0.43	-5.3	0.1829
[Z/H]	M_*	0.1647 ± 0.0003	0.40	7.5	0.1647	0.1773 ± 0.0003	0.41	6.7	0.1776
[Z/H]	M_*/R_e	0.1549 ± 0.0015	0.50	3.0	0.1515	0.1652 ± 0.0013	0.53	1.0	0.1648
[Z/H]	M_*/R_e^2	0.1766 ± 0.0012	0.41	-11.2	0.1736	0.1876 ± 0.0009	0.39	-10.0	0.1855
Age	M_D	0.2283 ± 0.0024	0.15	10.3	0.2275	0.2281 ± 0.0024	0.17	8.7	0.2264
Age	M_D/R_e	0.2183 ± 0.0045	0.42	10.0	0.2095	0.2137 ± 0.0046	0.47	9.0	0.2053
Age	M_D/R_e^2	0.1993 ± 0.0041	0.57	-0.6	0.1911	0.1954 ± 0.0044	0.60	-0.5	0.1867
Age	M_*	0.2330 ± 0.0045	0.10	14.9	0.2253	0.2370 ± 0.0045	0.14	8.3	0.2312
Age	M_*/R_e	0.2484 ± 0.0113	0.39	7.4	0.2045	0.2391 ± 0.0106	0.45	5.8	0.2019
Age	M_*/R_e^2	0.2389 ± 0.0098	0.47	-7.1	0.2047	0.2348 ± 0.0102	0.47	-6.0	0.2029
[α/Fe]	M_D	0.1049 ± 0.0007	0.32	7.8	0.1046	0.1072 ± 0.0006	0.27	4.9	0.1075
[α/Fe]	M_D/R_e	0.0961 ± 0.0007	0.49	3.6	0.0946	0.0999 ± 0.0009	0.43	4.0	0.0982
[α/Fe]	M_D/R_e^2	0.0963 ± 0.0007	0.51	-5.4	0.0954	0.1009 ± 0.0010	0.45	-3.6	0.0983
[α/Fe]	M_*	0.1094 ± 0.0007	0.21	2.1	0.1084	0.1110 ± 0.0007	0.20	2.9	0.1103
[α/Fe]	M_*/R_e	0.1032 ± 0.0015	0.39	1.0	0.1019	0.1073 ± 0.0018	0.34	0.8	0.1056
[α/Fe]	M_*/R_e^2	0.1076 ± 0.0014	0.30	-6.7	0.1066	0.1099 ± 0.0013	0.23	-5.2	0.1087

Table 2.1 Summary of the results for both the unweighted, and the mass-function weighted analyses. RMS_G and RMS_{rm} indicate the RMS values about the Gaussian model fit, and the running median respectively. ρ_S represents the Spearman correlation coefficient. $\frac{a_r}{\Delta a_r}$ shows the σ significance of the residual trend with size, where a_r is the slope of the residual trend with 1σ uncertainty Δa_r

We define spectroscopic estimators for the gravitational potential $\Phi \propto \sigma^2$ and surface density $\Sigma \propto \sigma^2/R_e$ by assuming galaxies are structurally homologous and in virial equilibrium. We use the virial theorem to also define the spectroscopic (dynamical) mass proxy $M_D \equiv \sigma^2 R_e/(3G)$ (the arbitrary 1/3 scaling factor conveniently makes M_D span the same range as M_*). Further assuming a uniform dark matter fraction within $1R_e$, we define the photometric estimators $\Phi \propto M_*/R_e$ and $\Sigma \propto M_*/R_e^2$. Hence we have two independent methods for estimating mass, gravitational potential, and surface density: M_*, M_*/R_e and M_*/R_e^2 rely solely on photometry, whereas M_D, M_D/R_e and M_D/R_e^2 also use spectroscopy. In the limit that galaxies are virialized and have the same mass-to-light ratio, these measures would be proportional. We note that M_* is calculated under the assumption of a uniform Chabrier (2003) initial mass function (IMF). However, the IMF may vary systematically with stellar mass-to-light ratio, leading to an underestimated M_* for massive galaxies (Cappellari et al. 2012). Despite this bias, the photometric results are remarkably consistent with the spectroscopic results, and are included to provide an independent measure for each structural parameter with uncorrelated uncertainties. In addition, photometric observations are significantly less expensive than spectroscopy.

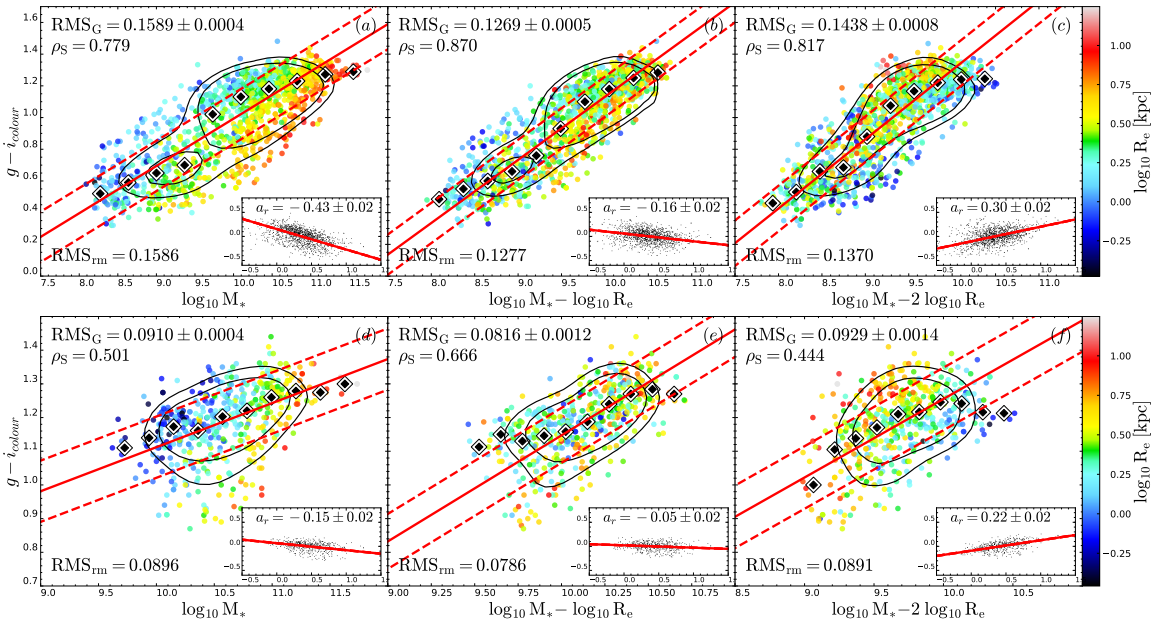

Figure 2.1 $g - i$ colour versus M_*, M_*/R_e, and M_*/R_e^2 for the full sample (top row) and for the ETG subsample (bottom row). The solid red line is the best-fit linear relation and the dashed red lines indicate the RMS about this fit. The RMS of the best-fit line (RMS$_G$) with its 1σ uncertainty is given at the top of each panel, along with the Spearman coefficient ρ_S. The black diamonds show the running median in evenly spaced bins, and the RMS about this running median (RMS$_{rm}$) is shown in the bottom left of the panels. The contours enclose 60% and 80% of the data. The colour scale indicates R_e in units of log(kpc). The inset panels show the best-fit residuals (data - best-fit) as a function of log R_e. The slope of the residual trend a_r is displayed at the top of each inset. For both the full SAMI sample and the ETG subsample, the colour–M_*/R_e relations (panels b and e) have less scatter (lower RMS$_G$ and RMS$_{rm}$), are more significant (higher ρ_S), and have less residual trend with radius (demonstrated by the inset panels) compared to the relations with M_* or M_*/R_e^2.

2.3. Methods and Results

We fit linear relations via a maximum likelihood optimization followed by Markov Chain Monte Carlo (MCMC) integration (Goodman & Weare 2010). The data is modeled as a two-dimensional Gaussian, which avoids bias inherent to orthogonal or parallel least squares regressions (see e.g. Magoulas et al. 2012). The log-likelihood function is optimized using the method of Differential Evolution (Storn & Price 1997; Price et al. 2005). For all the relations except for age, we perform outlier rejection by omitting points which lie outside the 90% contour line. Due to the larger scatter, in the age relations we perform the outlier rejection at the 80% contour. We calculate the root-mean-square about the Gaussian model fit (RMS$_G$), which is displayed at the top left on each panel.

In order to assess whether the linear fit is an accurate model, we compute a running median using equally sized bins in log-space. For all the correlations that we consider to be physically motivated, the running median closely follows the log-linear fits, supporting our choice of model. The RMS about the running median (RMS$_{rm}$) is shown at the bottom left in the panels.

For each relation, we also fit the residuals about the Gaussian model as a function of R_e, using the same method as for the main relation. These residual fits indicate which of M, Φ, or Σ best encapsulates the SP parameter's dependence on galaxy size. The errors from the initial fit are incorporated into the uncertainty on the residual values, which in turn is taken

into account when fitting the residuals.

We use RMS_G and $\mathrm{RMS}_{\mathrm{rm}}$ to determine the quality of the relation, and the Spearman coefficient (ρ_S) to define the significance of the trend. We estimate the uncertainties on each parameter by full integration of the posterior distribution. Our results remain unchanged whether we use the median-absolute-deviation (MAD) or RMS.

Due to the relatively small sample size, plane fits of SP parameters as log-linear combinations of M_D (or M_*) and R_e were poorly constrained, and hence omitted.

We firstly compare how $g-i$ colour trends with the photometric estimators M_*, M_*/R_e and M_*/R_e^2 using both the full sample and the ETG subsample. Although M_* has an explicit dependence on $g-i$ colour, we also use M_* to estimate all three proxies, so any bias due to this explicit dependence will not affect the comparison. For an analysis using spectral energy distribution masses, see Chapter 3. We can rule out a correlation in the uncertainties due to random errors on M_* and R_e, because R_e uses r-band photometry whereas M_* uses g- and i-band magnitudes. We then use the ETG subsample to fit [Z/H], age, and $[\alpha/\mathrm{Fe}]$ as functions of M, Φ, and Σ using both the spectroscopic and photometric measures.

We perform an identical analysis on the mass-function weighted sample, and summarize the results in Table 2.1. Given the analyses show consistent results, in this section we focus on the unweighted analysis.

2.3.1. $g-i$ Colour

Figure 2.1a shows $g-i$ colour as a function of M_* for the full sample, and exhibits the well-documented bimodal trend of colour–mass diagrams, with galaxies forming a red sequence (RS) and blue cloud (BC). As the contour lines reveal, the RS and BC do not align in colour–M_* space, and so the best-fit line does not accurately model the distinct distributions; it simply provides a reference for comparison of the RS and BC alignment for the different relations. The colour scale indicates galaxy size and shows a strong residual trend, implying that, at fixed mass, size contains additional information on $g-i$ colour. By comparison, Figure 2.1b shows that in the colour–M_*/R_e diagram the residual trend with size is significantly less; furthermore, the RS and BC are better aligned in Figure 2.1b, as apparent from the contours and demonstrated by the lower $\mathrm{RMS}_\mathrm{G} = 0.127$ (cf. $\mathrm{RMS}_\mathrm{G} = 0.159$ for colour–M_*). Similarly, comparing colour as a function of M_*/R_e (Figure 2.1b) and of M_*/R_e^2 (Figure 2.1c), the RMS values are smaller and the residual trend with size is less significant for colour–M_*/R_e.

The bottom row of Figure 2.1 shows these relations for the ETG subsample (effectively for the RS only). For ETGs, $g-i$ colour has a stronger and tighter relation with M_*/R_e compared to either M_* or M_*/R_e^2, and less residual trend with size. By construction, M_*/R_e necessarily has a larger observational uncertainty than M_* alone, as M_*/R_e includes the uncertainty on both M_* and R_e. Yet the colour–M_*/R_e relation shows less scatter than colour–M_*, therefore colour–M_*/R_e must have significantly lower *intrinsic* scatter. Furthermore, colour–M_*/R_e has a higher Spearman coefficient of $\rho_S = 0.666$, compared to $\rho_S = 0.501$ and 0.444 for M_* and M_*/R_e^2 respectively. For both the total sample and the ETG subsample, compared to trends with M_* and M_*/R_e^2, the colour–M_*/R_e relation has the lowest RMS values, least residual trend with size, and highest ρ_S.

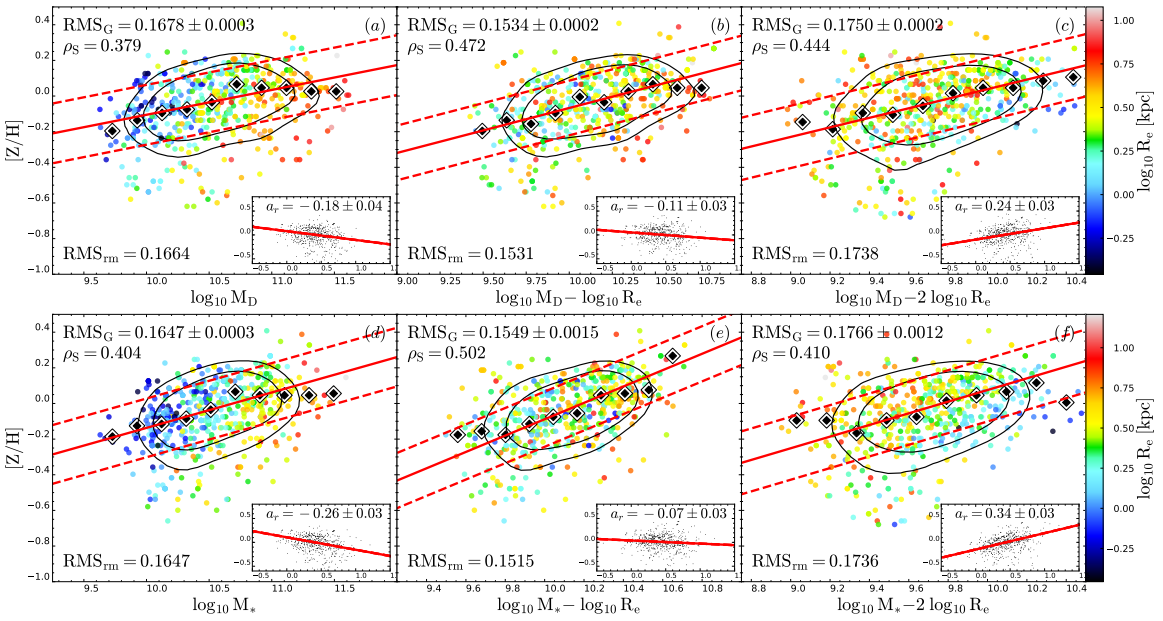

Figure 2.2 [Z/H] versus M, Φ, and Σ for ETGs. The top row uses the spectroscopic estimator $M_D \propto \sigma^2 R_e$, the bottom row uses the purely photometric M_*. The inset panels show the best-fit residuals (data - best-fit) as a function of $\log R_e$ (other details as for Figure 1). For both the spectroscopic and photometric estimators, the [Z/H]–Φ relations (panels b and e) have the least scatter (lowest RMS$_G$ and RMS$_{rm}$), are the most significant (highest ρ_S), and have the least residual trend with radius (inset panel).

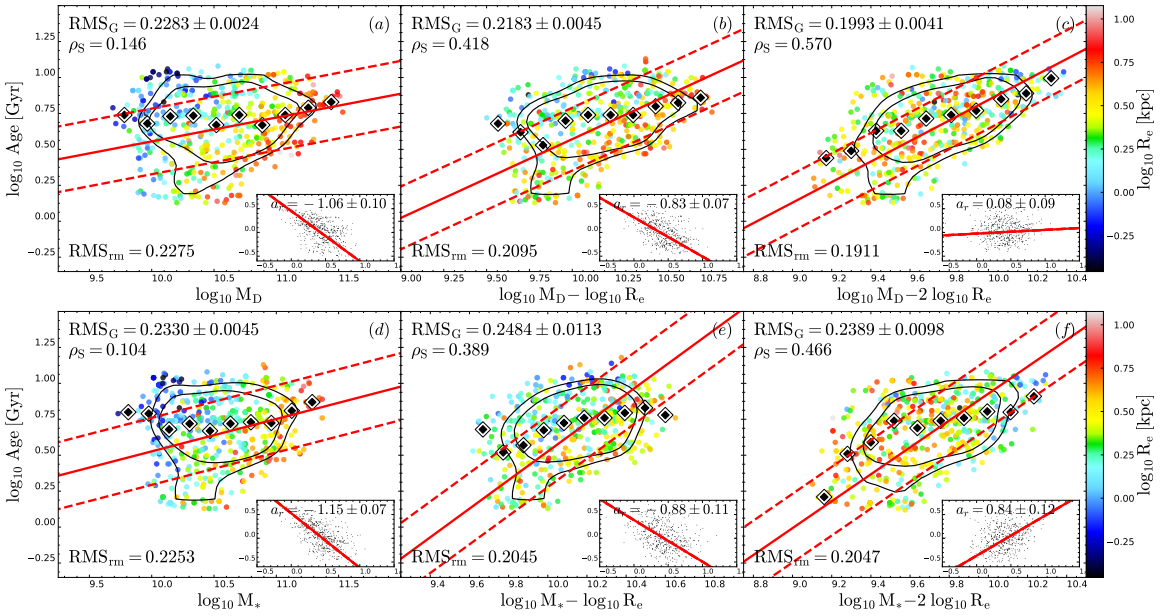

Figure 2.3 Age versus M, Φ, and Σ for ETGs. The top row uses the spectroscopic estimator $M_D \propto \sigma^2 R_e$, the bottom row uses the purely photometric M_*. The inset panels show the best-fit residuals (data - best-fit) as a function of $\log R_e$ (other details as for Figure 1). Overall, for both the spectroscopic and photometric estimators, the age–Σ relations (panels c and f) tend to have the least scatter (lowest RMS$_G$ and RMS$_{rm}$), are the most significant (highest ρ_S), and have the least residual trend with radius (inset panel).

2.3.2. Metallicity

In Figure 2.2 we show the relations between [Z/H] and M, Φ, and Σ; the top row uses spectroscopic virial masses and the bottom row photometric stellar masses. We see consistent results between the spectroscopic and photometric mass estimators. With increasing power of R_e, the residual trend with size goes from negative in the [Z/H]–M relations, to close to zero for [Z/H]–Φ, and finally to positive for [Z/H]–Σ. The [Z/H]–Φ relations also have the tightest and most significant correlations; [Z/H]–M_*/R_e has an $RMS_G = 0.155$, whereas the RMS_G values for [Z/H]–M_* and [Z/H]–M_*/R_e^2 are higher by 7σ and 14σ respectively. Given the higher observational uncertainty on M_*/R_e than M_* alone, the lower RMS for [Z/H]–M/R_e implies this relation must also have a lower intrinsic scatter than [Z/H]–M. For the spectroscopic estimators, $M_D/R_e \propto \sigma^2$ and hence has a lower observational uncertainty than M_D and M_D/R_e^2, and so we cannot comment on the relative intrinsic scatter about these trends. The result is, however, consistent with the photometric estimators, with [Z/H]–M_D/R_e showing the lowest RMS. The two [Z/H]–Φ relations also show the highest ρ_S.

2.3.3. Age

We show the results of our analysis for age in Figure 2.3. There is more scatter in the age relations than in the other SP parameters, most likely because age is more sensitive to recent bursts of star formation (Serra & Trager 2007). Despite this larger scatter, we see statistically significant results.

Age is well-known to have a dependence on galaxy mass (e.g. Kauffmann et al. 2003b; Gallazzi et al. 2005; Thomas et al. 2010; McDermid et al. 2015), however age–M_D (Figure 2.3d) shows only a weak correlation, and a large residual trend with size. Age–M_D also has a lower Spearman coefficient than M_D/R_e and M_D/R_e^2. Focusing instead on Σ, we see that age–M_D/R_e^2 has the lowest $RMS_G = 0.200$, highest Spearman coefficient $\rho_S = 0.570$, and a residual trend with size statistically consistent with zero (within 1σ). M_D/R_e^2 and M_D have the same observational uncertainty, which is by construction greater than the uncertainty for M_D/R_e. The notably lower RMS for age–M_D/R_e^2 therefore implies the intrinsic scatter in this trend must also be significantly lower. We find consistent results for the photometric estimators; M_*/R_e^2 has the lowest intrinsic scatter and largest ρ_S. However there are large residual trends with size for all three photometric parameters, likely due to the large scatter in the age measurements.

2.3.4. $\alpha-$ Enhancement

Lastly, Figure 2.4 shows the results for [α/Fe]. Of the three structural parameters investigated, the [α/Fe]–M relations are the weakest. The [α/Fe]–M trends (Figures 2.4a and 2.4d) have the lowest Spearman coefficients and highest RMS values. On the other hand, it is unclear whether [α/Fe] trends better with Φ or Σ. Overall, the [α/Fe]–Φ relation tends to have less residual trend with size compared to [α/Fe]–Σ: a_r = -0.09 and -0.03 for Figures 2.4b and 2.4e compared to 0.11 and 0.18 for Figures 2.4c and 2.4f. The difference is only marginal, and for the other measures (RMS_G, RMS_{rm}, and ρ_S) there is no clear improvement of one

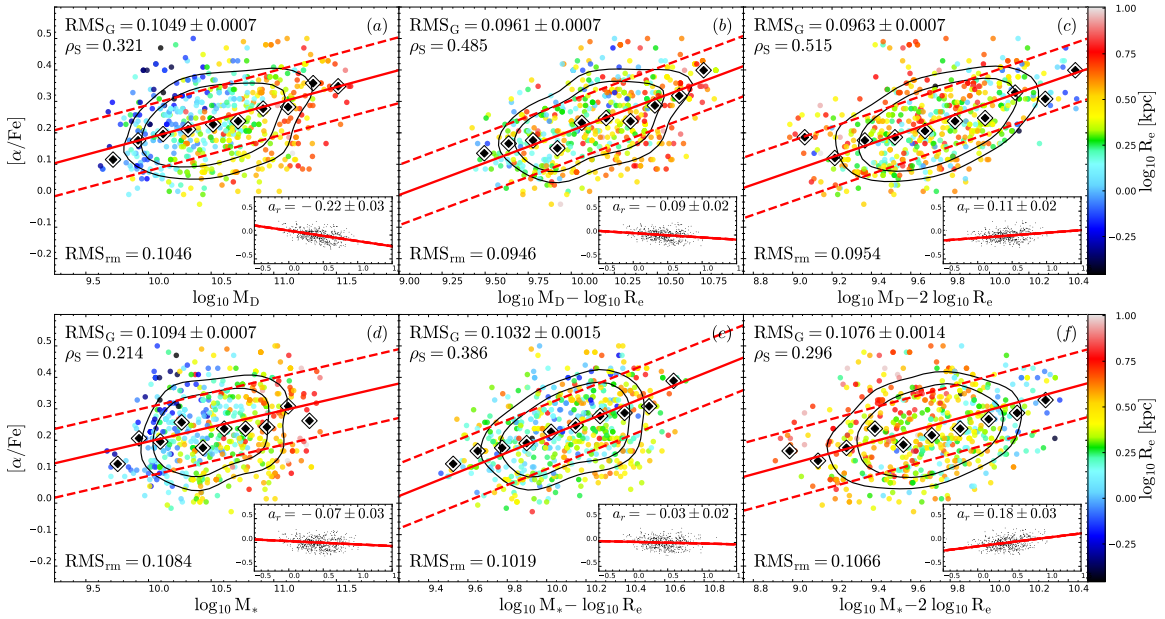

Figure 2.4 [α/Fe] versus M, Φ, and Σ for ETGs. The top row uses the spectroscopic estimator $M_D \propto \sigma^2 R_e$, the bottom row uses the purely photometric M_*. The inset panels show the best-fit residuals (data - best-fit) as a function of $\log R_e$ (other details as for Figure 1). It is unclear whether [α/Fe] trends better with Φ (panels b and e) or Σ (panels c and f), although both show significant improvement on the [α/Fe]–M relations (panels a and d).

over the other. The same is true for the results of the mass-function weighted analysis (see Table 2.1); the [α/Fe]–Φ relations have slightly lower RMS values, but the strength of ρ_S and the residual trends with radius are the same within the uncertainties. It is clear that both mass *and* size are important in determining [α/Fe], however from these results it is not clear whether Φ or Σ better represents this dependence.

2.4. Discussion

For each stellar population (SP) parameter we compared the correlations with each of M, Φ, and Σ in three ways. Firstly, we use the RMS values, in conjunction with the relative observational uncertainty on the parameters, to understand the relative intrinsic scatter. Secondly, we fit the residuals of the Gaussian model as a function of galaxy size, and use the value of the slope to determine which structural parameter best encapsulates the SP parameter's dependence on size. Thirdly, we use the Spearman correlation coefficient ρ_S as a nonparametric assessment of the strength of the correlations. We find our log-linear relations to be adequate representations of the data, as indicated by the linearity of the running median and the similarity of the RMS values for the Gaussian model and running median fits. Given this, we are able to compare the RMS values for different fits to determine which structural parameter is the best predictor for the stellar population parameter in each case.

From our analysis, we find clear results which show that the SP parameters $g - i$ colour and stellar metallicity [Z/H] correlate best with the depth of the gravitational potential Φ, while SP age trends best with surface density Σ. On the other hand, the results for [α/*Fe*] are not

so clear; the $[\alpha/\mathrm{Fe}]$-Φ relations are only slightly better than $[\alpha/\mathrm{Fe}]$-Σ, although both are appreciably better than the relations with M.

Wake et al. (2012), Thomas et al. (2010) and Graves et al. (2009a) found that galaxy colour and $[\mathrm{Z/H}]$ correlate better with σ than with either M_* or M_D, and the Age-Σ relation was explored recently by Scott et al. (2017). Our analysis builds on these works and others by: (i) quantitatively analysing residual trends with galaxy size; (ii) comparing the observational uncertainty on the parameters to deduce the relative intrinsic scatter in the relations; and (iii) showing that trends with σ are reproduced using the purely photometric estimator for the gravitational potential, M_*/R_e.

By understanding the relative intrinsic scatter, we can infer the likelihood of parameters being causally linked. However, without a theoretical framework of the physical processes driving these trends, it remains uncertain whether these correlations represent causation, or are the result of some other underlying trend. We therefore present possible frameworks, while acknowledging that more work is required to determine the true physical impact of these mechanisms in relation to other galactic processes.

2.4.1. Sample Selection

We find very close agreement between the results for the unweighted SAMI sample and the weighted sample representing the galaxy mass function. For $g-i$ colour, $[\mathrm{Z/H}]$, and age, the correlations which show the least scatter, least residual trend with size, and highest correlation coefficient in the main analysis are the same as those in the mass-function weighted analysis. The two samples also agree in that Φ shows only a marginal improvement compared to Σ for $[\alpha/\mathrm{Fe}]$.

2.4.2. Colour-Φ Diagram

Due to the tighter relations in both the RS and BC, we infer that the colour-Φ diagram is a more precise tool than the traditional colour-M diagram for identifying a galaxy's evolutionary type. The RS and BC are better aligned in colour-Φ space, indicating a smoother transition between the two populations. Furthermore, the significant residual trend with size in the colour–M diagram, indicates galaxy size as well as mass (in the form M/R_e) is required to accurately determine observed colour.

2.4.3. Metallicity-Φ Relation

We suggest the stronger correlation between $[\mathrm{Z/H}]$ and Φ (rather than M), is evidence that gravitational potential is the main regulator of global SP metallicity. The underlying physical mechanism is that the depth of the gravitational potential determines the escape velocity required for metal-rich gas to be ejected from the system. This hypothesis is supported by the tight radial trend in ETGs between local escape velocity and line strength indices (Scott et al. 2009). Assuming star formation occurs mostly *in situ* (e.g. Johansson et al. 2012), we would predict a similar relation using the gas-phase metallicity in star-forming galaxies (D'Eugenio et al. submitted). Even so, we know ETGs have long evolutionary histories that

include galaxy mergers, and this hypothesis does not, on its own, explain how the relation is maintained through mergers. However, simulations by Boylan-Kolchin & Ma (2007) of the accretion of satellite galaxies found that low-density satellites are easily disrupted, losing a large fraction of their mass during early passes at large radii; high-density satellites are more likely to survive multiple passes and continue sinking towards the center of the host. This maintains the existing [Z/H]–Φ relation, because diffuse, low–metallicity satellites will lower both the potential and metallicity of the host by adding low–metallicity material at large radii. Conversely, compact, high–metallicity satellites will carry most of their mass into the inner regions of the host, deepening the host's potential and increasing its [Z/H].

2.4.4. Age and α-Enhancement

We find strong evidence for the age-Σ relation, however it is unclear whether $[\alpha/\mathrm{Fe}]$ correlates better with Φ or Σ; the best correlation may lie somewhere between the two quantities (i.e. $[\alpha/\mathrm{Fe}] \propto M/R^x$ for $x \in [1,2]$).

Taking $[\alpha/\mathrm{Fe}]$ as a measure of star formation duration (SFD) and assuming ETGs formed approximately coevally, it follows naturally that a long SFD (low $[\alpha/\mathrm{Fe}]$) will correspond to a younger 'single-burst' SP; conversely, a short SFD (high $[\alpha/\mathrm{Fe}]$) will correspond to an older 'single-burst' SP. Thus, if ETGs are coeval, we can expect age and $[\alpha/\mathrm{Fe}]$ to correlate with the same structural parameter (whichever that may be).

To explain the origin of the correlations with Σ, we propose the following two mechanisms: (1) compactness-related quenching; and (2) the $\Sigma_{SFR} \propto \Sigma_{gas}$ relation. As we will argue below, both mechanisms appear in broad agreement with our results, although a more detailed semi-analytical approach would help resolve their relative impact on ETG stellar populations.

Quiescence correlates strongly with central surface density, regardless of the measurements used: whether quiescence is measured via specific star formation rate (sSFR; Brinchmann et al. 2004; Franx et al. 2008; Barro et al. 2013; Woo et al. 2015; Whitaker et al. 2017), via the fraction of red sequence galaxies (f_q; Omand et al. 2014), or some other measure of star formation history (e.g. the D_n4000 break; Kauffmann et al. 2003a). Woo et al. (2015) proposed two main quenching pathways which act concurrently but on very different timescales: central compactness-related processes are rapid, while halo quenching is prolonged. Compactness-related processes are those which, as a direct or indirect consequence of building the central bulge, contribute to quenching. For example, gaseous inflows from the disk to the bulge, triggered by disk instability or an event such as a major merger, are exhausted in a star burst, leading to an increased bulge compactness. Furthermore, these inflows can trigger active galactic nuclei, from which the feedback heats and blows away surrounding gas preventing further star formation. In this scenario of compactness-related quenching, it follows that galaxies with a high Σ (i.e. compact star formation) quenched faster and hence earlier, resulting in an older SP and a shorter SFD than their diffuse counterparts. This leads naturally to the age-Σ and $[\alpha/\mathrm{Fe}]$-Σ relations in ETGs.

Alternatively, given age–Σ and $[\alpha/\mathrm{Fe}]$–Σ, we could look to the $\Sigma_{gas} \propto \Sigma_{SFR}$ relation (e.g. Schmidt 1959; Kennicutt 1998; Federrath et al. 2017) for an empirical explanation. A high

Σ_{gas} in star-forming disks produces a high specific star formation rate (SFR), and (due to the finite supply of gas) this then leads to a short SFD, and hence an old SP age. This trend with Σ_{gas} in the BC becomes fossilized as a trend in Σ_* and Σ_D in ETGs.

However, neither of these two mechanisms explain why $[\alpha/\mathrm{Fe}]$ also trends strongly with Φ. A possible interpretation is that the extent to which $[\alpha/\mathrm{Fe}]$ correlates with Φ and not Σ, indicates the extent to which these galaxies are not coeval, and the time since formation as a function of mass and/or size. The residuals of the Gaussian fit in Figures 2.4c and 2.4f show that at fixed Σ, larger galaxies have higher $[\alpha/\mathrm{Fe}]$, and hence shorter star-formation histories. Future analyses could focus on analytic or semi-analytic modeling to explain these trends.

2.5. Summary

Our analysis builds on Franx et al. (2008) and Wake et al. (2012), arguing that the evolution of stellar populations is driven by physical parameters other than galaxy mass. We find the tightest correlations, and the least residual trend with galaxy size, for the $g-i$ colour–Φ, $[\mathrm{Z/H}]$–Φ, and age–Σ relations. We find $[\alpha/\mathrm{Fe}]$ to correlate strongly with both Σ and Φ. We show that correlations with σ are reproduced using the purely photometric M_*/R_e. From these results, our inferences and interpretations are that: (1) the colour–Φ diagram is a more precise tool for determining the developmental stage of the stellar population than the colour–mass diagram; (2) gravitational potential is the primary regulator for global stellar metallicity, via its relation to the gas escape velocity. We also propose two possible mechanisms for the age–Σ and $[\alpha/\mathrm{Fe}]$–Σ correlations: the age–Σ and $[\alpha/\mathrm{Fe}]$–Σ correlations are results of compactness-driven quenching mechanisms; and/or the correlations are fossil records of the $\Sigma_{SFR} \propto \Sigma_{gas}$ relation in their disk-dominated progenitors. Determining which of the various possible physical mechanisms are responsible for these relations requires comparison to detailed simulations that take into account of all these processes.

CHAPTER 3

Low-Redshift Star-Forming Galaxies

The work presented in this chapter has been previously published as 'Gravitational Potential and Surface Density Drive Stellar Populations. II. Star-forming Galaxies', Barone, Tania M.; D'Eugenio, Francesco; Colless, Matthew; Scott, Nicholas, 2020, ApJ, 898, 62B.

3.1. Introduction

In this Chapter we build on the results on stellar populations in early-type galaxies presented in Chapter 2 by studying the ages and metallicities of star-forming galaxies and how they correlate with stellar mass (M_*), gravitational potential ($\Phi \propto M_*/R_e$) and surface mass density ($\Sigma \propto M_*/R_e^2$).

In Chapter 2, we showed that correlations with σ are reproduced using the purely photometric estimator of potential M_*/R_e. We found the tightest correlations, and the least residual trend with galaxy size, for the $g-i$ colour–Φ, [Z/H]–Φ, and age–Σ relations. We found $[\alpha/\mathrm{Fe}]$ to correlate strongly with both Σ and Φ. From these results we concluded that: (1) the colour–Φ diagram is a more precise tool for determining the developmental stage of a stellar population than the colour–M diagram; and (2) Φ is the primary regulator for global stellar metallicity, via its relation to the gas escape velocity. This explanation is further supported by the recent results of D'Eugenio et al. (2018), who showed that gas-phase metallicity in star-forming galaxies (SFGs) is also more tightly correlated with Φ than either M or Σ. With regards to the age–Σ and $[\alpha/\mathrm{Fe}]$–Σ correlations, we proposed two possible explanations: either they are the result of compactness-driven quenching mechanisms or they are fossil records of the $\Sigma_{SFR} \propto \Sigma_{gas}$ relation in their disk-dominated progenitors (or some combination of these). To determine which of the various possible physical mechanisms are responsible, we need to know whether these scaling relations are also present in earlier phases of galaxy evolution, while they are still forming stars.

In Section 3.2 we detail the sample selection, and why the dataset used has changed from Chapter 2. Section 3.3 describes the full spectral fitting method used to measure the stellar population ages and metallicities. In Section 3.4 we present our analysis methods and results for the luminosity-weighted parameters, and in Section 3.5 we present the mass-weighted results. In Section 3.6 we discuss our results and the possible mechanisms responsible, and qualitatively compare to the results presented in Chapter 2. Finally we provide a summary in Section 3.7. Although we perform both luminosity-weighted and mass-weighted fits, we focus predominantly on the luminosity-weighted parameters. Given the galaxies in our sample are star-forming, their spectra are dominated by young stars and so the contribution from low-luminosity old stars is not well constrained, making it difficult to recover the true mass-weighted parameters. Throughout this Chapter we use the terms 'early' and 'late' type to refer to a visual morphological classification, whereas 'quiescent' and 'star-forming' are based on measured star formation rates. While early-type and star-forming are not mutually exclusive categories, we note that the overlap between them is small. Only 7% of early-types in our sample from Chapter 2 would also be classified as star-forming. Therefore for our purposes the categories can be considered disjoint.

3.2. Sample Selection

All data used in this Chapter is publicly available and based on the SDSS Legacy Survey (York et al. 2000; Strauss et al. 2002). An electronic table of the catalog data as well as our derived stellar population parameters is available online, and is described in Table 3.2. For our stellar population measurements we use optical spectra from Data Release 7

(Abazajian et al. 2009). We use r-band effective radii (R_e) from Simard et al. (2011), as they provide both single and various double Sérsic fits as well as an F-test probability to determine the most appropriate model for each galaxy. To convert from apparent to physical size we use the spectroscopic redshifts given by the SDSS pipeline and assume the standard ΛCDM cosmology. We use H_α-derived specific star formation rates (sSFR; Brinchmann et al. 2004) from the MPA/JHU catalog, and select star-forming galaxies as having a total sSFR $> 10^{-11.0}\mathrm{M}_\odot\mathrm{yr}^{-1}$, and 'star forming' locations on the BPT diagram (Baldwin et al. 1981; Veilleux & Osterbrock 1987; Kewley et al. 2001; Kauffmann et al. 2003c; Schawinski et al. 2007a) as defined by Thomas et al. (2013). To ensure reliable stellar population measurements, we select spectra with a median spectral signal-to-noise ratio ≥15 per Å. We use stellar masses (M_*) from Kauffmann et al. (2003a) and Salim et al. (2007), which are derived from spectral energy distribution (SED) fitting. The M_* from Kauffmann et al. (2003a) are based on a Kroupa (2001) initial mass function (IMF), whereas the stellar population models use a Chabrier (2003) IMF. Hence we rescale M_* to a Chabrier (2003) IMF using the conversion from Madau & Dickinson (2014), $\log M_{\mathrm{Chabrier}} = \log M_{\mathrm{Kroupa}} - 0.034$.

We compare M_* from Kauffmann et al. (2003a) with M_* derived from our full spectral fits, as well as the M_* derived by Chang et al. (2015) using SDSS spectra and photometry from the Wide-field Infrared Survey Explorer (WISE; Wright et al. 2010), and find good agreement between all three measurements. We prefer to use a partially independent measure of M_* rather than the values derived from our full spectral fits to reduce the correlated errors between M_* and the stellar population parameters. The stellar masses derived by Chang et al. (2015) use the radius measurements by Simard et al. (2011) that we also use in our fits, so to reduce the effect of correlated errors between M_* and R_e artificially tightening the trends, we use M_* from Kauffmann et al. (2003a). We note, however, that our results are quantitatively unchanged if we instead use the stellar masses from Chang et al. (2015) or from our full spectral fits.

In Chapter 2 we used a different dataset, namely 625 ETGs from the Sydney-AAO Multi-object Integral-field (SAMI) galaxy survey (Croom et al. 2012; Bryant et al. 2015; Scott et al. 2018). However, the comparatively extended ongoing star formation in SFGs leads to a higher intrinsic scatter in single-burst parametrizations, so here we require a larger sample than SAMI provides in order to determine the same scaling relations.

3.2.1. Aperture Matched Sampling

We employ the technique of Aperture-Matched Sampling (AMS) used by D'Eugenio et al. (2018), in which galaxies are selected to have similar physical areas encompassed by the fiber aperture. This technique allows us to mimic the adaptive aperture of integral field surveys while taking advantage of the large and diverse datasets of single-fiber surveys such as the SDSS Legacy Survey. The AMS approach mitigates (at the expense of sample size) the aperture bias inherent to single-fiber surveys that results from probing galaxies over varying areas depending on their apparent size. Combined with radial trends within galaxies, aperture bias can lead to spurious global trends. The aperture-matched subsample is defined by $R_e = R_{\mathrm{fiber}}(1 \pm t)$ for some small tolerance t. Following D'Eugenio et al. (2018) we use a tolerance of 13%; given the SDSS Legacy Survey fiber radius of 1.5″, this criterion selects galaxies with 1.3″$< R_e <$1.7″. Due to our aperture-matched criterion, our sample

Column Name	Units	Description
specObjID	...	SDSS Spectroscopic object ID
ObjID	...	SDSS Photometric object ID
Plate	...	SDSS Plate ID
MJD	...	Modified Julian Date of observation
FiberID	...	SDSS Fiber ID
Redshift	...	SDSS spectrscopic redshift
log_Age_L	$\log_{10}$ Gyr	Luminosity-weighted age
log_Age_L_unc	$\log_{10}$ Gyr	Uncertainty on luminosity-weighted age
ZH_L	...	Luminosity-weighted total metallicity
ZH_L_unc	...	Uncertainty on luminosity-weighted total metallicity
log_Age_M	$\log_{10}$ Gyr	Mass-weighted age
log_Age_M_unc	$\log_{10}$ Gyr	Uncertainty on mass-weighted age
ZH_M	...	Mass-weighted total metallicity
ZH_M_unc	...	Uncertainty on mass-weighted total metallicity
log_Mstar	$\log_{10} M_\odot$	Stellar Mass from Kauffmann et al. 2003
log_Mstar_unc	$\log_{10} M_\odot$	Uncertainty on Stellar Mass from Kauffmann et al. (2003a)
Re	kpc	Circularised effective radius in r-band from Simard et al. (2011)

Table 3.1 Description of the table containing our derived stellar population parameters along with the stellar masses from Kauffmann et al. (2003a), and effective radii from Simard et al. (2011). This table is available in its entirety in a machine-readable form in the online journal.

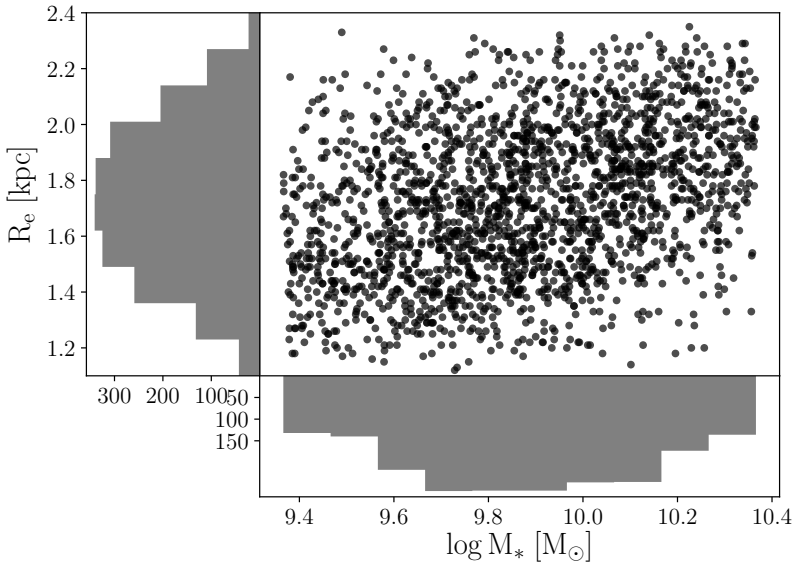

Figure 3.1 Mass–size plane for the sample of SDSS galaxies used here. The sample is approximately evenly distributed in R_e at fixed M_*, which reduces bias when determining the dependence of stellar population parameters on size.

has a correlation between galaxy size and redshift. We therefore also require a sample with a narrow range in redshift to remove the effect of our results being due to evolution with redshift rather than dependence on size. We select galaxies with spectroscopic redshifts $0.043 < z < 0.073$.

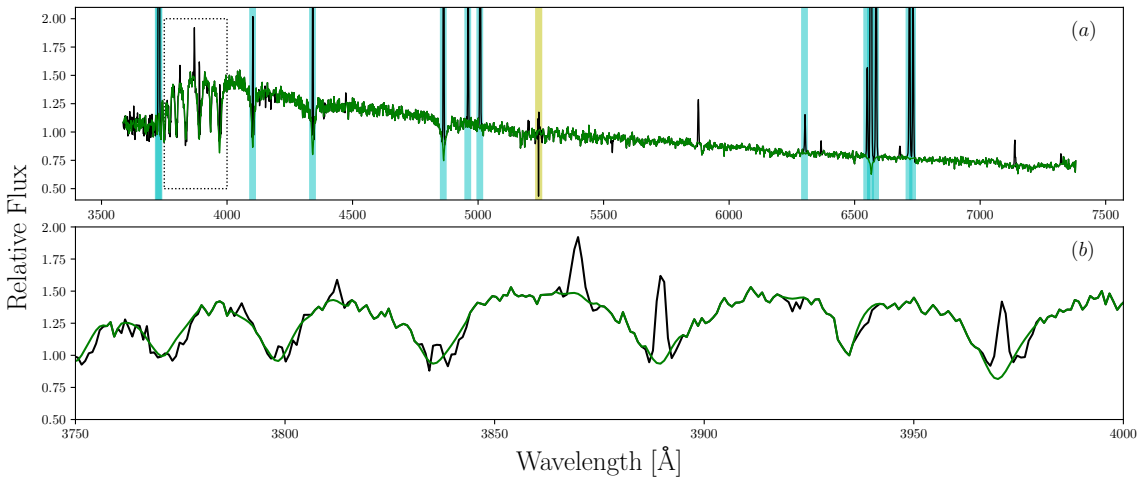

Figure 3.2 The rest-frame original spectrum for galaxy spec-0541-51959-0600 (black line) and the spectrum used for the stellar population template fitting (green line) that has gas emission lines, sky lines, and discrepant pixels masked. Panel (a) shows the entire wavelength range, panel (b) shows a close-up of the region covering the higher order Balmer lines (indicated by a black dotted box in panel a). The cyan regions are emission lines explicitly masked using the pPXF function `determine_goodpixels`, and the yellow region is the 5577Å sky line that is also explicitly masked. Any remaining emission lines or discrepant pixels are identified and masked by the CLEAN function in pPXF, which iteratively rejects pixels that deviate more than 3σ from the best-fit and refits until no further pixels are clipped (Cappellari et al. 2002). The higher-order Balmer lines are not explicitly masked, because not all spectra have emission in these regions. However as shown in panel (b), the method used effectively identifies remaining emission lines and masks them, recovering the shape of the underlying absorption feature.

3.2.2. Mass-Limited Sample

In order to investigate the relative importance of mass and size in predicting stellar population parameters, it helps for the sample to have a similar size distribution at any fixed mass, so there is less in-built mass–size correlation (see Figure 3.1). Consequently we select a mass-limited sample defined by $9.434 < \log(M_*/M_\odot) < 10.434$. The final sample still has a residual mass-size dependence in that higher mass galaxies have a larger mean size, as removing this completely would severely compromise sample size. While the distribution of sizes at the high and low mass ends of our sample are not identical, the change in the range of sizes is small; the mean size of the galaxies in the lowest and highest mass bins in Figure 3.1 (of width 0.1 dex) are 1.58 and 1.88 kpc respectively.

3.3. Stellar Population Synthesis

We measure the stellar population parameters from full spectral fits using theoretical stellar population models based on the Medium resolution INT Library of Empirical Spectra (MILES; Sánchez-Blázquez et al. 2006b; Vazdekis et al. 2010, 2015), using BaSTI isochrones (Pietrinferni et al. 2004, 2006) and a Chabrier (2003) initial mass function. This is different from the Lick index method and models used in Chapter 2. The stellar population parameters for Chapter 2 were measured by Scott et al. (2017) using the popular Lick system of absorption line indices and the models by Schiavon (2007) and Thomas et al. (2011), as Lick indices afford a benchmark for the analysis of ETG (and globular cluster) populations

(Faber 1973). The little-to-no ongoing star formation in ETGs means the spectral absorption lines are free from emission by ionised interstellar gas, allowing for precise measurements. In contrast, SFGs have emission from ionized gas contaminating the absorption features, making it difficult to make accurate measurements. Nevertheless, with high signal-to-noise spectra and careful masking of emission lines, Ganda et al. (2007) and Peletier et al. (2007) were able to find scaling relations with mass and velocity dispersion similar to those found in ETGs.

However, an alternative is to use sets of theoretical spectra for single-age and single-metallicity populations that allow a full spectral fitting approach using not just a limited number of absorption features but the whole spectrum, including the shape of the continuum. In addition to the MILES models by Vazdekis et al. (2010, 2015) used here, other widely used sets of theoretical spectra include Bruzual & Charlot (2003) and Binary Population and Spectral Synthesis (BPASS; Eldridge et al. 2017; Stanway & Eldridge 2018). While these models do not account for emission from ionized gas, the issue of emission lines obscuring absorption features is less severe with a full spectral fitting method than for Lick indices, because the whole spectrum is used. We therefore use spectral fitting to approach the comparatively less well-studied field of stellar populations in star-forming galaxies.

Despite the different stellar population models used in this work (Vazdekis et al. 2010, 2015) and in Chapter 2, (Schiavon 2007; Thomas et al. 2011), there is good agreement between results from these models. McDermid et al. (2015) show that there is a tight relation between stellar population parameters derived using Lick indices and Schiavon (2007) models, and mass-weighted parameters derived from full spectral fitting and Vazdekis et al. (2010) models for ETGs. Their Figure 4 shows that the [Z/H] derived from the two models and methods closely follow the one-to-one relation. The ages follow a tight correlation offset from the one-to-one line, with the luminosity-weighted Schiavon (2007) ages being systematically younger than the mass-weighted Vazdekis et al. (2010) ages. However this is most likely a result of luminosity-weighted ages being more sensitive to young stars than mass-weighted ages (Serra & Trager 2007), rather than a difference in the models used. Additionally, Scott et al. (2017) show that there is good agreement between the Schiavon (2007) and Thomas et al. (2011) models, differing most in the low-[Z/H] regime.

Our stellar population analysis consists of two main steps: Step 1 involves masking the spectra of emission and sky lines; Step 2 involves fitting the masked spectrum as a weighted sum of single-age and single-metallicity templates.

3.3.1. Step 1. Emission Line Masking

The aim of this pre-processing stage is to mask sky and gas emission lines. We begin by de-redshifting the galaxy and masking known sky and galaxy emission lines. Specifically, we use the function `determine_goodpixels` from the Python implementation of the publicly available Penalized Pixel-Fitting software (pPXF; Cappellari & Emsellem 2004; Cappellari 2017) to mask 13 common emission lines (see pPXF documentation for emission line details). Additionally, we also mask the sky line in the region between 5565Å to 5590Å. These masked regions are highlighted in panel (a) of Figure 3.2. We then perform two fits to the masked spectrum, using pPXF and all 985 empirical stellar templates from the

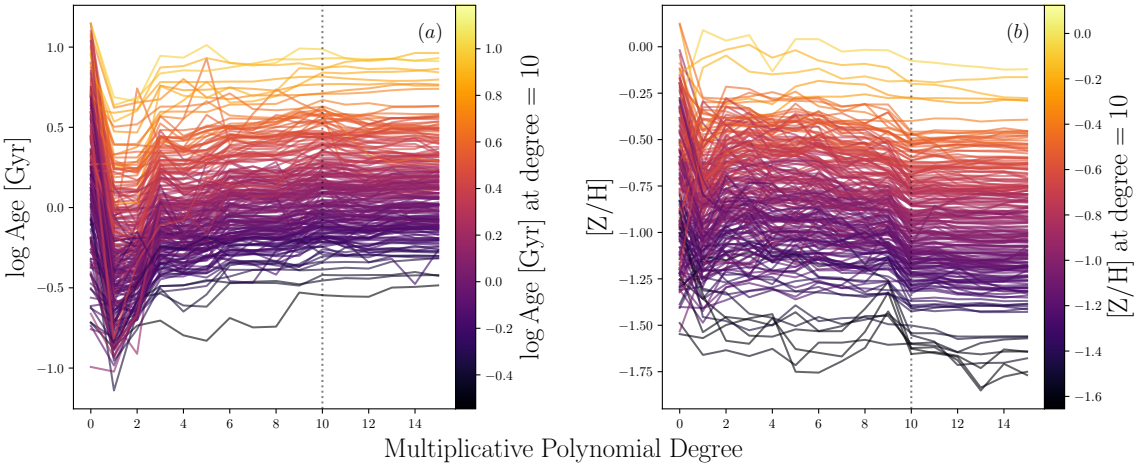

Figure 3.3 The luminosity-weighted age and [Z/H] from fits using varying degrees of the multiplicative polynomial, for a subsample of 209 galaxies. Each line is a single galaxy, and is coloured by its age (panel a) and [Z/H] (panel b) from the 10$^{\text{th}}$ degree fit. The stellar population parameters vary little above a multiplicative polynomial of degree 10, hence we use a 10$^{\text{th}}$ degree polynomial.

MILES library (Sánchez-Blázquez et al. 2006a; Falcón-Barroso et al. 2011) broadened to the SDSS instrumental resolution. The purpose of the first fit is to obtain an estimate of the noise and uses the variance given by the SDSS pipeline. Based on the χ^2_{reduced} of the first fit, we then rescale the variances to give $\chi^2_{\text{reduced}} = 1$. The median rescaling value is 0.994 with a standard deviation of 0.079. With this slightly improved noise estimate, the second fit identifies any remaining bad pixels by iteratively rejecting pixels that deviate more than 3σ from the best-fit, refitting until no further pixels are rejected (see section 2.1 of Cappellari et al. (2002) and the CLEAN keyword in the pPXF documentation). Panel (b) of Figure 3.2 demonstrates that emission lines not explicitly masked, such as the higher order Balmer lines, are identified and masked by the CLEAN iterative pixel rejection. The pixels identified as bad or containing emission lines are then replaced by the best-fit model from the second fit.

3.3.2. Step 2. Full Spectral Fitting

After the pre-processing stage, the stellar population age and metallicity are measured from the masked, emission-line-free spectrum. We fit the masked spectrum as a linear combination of synthetic single-population templates and a degree 10 multiplicative polynomial. The role of the multiplicative polynomial is to correct the shape of the continuum and account for dust extinction, however it significantly increases the computation time (Cappellari 2017). Therefore, ideally the degree of the multiplicative polynomial should be the lowest value such that both residual flux calibration errors and dust extinction are corrected for. Using a randomly selected subsample of 209 galaxies (10% of the full sample) we tested the dependence of the resulting stellar population parameters on the degree of the multiplicative polynomial used. As shown in Figure 3.3, while the absolute values of age and [Z/H] vary greatly for fits with a multiplicative polynomial degree less than 10, the relative difference between galaxies remains similar. The stellar population parameters vary little for degree ≥ 10, hence we use a degree 10 polynomial.

The templates used are from Vazdekis et al. (2010, 2015) and are constructed from the MILES stellar library and the base $[\alpha/\mathrm{Fe}]$ BaSTI isochrones (Pietrinferni et al. 2004, 2006) and a Chabrier (2003) initial mass function. The base models contain no assumption on the abundance ratios, hence the templates follow the abundance pattern of the Milky Way (Vazdekis et al. 2010). The 636 templates span an approximately regular grid in age and metallicity, spanning $-2.27 \leq [\mathrm{Z/H}] \leq 0.40$ $(0.0001 \leq Z \leq 0.040)$ and $0.03\,\mathrm{Gyr} \leq \mathrm{Age} \leq 14.0\,\mathrm{Gyr}$. We perform both luminosity-weighted (i.e. templates are individually normalised; section 3.4) and mass-weighted fits (i.e no renormalization of templates; section 3.5), however we focus the analysis and discussion predominantly on the luminosity-weighted parameters. Given the galaxies in our sample are star-forming, their spectra are dominated by young stars and so the contribution from low-luminosity old stars is not well constrained, making it harder to recover the true mass-weighted parameters. Each template is assigned a weight and from the combinations of weights a star formation history can be inferred (e.g. McDermid et al. 2015). However, the recovery of the star formation history is an ill-conditioned inverse problem without a unique solution unless further constraints are imposed (e.g. Press et al. 1987). This is because of the not-insignificant degeneracies between stellar spectra with different ages and metallicities. A common solution is to use linear regularization, which constrains the weights of neighbouring templates (in age–metallicity space) to vary smoothly. While linear regularization produces more realistic star-formation histories, typical degrees of regularization (see criterion advocated by Press et al. 1992 and used by, for example, McDermid et al. 2015; Norris et al. 2015; Boecker et al. 2020) are not expected to significantly change the weighted stellar population parameters, and we confirmed this to be the case for the luminosity-weighted age and $[\mathrm{Z/H}]$ using the random subsample of 209 galaxies. However, we did find a small systematic offset between the regularized and non-regularized parameters, in that the regularized values are on average 0.06 dex older and 0.07 dex more metal rich. This offset is introduced by regularizing over templates that are not evenly spaced in age or metallicity. The Vazdekis et al. (2010) templates have larger spacing at older ages, hence smoothing between adjacent templates results in the regularized values being slightly older. This offset is small and less than the median uncertainties on the stellar population parameters ($\sigma_{\log \mathrm{Age}} = 0.12$ dex and $\sigma_{[\mathrm{Z/H}]} = 0.10$ dex). Overall, we prefer to use the non-regularized fits in estimating the weighted ages and metallicities.

Estimating Uncertainties

We derive uncertainties on the luminosity-weighted stellar population parameters as a function of the median S/N per pixel, derived from testing performed on the same 209 galaxies used to test the degree of the multiplicative polynomial. First, we shuffle the residuals from the best-fit within 7 bins approximately 500Å wide, and add this to the best-fit spectrum and refit, repeating 100 times per galaxy. The resulting stellar population parameter distribution is approximately Gaussian and centred around the original fit. Hence we take the standard deviation of the distribution as the uncertainty on the stellar population parameter. Figure 3.4 shows the dependence of the measured uncertainty on the median spectral S/N for the 209 test galaxies. Both the uncertainty on age and $[\mathrm{Z/H}]$ show an inverse dependence on S/N, which we fit using the Levenberg-Marquardt least-squares optimization algorithm implemented in Python by the `SciPy` package's `optimize.curve_fit` routine

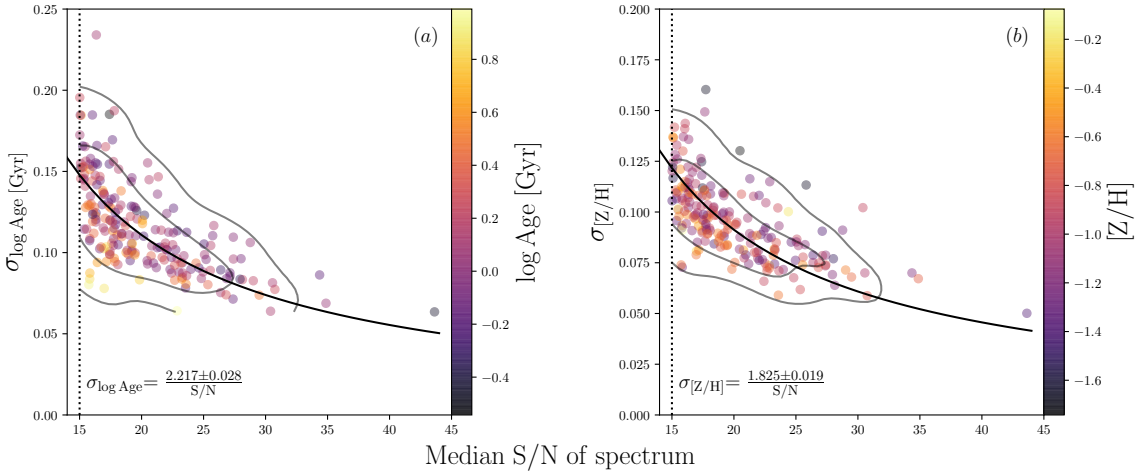

Figure 3.4 Uncertainty on luminosity-weighted age and [Z/H] versus median S/N of the spectrum for the subsample of 209 test galaxies. Each point is coloured by its age (panel a) and [Z/H] (panel b). The grey contours enclose 95% and 68% of the data. In both panels the black line is the best-fit inverse relation, which is then used to assign an uncertainty on age and [Z/H] to every galaxy in the full sample, based on its spectral S/N.

(Virtanen et al. 2020). We then use these relations, $\sigma_{\log \mathrm{Age}} = \frac{2.217}{S/N}$, and $\sigma_{[Z/H]} = \frac{1.825}{S/N}$ to assign uncertainties to the age and [Z/H] of each galaxy based on its S/N.

Unlike the luminosity-weighted parameters, the mass-weighted stellar population parameters do not show a strong variation with S/N, and show greater scatter at fixed S/N. Therefore, rather than assigning an uncertainty to each galaxy based on its S/N, we use the median uncertainties from the test subsample, $\sigma_{\log \mathrm{Age}} = 0.096$ and $\sigma_{[Z/H]} = 0.18$, and use these values for every galaxy in the sample.

3.4. Luminosity-Weighted Ages and Metallicities

3.4.1. Fitting Method

We fit both two-parameter lines $z = a_0 + a_1 x$ and three-parameter planes $z = a_0 + a_1 x + a_2 y$ to the relationships between stellar population parameters (age and metallicity) and structural properties (M_*, R_e and the combinations Φ and Σ), allowing for intrinsic scatter in the z direction (i.e. in the stellar population parameter). These fits are performed using a Bayesian approach with uniform priors on the slope(s), intercept, and intrinsic scatter.

The posterior function is first optimised using the Differential Evolution numerical method (Storn & Price 1997; Price et al. 2005), followed by Markov Chain Monte Carlo integration (Goodman & Weare 2010) of the posterior distribution to estimate the uncertainties on each model parameter using the Python package `emcee` (Foreman-Mackey et al. 2013).

For both the line and plane fits we quantify the residuals as a function of R_e, as displayed in the inset at the bottom right of each panel. In conjunction with the plane fit (where the residual correlation is close to zero by construction), the slopes of the residual correlations illustrate which of M_*, Φ or Σ best encapsulates the stellar population parameter's dependence on size.

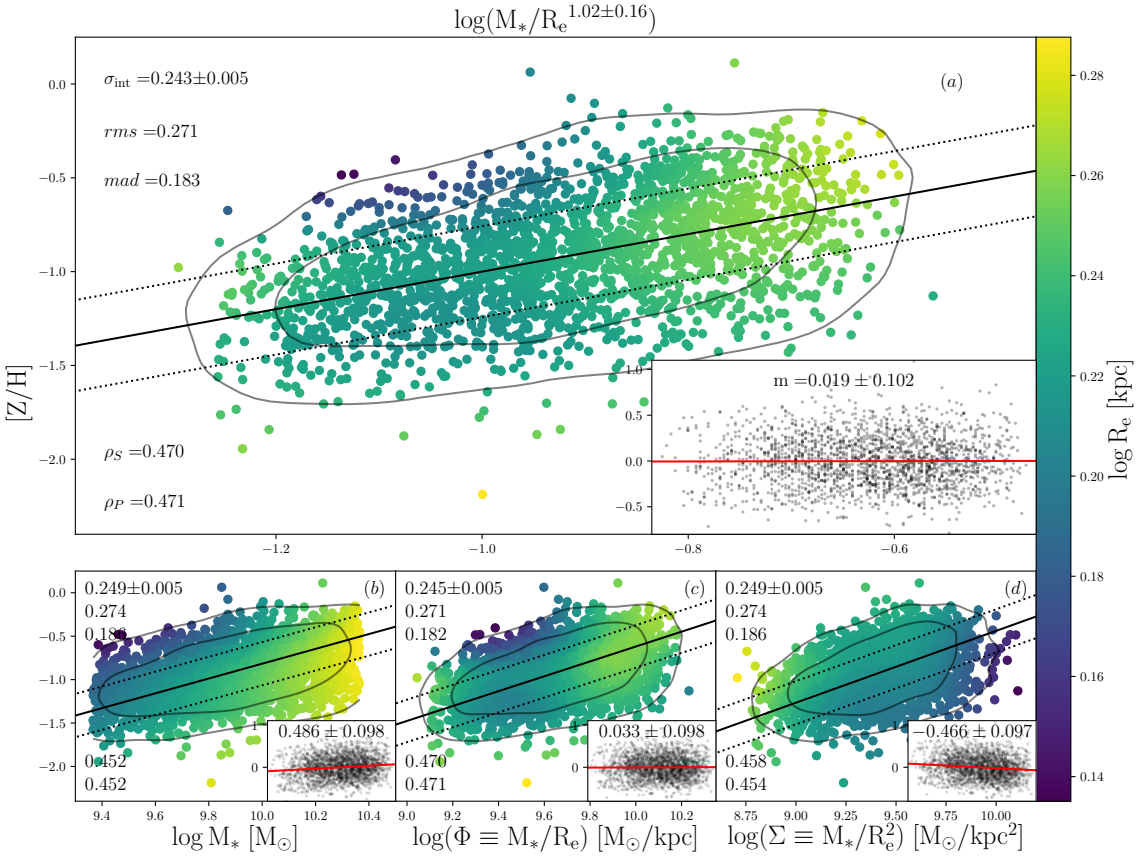

Figure 3.5 Luminosity-weighted [Z/H] versus the best-fit linear combination of M_* and R_e (panel a) and luminosity-weighted [Z/H] versus M_*, $\Phi \equiv M_*/R_e$ and $\Sigma \equiv M_*/R_e^2$ (panels b–d). In each panel the solid black line is the best-fit linear relation and the dashed lines indicate the intrinsic scatter σ_{int} about this fit. The colourscale indicates the LOESS-smoothed value of $\log R_e$ (in kpc). The scatter, both root-mean-square (*rms*) and median absolute deviation (*mad*), is given at the top left of each panel and the correlation coefficient, both Spearmam ρ_S and Pearson ρ_P, is given at the bottom left. The contours enclose 68% and 95% of the sample. The insets show the best-fit residuals (bestfit - data) versus $\log R_e$; the slope of the residual trend m is displayed at the top of each inset. Panels (a) and (c) indicate that of the three structural parameters studied, [Z/H] correlates best with Φ.

For each relation we use several metrics to quantify both the significance of the correlation and the tightness of the scatter about the fit. The Spearman and Pearson correlation coefficients (ρ_S, ρ_P) characterise the significance, while the root-mean-square (*rms*) scatter and median absolute deviation (*mad*) about the fit quantify the tightness. The absolute *intrinsic* scatter in the relations is difficult to measure, because it is sensitive to the assumed observational uncertainties. However, given the non-zero observational uncertainty on R_e, it follows that $M_* R_e^i$ necessarily has a higher total observational uncertainty than M_* alone (for $i \neq 0$). Moreover, if $M_* R_e^j$ shows less scatter than $M_* R_e^i$ for $j > i$, $M_* R_e^j$ must be intrinsically tighter. Hence, by understanding the relative observational uncertainties, we can compare the measured scatter about the fits and rank the relations based on their relative intrinsic scatter. The colourscales in the figures show $\log R_e$, smoothed using the locally weighted regression algorithm LOESS (Cleveland & Devlin 1988; Cappellari et al. 2013), to highlight the residual trends with galaxy size.

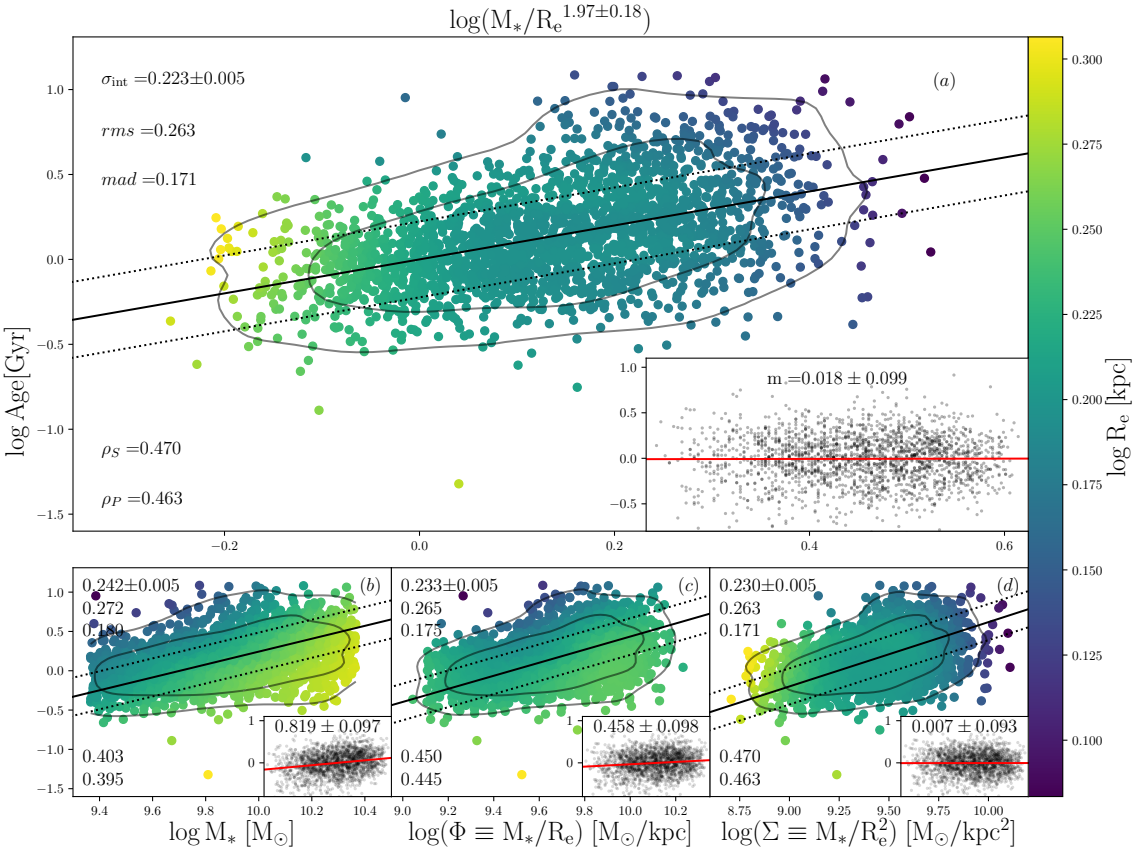

Figure 3.6 Luminosity-weighted age versus the best-fit linear combination of M_* and R_e (panel a), and luminosity-weighted age versus M_*, $\Phi \equiv M_*/R_e$ and $\Sigma \equiv M_*/R_e^2$ (panels b–d). In each panel the solid black line is the best-fit linear relation and the dashed lines indicate the intrinsic scatter σ_{int} about this fit. The colourscale indicates the LOESS-smoothed value of $\log R_e$ (in kpc). The scatter, both root-mean-square (*rms*) and median absolute deviation (*mad*), is given at the top left of each panel and the correlation coefficient, both Spearmam ρ_S and Pearson ρ_P, is given at the bottom left. The contours enclose 68% and 95% of the sample. The insets show the best-fit residuals (bestfit - data) versus $\log R_e$; the slope of the residual trend m is displayed at the top of each inset. Panels (a) and (d) indicate that of the three structural parameters studied, age correlates best with Σ.

3.4.2. Metallicity [Z/H]

We show the results of this analysis for [Z/H] in Figure 3.5. Of the three structural parameters, [Z/H]–Φ in panel (c) has the tightest correlation. Indeed, the plane fit in panel (a) shows that the optimum coefficient of $\log R_e$ is -1.02 ± 0.16, consistent within the uncertainties to the -1 coefficient corresponding to Φ. Furthermore for the [Z/H]–Φ relation, the σ_{int}, *rms* and *mad* are all consistent within the uncertainties to the plane fit. Moving from left to right in Figure 3.5 from M_* (panel b) through Φ (panel c) to Σ (panel d), we see a peak in ρ_P and ρ_S, as well as a minimum in σ_{int}, *rms* and *mad* at Φ (panel c). Invoking the argument given above, the larger *observational* uncertainties in [Z/H]–Φ compared to [Z/H]–M_*, along with slightly less scatter, implies [Z/H]–Φ must have less *intrinsic* scatter than [Z/H]–M_*.

In addition to the tightness of the fits, the residual trends with $\log R_e$ indicate which of the parameters investigated best encapsulates the dependence of [Z/H] on size. The [Z/H]–M_* diagram in panel (b) and the [Z/H]–Σ diagram in panel (d) both show significant residual

trends with size. As shown by the inset panels, the slopes of the residuals of [Z/H]–M_* and [Z/H]–Σ with size are $m = 0.486 \pm 0.098$ and $m = -0.466 \pm 0.097$ respectively. On the other hand, the [Z/H]–Φ relation shows no residual trend with size ($m = 0.033 \pm 0.098$). This lack of residual trend with size indicates that Φ best encapsulates the relative dependence of [Z/H] on mass and size.

The results are quantitatively unchanged if we instead use M_* from Chang et al. (2015). The plane fit using M_* from Chang et al. (2015) is $[Z/H] \propto M_*/R_e^{1.00\pm0.13}$, consistent within the uncertainties to our presented results $[Z/H] \propto M_*/R_e^{1.02\pm0.16}$ using M_* from Kauffmann et al. (2003a).

3.4.3. Age

In Figure 3.6, panels (b)-(d) show the relations between age and M_*, Φ and Σ, while panel (a) shows age fitted by a plane in M_* and R_e. For the plane fit, the optimum coefficient of $\log R_e$ is -1.97 ± 0.18, consistent within the uncertainties to the -2 coefficient corresponding to Σ, indicating that despite the high intrinsic scatter and observational uncertainties, age scales most closely with surface mass density Σ. Indeed the improvement of the plane fit (panel a) over the age–Σ relation (panel d) is marginal, as indicated by the identical values of ρ_S and ρ_P. Moving from left to right in Figure 3.6 from M_* (panel b) through Φ (panel c) to Σ (panel d), we see a consistent decrease in the scatter, *rms*, *mad* and residual slope, along with a corresponding increase in ρ_P and ρ_S. Given the higher observational uncertainty of Σ compared to M_* or Φ, the tighter correlation with Σ implies a fundamentally closer relationship.

Both the age–M_* (panel b) and age–Φ (panel c) relations show significant positive residual trends with size, $m = 0.819 \pm 0.097$ and $m = 0.458 \pm 0.098$ respectively, whereas the age–Σ residuals (panel d) shows no trend with size ($m = 0.007 \pm 0.093$). This lack of residual trend with size indicates that Σ best encapsulates the relative dependence of age on mass and size.

If we instead use M_* from Chang et al. (2015) rather than Kauffmann et al. (2003a), our results remain quantitatively unchanged. The plane fit using M_* from Chang et al. (2015) is age $\propto M_*/R_e^{1.90\pm0.16}$, consistent within the uncertainties to age $\propto M_*/R_e^{1.97\pm0.18}$ using M_* from Kauffmann et al. (2003a).

3.5. Mass-Weighted Ages and Metallicities

Here we present the mass-weighted stellar population measurements and analyse their dependence on mass and size, to investigate whether the results presented for the luminosity-weighted parameters ($[Z/H]_L$ and age_L) in section 3.4 hold when using mass-weighted parameters ($[Z/H]_M$ and age_M). Unlike $[Z/H]_L$ and $\log age_L$ which show linear dependencies on $\log M_*$, $\log \Phi$, and $\log \Sigma$, both $[Z/H]_M$ and $\log age_M$ show a non-linear dependence on these parameters. We are therefore unable to apply to the mass-weighted parameters the linear fitting method (described in section 3.4) that we used for the luminosity-weighted parameters. Instead, we analyse the dependence of the mass-weighted parameters on $\log M_*$, $\log \Phi$ and $\log \Sigma$ by showing how $[Z/H]_M$ and $\log age_M$ vary in the mass–size plane.

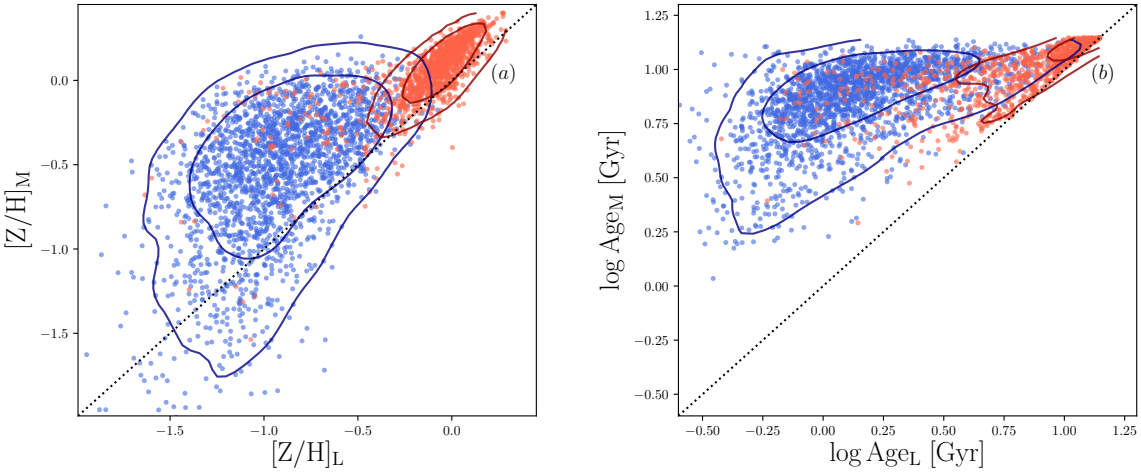

Figure 3.7 Comparison of mass-weighted and luminosity-weighted [Z/H] (panel a) and age (panel b). Blue points are star-forming galaxies, red points are early-type galaxies from the MOSES catalog. The black dotted line shows the 1-1 relation. The contours enclose enclose 68% and 95% of each sample.

First, in Figure 3.7 we compare the mass-weighted and luminosity-weighted parameterizations for both our sample of star-forming galaxies, and an additional sample of early-type galaxies. For the early-types, we use an aperture-matched subsample (following the same criteria described in section 3.2.1) of 1266 galaxies from the MOrphologically Selected Early-types in SDSS (MOSES; Schawinski et al. 2007a; Thomas et al. 2010) catalog. Similarly, Figure 4 of McDermid et al. (2015) compares mass-weighted [Z/H] and age derived from full spectral fitting to single stellar population (SSP) parameters measured from Lick indices for early-type galaxies from the ATLAS^{3D} survey (Cappellari et al. 2011). Given SSP parameters are expected to closely follow luminosity-weighted parameters (Serra & Trager 2007), we compare our results with those of McDermid et al. (2015).

We then show how the the mass-weighted parameters depend on mass and size by how they vary in the mass–size plane (Figure 3.8 for [Z/H] and Figure 3.9 for age). We include the luminosity-weighted parameters in Figures 3.8 and 3.9 for reference. To visually highlight the underlying trends we use the LOESS (Cleveland & Devlin 1988; Cappellari et al. 2013) algorithm. We compare our luminosity-weighted mass–size planes to similar figures by Scott et al. (2017) and Li et al. (2018). Specifically, we compare to Figures 9 and 10 of Scott et al. (2017) which show how SSP parameters for SAMI galaxies vary in the mass–size plane, and Figure 4 of Li et al. (2018) who show how luminosity-weighted parameters vary in the mass–size plane for galaxies from the Mapping Nearby Galaxies at APO(MaNGA; Bundy et al. 2015) survey.

3.5.1. Metallicity [Z/H]

Luminosity-weighted metallicity depends mostly on the old stellar population (Serra & Trager 2007), and so we expect good agreement between $[Z/H]_L$ and $[Z/H]_M$. For early-types (red points in Figure 3.7 a) there is a clear 1-1 relation, although unlike Figure 4. of McDermid et al. (2015) there is a small zero-point offset, with $[Z/H]_M$ being on average 0.16 dex more metal rich than $[Z/H]_L$. However this 1-1 relation appears limited to above $[Z/H]_L \approx -0.5$, below which there is a significant bend seen strongly in the star-forming

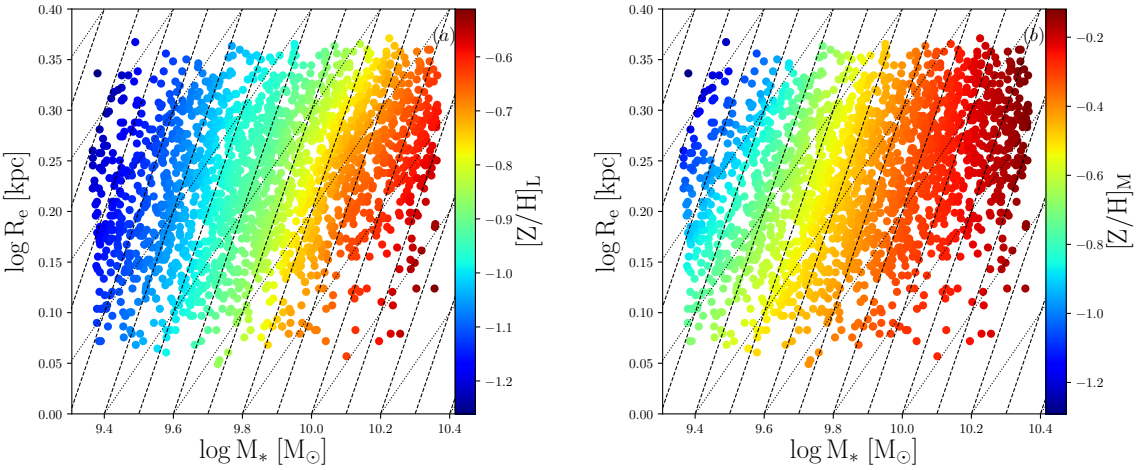

Figure 3.8 Mass–size plane for our sample of star-forming galaxies, with the colourscale representing LOESS-smoothed luminosity-weighted metallicity ($[Z/H]_L$; panel a) and mass-weighted metallicity ($[Z/H]_M$; panel b). The dashed lines are lines of constant $\Phi \propto M_*/R_e$, and the dotted lines are lines of constant $\Sigma \propto M_*/R_e^2$. Both $[Z/H]_M$ and $[Z/H]_L$ follows lines of constant Φ.

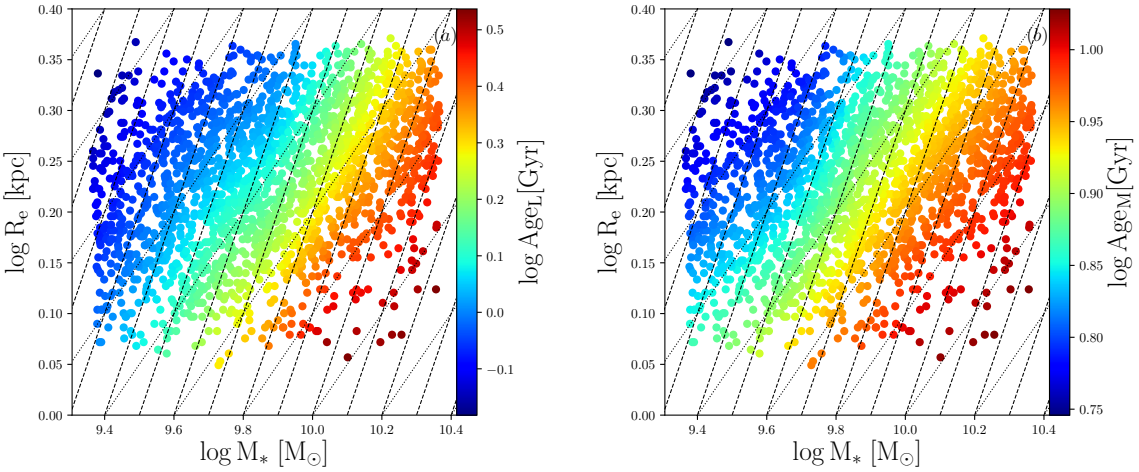

Figure 3.9 Mass–size plane for our sample of star-forming galaxies, with the colourscale representing LOESS-smoothed luminosity-weighted age (age_L; panel a) and mass-weighted age (age_M; panel b). The dashed lines are lines of constant $\Phi \propto M_*/R_e$ and the dotted lines are lines of constant $\Sigma \propto M_*/R_e^2$. While age_L follows lines of constant Σ, age_M instead varies somewhere between lines of constant Φ and Σ.

galaxies (blue points). In addition to not being 1-1, there is a large variation in $[Z/H]_M$ at fixed $[Z/H]_L$ for the star-forming galaxies.

Despite the non-linearity between $[Z/H]_M$ and $[Z/H]_L$, we see in Figure 3.8 that for star-forming galaxies, $[Z/H]_M$ (panel b), like $[Z/H]_L$ (panel a), follows lines of constant Φ. Li et al. (2018) also show that $[Z/H]_L$ for spiral galaxies in MaNGA varies along lines of constant Φ, and Scott et al. (2017) show that for all morphological types $[Z/H]_{SSP}$ varies along lines of constant Φ. This strengthens our quantitative results that global stellar metallicity is strongly dependent on the gravitational potential of the galaxy.

3.5.2. Age

It is well established that luminosity-weighted ages (age_L) strongly trace the younger stars (Trager et al. 2000a; Serra & Trager 2007; Trager & Somerville 2009), and indeed we see in Figure 3.7 panel (b) that for both the early-types and star-forming galaxies, age_M is consistently older than age_L. The early-types (red) resemble the relation shown in Figure 4 of McDermid et al. (2015), but for the star-forming galaxies (blue) there is a large spread in the age_M at fixed age_L. Notably, even at the youngest age_L, there are galaxies reaching the upper limit of the templates for age_M. For the youngest luminosity-weighted galaxies, it is possible that for these galaxies the spectrum is so dominated by young stars the contribution from low-luminosity old stars is poorly constrained, resulting in over-fitting of the oldest templates. This then leads to the large spread of age_M at fixed age_L.

Figure 3.9 shows that age_M (panel b) appears to follow lines of constant Σ, although not as closely as age_L. Age_M appears to vary more steeply than age_L, at a rate somewhere between lines of constant Φ and Σ, although for small, low-mass galaxies (below a stellar mass of $\approx 10^{9.7} M_\odot$ and radius $\approx 10^{0.2}$ kpc) age_M appears to closely follow Σ. Scott et al. (2017) show age_{SSP} also varies approximately along lines of constant Σ. While Li et al. (2018) do not plot lines of constant Σ, from their Figure 4 it is clear age_L varies more shallowly than the lines of constant Φ (lines of constant Σ are more shallow than lines of constant Φ).

3.6. Discussion

Our aim was to investigate which parameter (mass M_*, gravitational potential $\Phi \sim M_*/R_e$, or surface density $\Sigma \sim M_*/R_e^2$) best predicts the stellar population properties (age and metallicity) of star-forming galaxies. Looking both at the luminosity-weighted (section 3.4) and mass-weighted (section 3.5) parameters and taking into account both the tightness of the relations and any residual trends with galaxy size, we find age correlates best with surface density while metallicity [Z/H] correlates best with gravitational potential. These results are in striking agreement with Chapter 2, where, using different methods to determine stellar population parameters, we found early-type galaxies also show age correlating best with Σ and [Z/H] correlating best with Φ. We note that 'quiescent/star-forming' refers to a classification based on specific star formation rate whereas 'early-type/late-type' refers to a morphological classification, so 'early-type' and 'star-forming' are not mutually exclusive categories (see section 3.1 for further discussion of the overlap). However given the pronounced differences in internal structure, kinematics, and stellar population properties between the two categories, it is significant that they exhibit the same scaling relations. Crucially, this indicates that the dominant mechanism(s) driving stellar population evolution must originate while galaxies are still star-forming, and must be (at least) preserved through mergers and quenching processes. Here we discuss various mechanisms that could lead to these scaling relations.

3.6.1. Origin of the Metallicity–Potential Relation

We have demonstrated that global *stellar* metallicity exhibits a tight correlation with the gravitational potential for both early-type galaxies (Chapter 2) and star-forming galaxies

(this Chapter). D'Eugenio et al. (2018) found the same result for global *gas-phase* metallicity in star-forming galaxies. Furthermore, recent works hint at the existence of a similar global relation at higher redshift. Díaz-García et al. (2019) showed that at $z \sim 1$ more compact quiescent galaxies are both older and more metal-rich than their diffuse counterparts at fixed mass.

In general, in a closed-box model the total metal content is a reflection of the number of generations of stars the galaxy has formed; with each subsequent stellar generation more metals are produced and recycled into the next generation. However, we can rule out the [Z/H]–Φ relation being driven simply by the number of stellar generations, due to the existence of a strong correlation between the star formation duration (via either $[\alpha/\mathrm{Fe}]$ or the e-folding timescale) and gravitational potential in both early-types (M/R_e: Chapter 2; σ: Trager et al. 2000a; Thomas et al. 2005; Nelan et al. 2005; Thomas et al. 2010; Robaina et al. 2012; McDermid et al. 2015; Scott et al. 2017) and late-types (Ganda et al. 2007), since galaxies with a shallower potential (lower σ) have *longer*, rather than shorter, star formation durations.

The existence of the [Z/H]–Φ relation in both the gas and stars, in both young star-forming galaxies and old early-types, indicates the relation originates with in-situ star-formation, and is maintained throughout ex-situ assembly. Although the radius to which we probe ($\sim 1 R_\mathrm{e}$) is dominated by in-situ stars (Pillepich et al. 2014; Cook et al. 2016; Greene et al. 2019), we explore mechanisms related to both in- and ex-situ formation to explain the presence of the metallicity–potential relation. Regarding in-situ formation, either low-Φ galaxies *lose a higher fraction* of their metals or low-Φ galaxies *produce less* metals. In the following discussion we explore two possibilities, namely: (1) low-Φ galaxies are more likely to lose more metals, due to the relation between gravitational potential and gas escape velocity; or (2) low-Φ galaxies produce less metals due to variations in the initial-mass function. We then discuss how the relation could be preserved in galaxy mergers.

Metallicity is determined by gas escape velocity?

In Chapter 2 we proposed that the metallicity–potential relation is driven by low-Φ galaxies being more likely to lose their metals due to the relation between gravitational potential and gas escape velocity. The depth of the gravitational potential sets the escape velocity for ejection from the galaxy for metal-rich gas expelled by supernovae. This dependence of the gas escape-velocity on the gravitational potential also explains the existence of metallicity gradients within galaxies: the gravitational potential decreases outwards in galaxies, allowing stellar feedback to more easily eject metals in the outskirts than in the centre (Cook et al. 2016) and leading to decreasing radial stellar metallicity gradients, as observed in both late (Sánchez-Blázquez et al. 2014) and early-type galaxies (e.g Ferreras et al. 2019; Goddard et al. 2017; Martín-Navarro et al. 2018). This interpretation is supported by the results of Scott et al. (2009), who found a strong correlation in early-types between *local* [Z/H] and *local* escape velocity derived from dynamical models. Møller & Christensen (2020) also show that halo gas-phase metallicities are well explained by a dependence of the local gas-phase metallicity on the local gravitational potential. Supporting this explanation, simulations show that steep stellar population gradients are the result of in-situ star formation (Pipino et al. 2010), and mergers then tend to diminish these gradients (Kobayashi 2004; Di Matteo

et al. 2009), particularly at large radii where the stars have predominantly ex-situ origins (Hirschmann et al. 2015).

A test of this hypothesis is how the metallicity of the circumgalactic medium (CGM) correlates with galaxy structure; logically this mechanism should lead to a relative enrichment of the CGM around low-Φ galaxies at fixed M_*. Due to the low density nature of the CGM, obtaining precise metallicity measurements is time-consuming, and recent studies have sample sizes of less than 50 galaxies (e.g. Prochaska et al. 2017; Pointon et al. 2019). In addition, because the CGM is composed not only of stellar ejecta but also pristine gas from the halo and low-metallicity gas from satellites (e.g. Shen et al. 2013), any trend with galaxy gravitational potential would be difficult to interpret. An alternative way forward might be to investigate the dependence of CGM metallicity on galaxy structure in large-scale cosmological simulations of galaxy formation.

Metallicity is determined by initial mass function?

Another explanation for low-Φ galaxies producing fewer metals could be variations in the types of stars formed, i.e. the initial mass function (IMF). Different stellar types produce different chemical yields and, combined with their varying lifespans, affect both total metallicity [Z/H] and α-enhancement, with higher-mass stars leading to higher metallicities and α-enhancements (see e.g. Matteucci 2012). Indeed, Vincenzo et al. (2016) showed that the more top-heavy IMFs (Kroupa 2001; Chabrier 2003), with their greater proportion of high-mass stars, lead to twice the oxygen yields of the standard Salpeter (1955) IMF. Furthermore there is mounting evidence for a varying IMF both between (e.g. van Dokkum & Conroy 2010; Conroy & van Dokkum 2012b; Cappellari et al. 2012; Spiniello et al. 2014; Li et al. 2017) and within galaxies (Martín-Navarro et al. 2015a; van Dokkum et al. 2017; Vaughan et al. 2018; Parikh et al. 2018), although exactly what drives these variations remains unclear.

On the other hand, metallicity has been suggested to *anti*-correlate with the relative number of high-mass stars, both globally (Marks et al. 2012) with [Fe/H] and locally (Martín-Navarro et al. 2015b) with total metallicity [Z/H]. However in contrast, recent works have found that while both metallicity and IMF vary radially, spatially resolved maps show that IMF variations do not follow total metallicity [Z/H] variations (Martín-Navarro et al. 2019). Given these results, while the IMF clearly plays an important role in overall metal production, we find IMF variations do not explain the global metallicity–potential relation.

Ex-situ preservation

In addition to the previously discussed *generative* in-situ mechanisms, in order for the metallicity–potential relation to persist in ETGs it must be *preserved* during galaxy mergers. While simulations show that mergers tend to diminish metallicity gradients (Kobayashi 2004), it is possible that the global relation is preserved due to the compactness of a satellite influencing where it accretes onto the host. Using N-body simulations, both Boylan-Kolchin & Ma (2007) and Amorisco (2017) show that a compact, high-density satellite is more likely to accrete into the centre of the host, whereas a diffuse, low-density satellite is more easily disrupted by dynamical friction and therefore accretes onto the host's outskirts. This

differential process acts to reinforce the already established in-situ metallicity–potential relation: compact, high-Φ satellites will have relatively high metallicity and deposit their high-metallicity material into the centre of the host, increasing the host's gravitational potential. Conversely, diffuse, low-Φ satellites will deposit low-metallicity material at large radii, decreasing the host's gravitational potential at fixed mass. Additionally, Scott et al. (2013) find that, despite their different merger histories, both fast and slow rotating early-type galaxies lie on the same scaling relation between the Mgb spectral index and local escape velocity $V_{\rm esc}$. They show that simple model parameterisations indicate dry major mergers should move galaxies off, not along, the relation, and so the intrinsic scatter in the relation therefore provide an upper estimate on the frequency of dry major mergers. Combining predictions from N-body binary mergers and the observed scatter about the Mgb–$V_{\rm esc}$ relation, they estimate a typical present-day early-type galaxy to have typically only undergone about 1.5 dry major mergers.

Future studies comparing the slope of the metallicity–potential relation over all galaxy types, at low and high redshift, could further reveal the relative importance of these in- and ex-situ mechanisms, and the precise extent to which mergers diminish or preserve the relation.

3.6.2. Origin of the Age–Σ Relation

We find stellar age correlates best with surface mass density Σ for both star-forming and early-type galaxies (Chapter 2). While the true average stellar population age depends on when the galaxy first formed, the rate of star formation, and when the galaxy quenched, in practice single-burst model ages strongly depend on the age of the youngest stars (Trager et al. 2000a; Serra & Trager 2007; Trager & Somerville 2009). In Chapter 2 we proposed two possible explanations for the age–Σ relation in ETGs: (1) as a fossil record of the $\Sigma_{\rm SFR} \propto \Sigma_{\rm gas}$ relation while forming stars, or (2) as a result of compactness-driven quenching mechanisms.

For ETGs these two scenarios are completely degenerate, but in this work, because we use star-forming galaxies, we are able to break this degeneracy. In fact, given the result of this Chapter that the age–Σ relation also exists in SFGs, it would be an odd coincidence if the same relation was due to completely different physical processes. Assuming therefore the mechanism(s) leading to this relation is (are) the same for ETGs and SFGs, the relation must originate *before* quenching. Nonetheless, certain quenching mechanisms may further emphasize the relation. Here we discuss mechanisms related to each of these phases that could lead to or reinforce the age–Σ relation. Firstly we explore whether galaxies that formed earlier have high-Σ due to higher gas densities in the early universe, building upon the hypothesis from Chapter 2 that the relation is a fossil record of the $\Sigma_{\rm SFR} \propto \Sigma_{\rm gas}$ relation. We then discuss the possibility that compact galaxies quench earlier.

Compact galaxies formed earlier?

The age–Σ relation could be a result of more compact galaxies having formed earlier, because higher gas fractions in the early universe mean galaxies formed more compactly during their in-situ formation phase (Wellons et al. 2015). While this mechanism would apply to

both SFGs and ETGs, we first consider the body of evidence related to ETGs, then consider how this also affects SFGs.

The current paradigm from both observations and simulations is that present-day ETGs underwent two main phases of evolution: an early period of intense in-situ star formation at z ~2, producing the very compact galaxies observed at high redshift (e.g. van Dokkum et al. 2008; van der Wel et al. 2008), followed by passive ex-situ build-up via frequent minor and occasional major mergers (e.g. Oser et al. 2010; Barro et al. 2013; Rodriguez-Gomez et al. 2016; Wellons et al. 2016). During the in-situ phase the high gas density leads to a high star formation rate density, a causation parameterized by the Kennicut-Schmidt relation (Schmidt 1959; Kennicutt 1998; see Kennicutt & Evans 2012 for a review). As previously discussed in Chapter 2, the Kennicut-Schmidt relation, $\Sigma_{\rm SFR} \propto \Sigma_{\rm gas}$, in SFGs naturally leads to an age–Σ_* relation. A high gas density causes a high star formation rate (SFR) density and, assuming a non-replenishing gas supply, quickly exhausts the available gas, leading to a short star-formation duration and an old stellar population. Over time, the original high gas density is converted into a high stellar mass density. In addition, Tacconi et al. (2013) show that the Kennicutt-Schmidt relation is near-linear from redshifts $z \sim 1-3$, indicating this affects both old and young galaxies. Indeed, Franx et al. (2008) showed that specific star formation rate tightly anti-correlates with surface mass density (tighter than mass alone), concluding that star formation history is strongly dependent on surface mass density. Chapter 2 also showed that $[\alpha/\mathrm{Fe}]$, a proxy for star formation duration, correlates tightly with Σ (and Φ). Although still star forming, this fossil record of $\Sigma_{\rm SFR} \propto \Sigma_{\rm gas}$ is already detectable in our sample of SFGs as the age–Σ relation. Given the mass range of our sample of SFGs, $10^{9.4} < M_*/M_\odot < 10^{10.4}$, enough of the galaxies' star-forming period has passed for the relation with stellar age to be detectable. While the luminosity-weighted ages of SFGs are young, as discussed in section 5.2, luminosity-weighted ages predominantly trace the youngest stars, and the stellar population overall is likely much older as indicated by the mass-weighted ages, which are significantly older.

Additionally, at low redshift, SFGs are larger than quiescent galaxies at fixed mass (Shen et al. 2003; Trujillo et al. 2007; Cimatti et al. 2008; Kriek et al. 2009; Williams et al. 2010; Wuyts et al. 2011; van der Wel et al. 2014; Whitaker et al. 2017), indicating that currently star-forming galaxies are different from the progenitors of present-day compact quiescent galaxies, and will evolve into extended quiescent galaxies (Barro et al. 2013). This explains both why old SFG are more compact than young SFG, and also why early-types are more compact than SFGs. In this scenario, the age–Σ relation is a reflection of the gas density of the universe when the galaxy formed. We note, however, that any mechanism that causes a high gas density would also produce an age–Σ relation.

Compact galaxies quench earlier?

In Chapter 2 we proposed that the age–Σ relation in ETGs might be a result of compactness-driven quenching mechanisms. However, given the result of this work that age correlates tightly with Σ also for star-forming galaxies, we assume the mechanism(s) leading to the age–Σ relation is (are) the same for both quiescent and star-forming galaxies. Therefore, we infer the relation arises *before* quenching, thus disfavouring models where the relation is purely due to quenching. Nonetheless, quenching processes may act to reinforce an

already-existing relation[1]. Further work quantitatively comparing the age–Σ relation in low redshift samples of quiescent and SFGs may help resolve whether the relations originate from the same mechanism(s).

Star formation history and quiescence, as quantified in a variety of ways, correlate strongly with compactness and the presence of a central bulge, both at low (Kauffmann et al. 2003b, 2004; Bell 2008; Franx et al. 2008; van Dokkum et al. 2011; Bluck et al. 2014; Omand et al. 2014; Woo et al. 2017) and high redshifts (e.g. Bell et al. 2012; Wuyts et al. 2011; Cheung et al. 2012; Szomoru et al. 2012; Lang et al. 2014). Woo et al. (2015) proposed two main quenching pathways which may act concurrently: rapid central compactness-related processes, and prolonged halo (environmental) quenching. Compactness-related quenching mechanisms include processes which both build the central bulge and (either directly or indirectly) contribute to quenching, such as mergers and gaseous inflows from the disk. Specifically, gaseous inflows from the disk to the bulge, triggered by disk instability or an event such as a merger, are exhausted in a starburst, leading to increased bulge compactness. Additionally, these inflows can trigger active galactic nuclei which, if aligned with the gas disk, can cause molecular outflows, depleting surrounding gas on timescales of a few Myr and preventing further star formation (García-Burillo et al. 2014; Sakamoto et al. 2014). More recently, Woo & Ellison (2019) showed that, in addition to these compactness-related mechanisms, processes unrelated to central density such as secular inside-out disk growth (Lilly & Carollo 2016) combined with slow environmental quenching also naturally lead to a relation between the compactness of the galaxy (which they define by the surface mass density within the central 1kpc, $\Sigma_{1\mathrm{kpc}}$) and quiescence (defined by low sSFR). This compactness–quiescence relation would then naturally lead to a relation between surface mass density and stellar age in passive galaxies.

3.7. Summary

In this Chapter we have used 2- and 3- dimensional fits to study how the age and metallicity [Z/H] of the global stellar population in star-forming galaxies correlate with the galaxy structural parameters stellar mass (M_*), gravitational potential ($\Phi \sim M_*/R_\mathrm{e}$), and surface mass density ($\Sigma \sim M_*/R_\mathrm{e}^2$). This new study builds on our results for early-type galaxies (Chapter 2). For both early-type and star-forming galaxies, we find the tightest correlations and least residual trend with galaxy size for the age–Σ and [Z/H]–Φ relations. Finding these trends in both these studies, despite the different samples, methods, and models used to derive not only the stellar population parameters but also the stellar masses and effective radii, suggests our results are robust. We discuss multiple mechanisms that might produce these relations. We suggest that the [Z/H]–Φ relation is driven by low-Φ galaxies losing more of their metals because the escape velocity required by metal-rich gas to be expelled by supernova feedback is directly proportional to the depth of the gravitational potential. This relation is preserved during mergers, as elucidated by simulations. We rule out the possibility of the [Z/H]–Φ relation being due to IMF variations. In Chapter 2

[1]In principle, quenching could still be responsible for the observed trend if most SFGs had undergone a quenching phase, followed by rejuvenation. In practice, however, rejuvenation is not common and most SFGs have extended star-formation histories (e.g. Thomas et al. 2010; Chauke et al. 2019)

we discussed compactness-related quenching mechanisms which could lead to the age–Σ relation, however given in this work we show that the relation exists also in star-forming galaxies, it must arise *before* quenching. We therefore explore the possibility that the age–Σ relation is a result of compact galaxies forming earlier. Additionally, certain compactness-related quenching mechanisms may act to reinforce the already-existing relation. Future studies using cosmological simulations may help resolve the relative importance of each of these mechanisms.

CHAPTER 4

Age and Metallicity Relations over 6 Gyr

The work presented in this chapter has been previously published as 'The LEGA-C and SAMI Galaxy Surveys: Quiescent Stellar Populations and the Mass–Size Plane across 6 Gyr', Barone, Tania M.; D'Eugenio, Francesco; Scott, Nicholas, Colless, Matthew; et al., 2022, MNRAS, 512, 3828B

4.1. Introduction

In this Chapter we build on the results of stellar populations scaling relations at low redshift by analysing if (and how) the relations change across a lookback time of 6 Gyr ($0.014 \leq z \leq 0.76$), to test the hypotheses proposed for the age–Σ and [Z/H]–*Phi* scaling relations. Specifically, we study how the spatially-integrated average (global) age and metallicity of individual quiescent galaxies vary in the mass–size plane. Furthermore, we look at how the age–Σ and [Z/H]–Φ relations found at low redshift appear at $0.60 \leq z \leq 0.76$. By quantifying the significance of these scaling relations at low and intermediate redshift we aim to understand their origins and, in the process, begin to discern the redshift dependence of stellar population evolution over the past 6 Gyr.

The Chapter is arranged as follows. In Section 4.2 we describe the $0.60 \leq z \leq 0.68$ and $0.68 < z \leq 0.76$ samples from the LEGA-C survey and the $0.014 \leq z \leq 0.10$ comparison sample from the SAMI survey. Section 4.3 describes the full spectral fitting method used to obtain the metallicity and age measurements, as well as our analysis methods. We present the [Z/H] and age results in Section 4.4, followed by a discussion in Section 4.5. In discussing the age results we link the age–Σ relation to the distribution of the quiescent and star-forming populations across redshift in the mass–size plane in Section 4.5.2. Lastly we provide a summary of our conclusions in Section 4.6. We assume a flat Λ cold dark matter (ΛCDM) Universe with $\Omega_\Lambda = 0.7$, $\Omega_M = 0.3$ and $H_0 = 70\,\mathrm{km\,s^{-1}\,Mpc^{-1}}$, and a Chabrier (2003) initial mass function.

4.2. Data

We describe the LEGA-C and SAMI surveys in Sections 4.2.1 and 4.2.2 respectively, followed by describing auxiliary parameter measurements in Section 4.2.3. The adopted quiescent versus star-forming galaxy selection criterion is detailed in Section 4.2.4.

4.2.1. The LEGA-C Survey

The Large Early Galaxy Astrophysics Census (LEGA-C; van der Wel et al. 2016) is a slit spectroscopic survey of galaxies at intermediate redshifts in the COSMOS field (Scoville et al. 2007), using the VIsible Multi-Object Spectrograph (VIMOS; Le Fèvre et al. 2003) on the Very Large Telescope. LEGA-C targets were selected from the UltraVISTA catalogue (Muzzin et al. 2013a) based on a redshift-dependent apparent K_S magnitude limit: $K_s < 20.7 - 7.5\log((1+z)/1.8)$ (van der Wel et al. 2016), which has the advantage of closely resembling a selection on stellar mass while remaining model independent (see Appendix A of van der Wel et al. 2021). The survey comprises 4209 galaxies, 3472 of which have spectroscopic redshift measurements within $0.60 \leq z \leq 1.0$. Targets were observed for ~20 hours to reach an approximate S/N per Å ≈ 20 in the continuum. We use integrated spectra summed along the entire slit, with an effective spectral resolution of R~3500 (Straatman et al. 2018) and observed wavelength range ~6300Å–8800Å. We use spectra from the third

data release (van der Wel et al. 2021)[1]; see van der Wel et al. (2016) and Straatman et al. (2018) for earlier data releases.

While the LEGA-C sample spans the redshift range $0.60 \leq z \leq 1.0$, above $z \sim 0.8$ the survey selection criteria and the S/N requirement for stellar population analyses (median S/N per Å ≥ 10 in the rest-wavelength region 4427–4548 Å; see Section 4.2.5) limit the sample to only the brightest (most massive) targets. We therefore restrict our analysis to the redshift range $0.60 \leq z \leq 0.76$. We then estimate the size evolution with redshift for this redshift range using the relations from van der Wel et al. (2014) and Mowla et al. (2019) for high ($\log M_*/M_\odot > 11.3$) and intermediate $\log M_*/M_\odot \sim 10.75$) mass galaxies respectively. To ensure the size evolution is less than 0.05 dex (the uncertainty on the size measurements), we split the sample into two redshift bins: $0.60 \leq z \leq 0.68$ and $0.68 < z \leq 0.76$. Lastly, given the LEGA-C sample at z$\sim$ 0.7 is representative down to a stellar mass limit of $\log M_* \geq 10.48$ (van der Wel et al. 2021), we restrict our analysis to LEGA-C galaxies with $10.48 \leq \log M_* \leq 11.5$. This leaves final samples of 412 galaxy (219 quiescent, 193 star-forming) for $0.60 \leq z \leq 0.68$, and 513 (273 quiescent, 240 star-forming) for $0.68 < z \leq 0.76$.

4.2.2. The SAMI Galaxy Survey

The Sydney-AAO Multi-object Integral-field (SAMI; Bryant et al. 2015; Croom et al. 2021b) Galaxy Survey is a low-redshift integral-field survey of 3068 unique galaxies observed using the SAMI instrument (Croom et al. 2012) connected to the AAOmega spectrograph (Sharp et al. 2006, 2015) on the Anglo-Australian Telescope. The sample spans the redshift range $0.004 \leq z \leq 0.11$. Galaxies were observed through fused-fibre hexabundles (Bland-Hawthorn et al. 2011; Bryant et al. 2014), each comprising 61 tightly-packed fibres that form an approximately circular grid with a diameter of 15". Observations were typically for a total of 3.5 hours comprised of 7 dithers of 30 minutes each. Targets were selected based on stellar mass cuts in narrow redshift bins from three equatorial regions covered by the volume-limited Galaxy And Mass Assembly (GAMA; Driver et al. 2011) survey and 8 cluster regions; see Bryant et al. (2015) and Owers et al. (2017) for a full description of the sample selection for the GAMA and cluster regions respectively. For this analysis we exclude targets from the cluster regions to avoid over-representing galaxies from dense environments (e.g. as discussed in van de Sande et al. 2021), leaving the SAMI-GAMA sample which is highly complete ($\sim$ 90%) for $\log M_* \geq 10$ (Bryant et al. 2015; van de Sande et al. 2021; Croom et al. 2021b). SAMI spectra have two components, a 'blue' component (3700–5700 Å) at a resolution of R=1800, and a 'red' component (6300–7400 Å) at R=4300. For the full-spectral fits the higher spectral resolution red component is degraded to match the resolution of the blue component. The whole spectrum is then fit simultaneously. We use spatially-integrated $1R_e$ spectra from the third data release (Croom et al. 2021b)[2]; see Allen et al. (2015), Green et al. (2018) and Scott et al. (2018) for earlier releases.

As for the LEGA-C samples, we want to ensure the redshift evolution within our SAMI sample is less than the typical uncertainty on the size measurements (0.05 dex). We calculate the estimated size evolution within the SAMI redshift range using the same relations of van

[1]The data can be accessed from http://archive.eso.org/cms/eso-archive-news/Third-and-final-release-of-the-Large-Early-Galaxy-Census-LEGA-C-Spectroscopic-Public-Survey-published.html

[2]The data can be accessed at https://docs.datacentral.org.au/sami/

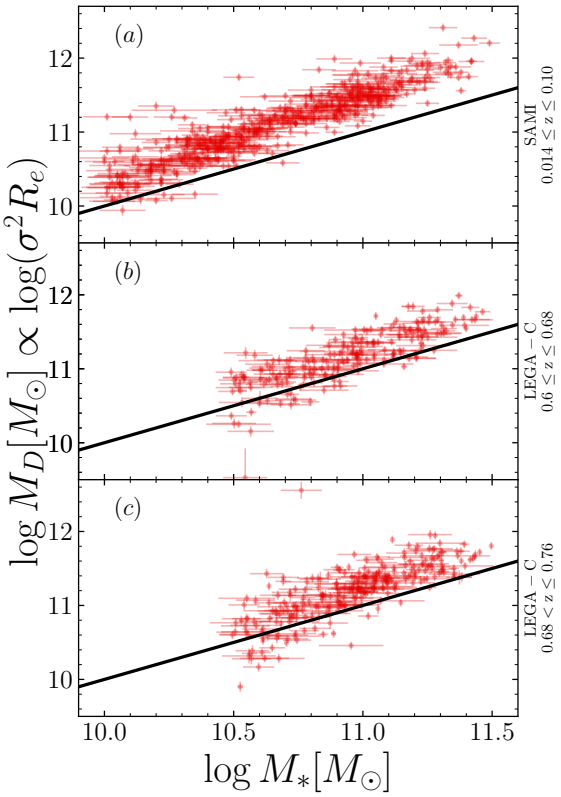

Figure 4.1 The stellar mass M_* versus the virial proxy for the dynamical mass M_D for the three redshift samples. The solid black line shows the 1-1 relation. Each point shows the 1σ uncertainty on $\log M_*$ and $\log M_D$. There is good agreement between the two mass estimates, with the dynamical masses being 0.4 and 0.2 dex higher for the SAMI and LEGA-C samples respectively.

der Wel et al. (2014) and Mowla et al. (2019) used in Section 4.2.1 for the LEGA-C sample. Based on the estimated size evolution, we remove 22 galaxies at the ends of the redshift range. Our final SAMI sample comprises of 974 galaxies (524 quiescent, 450 star-forming) with $10.0 \leq \log M_* \leq 11.5$, median S/N per Å ≥ 10 in the rest wavelength region 4427–4548, and in the redshift range $0.014 \leq z \leq 0.10$.

4.2.3. Measurements of galaxy properties

Semi-major effective radii (R_e) were measured from Sérsic fits using the GALFIT software (Peng et al. 2010) by van der Wel et al. (2021) for the LEGA-C sample and Hill et al. (2011) for the SAMI sample. For LEGA-C targets van der Wel et al. (2021) followed the procedure of van der Wel et al. (2012) on HST ACS F814W images from the COSMOS program (Scoville et al. 2007). For SAMI targets, Hill et al. (2011) followed the process of Kelvin et al. (2012), using *r*-band photometry from SDSS DR7 (Abazajian et al. 2009) reprocessed for GAMA. We note that colour gradients within galaxies affect the absolute measurement of R_e, in that bluer bands lead to larger size measurements (e.g. Kelvin et al. 2012). However, given our analysis focuses on the relative difference in size *within* each redshift bin, any systematic offset between the SAMI and LEGA-C size measurements due to the difference in photometric band does not affect our results.

We use stellar masses (M_*) and star formation rates (SFR) measured by de Graaff et al.

(2020, 2021) for the LEGA-C galaxies and Driver et al. (2018) for the SAMI galaxies. In both catalogues the measurements were derived using the MAGPHYS (Multi-wavelength Analysis of Galaxy Physical Properties; da Cunha et al. 2008) spectral energy distribution fitting software, based on the Bruzual & Charlot (2003) library of simple stellar population spectra, a Charlot & Fall (2000) dust attenuation model, a Chabrier (2003) initial mass function and an exponentially declining star formation history (however the LEGA-C star formation history also includes random star-formation bursts). While the two catalogues differ slightly in the photometric bands used for the fits due to differences in data availability, they both include photometry ranging from ultra-violet to the far-infrared. Specifically, de Graaff et al. (2021) used ugriz and BVYJHK$_s$ from UltraVISTA as well as Spitzer infrared and multiband (rest-frame mid ultra-violet to far-infrared), while Driver et al. (2018) used FUV, NUV, ugriz, ZYJHK, W1234, PACS100/160 and SPIRE 250/350/500 (rest-frame far ultra-violet to far-infrared). See de Graaff et al. (2021) and Driver et al. (2018) for further details. The samples are complete in stellar mass within each redshift bin ($\log M_* \geq 10, 10.48, 10.48 M_\odot$ for $z_{\rm SAMI} \in [0.014, 0.10]$, $z_{\rm LEGA-C} \in [0.60, 0.68], [0.68, 0.76]$ respectively). Our results are qualitatively unchanged if we use the same stellar mass limit ($\log M_* \geq 10.48$) for all three redshift bins.

We choose to use an independent measure of the stellar mass rather than those derived from the full spectral fits due to the increased wavelength coverage of the MAGPHYS masses. Given the rest spectral range of the LEGA-C (~3700–5200 Å for $z = 0.67$) and SAMI spectra (~3500–5400 and 6000–7000 Å for $z = 0.05$), masses derived from the full spectral fits include predominantly blue light, so they will be inevitably biased due to not sampling the rest-frame infrared. MAGPHYS stellar masses are based on a broader wavelength range (rest-frame ultra-violet to far infrared), which contains more information about dust extinction and reaches redder wavelengths than the spectroscopy alone.

In addition to covering the GAMA regions from which the SAMI sample was selected, the Driver et al. (2018) catalogue also includes measurements for the G10-COSMOS region (Davies et al. 2015; Andrews et al. 2017) which includes 301 LEGA-C galaxies. We use this overlap of 301 galaxies to check for systematic biases between the samples that might arise from the different photometric bands used in the SED fits. We find good agreement between the two catalogues for both the stellar masses and the star formation rates. The mean difference between the two catalogues is 0.08 ± 0.15 dex for $\log M_*$ and 0.07 ± 0.40 dex for $\log$ SFR, with the values from de Graaff et al. (2021) being slightly more massive and star-forming.

Lastly we define a simple proxy for the total (dynamical) galaxy mass M_D based on the virial theorem:

$$M_D \equiv k\sigma^2 R_e / G \tag{4.1}$$

Where σ is the aperture velocity dispersion (measured from the pPXF fits; see Section 4.3.1), G is the gravitational constant ($4.3 \times 10^{-6}\,\mathrm{km^2\,kpc\,s^{-2}}\,M_\odot^{-1}$), and k is a constant set to 5.0 (Cappellari et al. 2006). Figure 4.1 shows the stellar and dynamical mass estimates for the quiescent galaxies in the three redshift bins. In all three redshift samples there is good linear agreement between the stellar and dynamical estimates, with M_D being systematically 0.4 and 0.2 dex more massive than M_* for SAMI and LEGA-C galaxies respectively. We note that the higher $\log M_D - \log M_*$ for SAMI galaxies compared to LEGA-C is likely driven

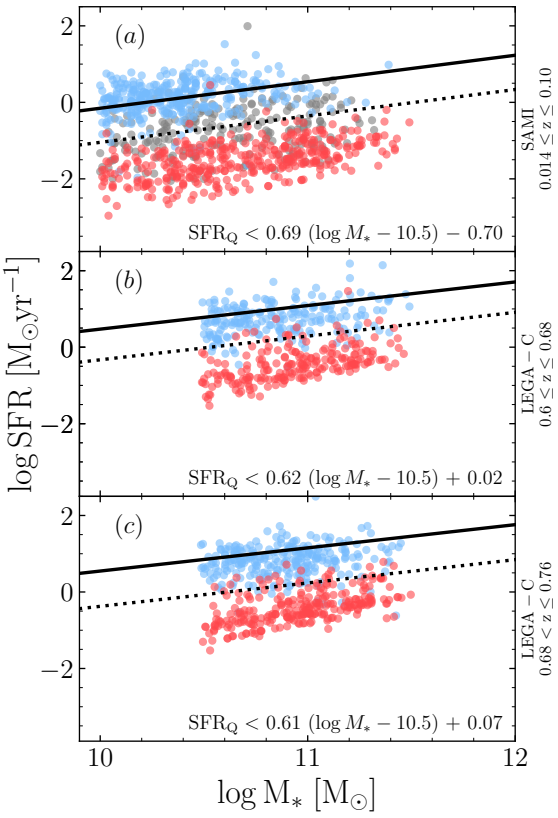

Figure 4.2 Star formation rate versus stellar mass for the three redshift bins. The black solid lines are the redshift-dependent main sequence from Whitaker et al. (2012, see Equation 4.2). The dotted black lines are the adopted boundary between quiescent and star-forming galaxies, defined as $SFR_Q < SFR_{MS} - 2RMS$ (bottom right of each panel), where RMS is the measured scatter about the main sequence based on an initial cut 1 dex below the relation. The points are coloured using quiescent (red points), star-forming (blue points), and intermediate (grey points; panel a only) selection criteria from the literature (see Section 4.2.4); our adopted selection criteria are comparable to these alternatives.

by the smaller physical coverage of the SAMI galaxies ($1R_e$) compared to LEGA-C ($\gtrapprox 1R_e$; see Section 4.2.5). However, given our analysis focuses on trends within redshift bins, systematic differences between bins does not influence our results. For a detailed discussion and analysis of dynamical versus stellar masses for LEGA-C galaxies, we refer the reader to de Graaff et al. (2021).

4.2.4. Quiescent Galaxy Selection

We separate quiescent and star-forming galaxies in both the LEGA-C and SAMI samples based on their distance from the redshift-dependent star-forming main sequence defined by Whitaker et al. (2012):

$$\log \mathrm{SFR} = (0.70 - 0.13z)(\log M_* - 10.5) + 0.38 + 1.14z - 0.19z^2 \tag{4.2}$$

We show this relation in Figure 4.2 (solid black line) using the central redshift value in each bin ($z = 0.057, 0.64, 0.72$). We do an initial cut 1 dex below the relation and measure the root-mean-square (RMS) scatter about the trend. We then define quiescent galaxies as those with $SFR_Q < SFR_{MS} - 2RMS$ (dotted black line). The precise selection cut for each redshift bin is given in the corresponding panel of Figure 4.2.

Post-starburst galaxies are a subclass of quiescent galaxies that recently quenched after a burst of star-formation (Dressler & Gunn 1983; Balogh et al. 1999; Dressler et al. 1999), and therefore contain a young average stellar population. As a result of their rapid quenching (Wu et al. 2020), post-starburst galaxies tend to be smaller than the rest of the quiescent population at fixed mass (Whitaker et al. 2012; Yano et al. 2016; Almaini et al. 2017). The young average ages and small sizes of post-starburst galaxies are contrary to the rest of the quiescent population in which young galaxies tend to be larger at fixed mass (Wu et al. 2018). The number of post-starburst galaxies in our three redshift samples (defined as quiescent galaxies with an equivalent width of $H\delta_A > 4$Å; e.g. Wu et al. 2018; D'Eugenio et al. 2020) is 2, 8, and 19 (0.4%, 4%, and 7%) for $0.014 \leq z_{\rm SAMI} \leq 0.10$, $0.60 \leq z_{\rm LEGA-C} \leq 0.68$ and $0.68 < z_{\rm LEGA-C} \leq 0.76$ respectively. It can be argued that post-starburst galaxies should be removed from our sample, because their evolutionary path with a final starburst in the centre is different from the rest of the galaxy population (Wu et al. 2018, 2020; D'Eugenio et al. 2020). However, when we repeat our analysis after having removed these galaxies, we find the results qualitatively unchanged. Therefore we do not remove post-starburst galaxies from our quiescent samples.

Comparison to other Quiescent classifications

We use the star-forming main sequence as defined by Whitaker et al. (2012) because their analysis used the same cosmological parameters and IMF assumed in this work and covers the full redshift range of both the LEGA-C and SAMI samples. We note however that the Whitaker et al. (2012) results are based on linear fits in the $\log \mathrm{SFR}$–$\log M_*$ plane, but more recent works have shown that the star-forming main sequence turns over at high stellar masses (e.g. Leslie et al. 2020). We therefore test our analysis using other quiescent selection criteria used in the literature for the two surveys.

In Figure 4.2 we compare our quiescent selection criterion to others used in the literature for the two surveys. The SAMI galaxies (panel a) are coloured by the selection used in Croom et al. (2021a), which is based on the star formation rates from Medling et al. (2018) and distance from the Renzini & Peng (2015) main sequence. The LEGA-C galaxies (panels b and c) are coloured by their U–V vs V–J diagram classification (Labbé et al. 2005), as defined by Muzzin et al. (2013b) and used in, e.g., Chauke et al. (2018), Wu et al. (2018) and Straatman et al. (2018). Figure 4.2 shows that our quiescent selection based on distance from the Whitaker et al. (2012) main sequence is comparable to these alternative selection criteria used in the literature. We repeated our anlysis using these alternate quiescent selection criteria and find our results unchanged. Therefore, we use the quiescent criteria based on the Whitaker et al. (2012) main sequence and MAGPHYS derived SFR and M_* for consistency across the two surveys.

4.2.5. Survey Comparison

Galaxies have well established internal radial stellar population gradients that, when combined with a varying aperture size, can lead to spurious global trends. A key difference between the two surveys are the apertures used; the VIMOS instrument used by LEGA-C has slits 1" wide and 8" long whereas the SAMI instrument uses fused-fibre hexabundles

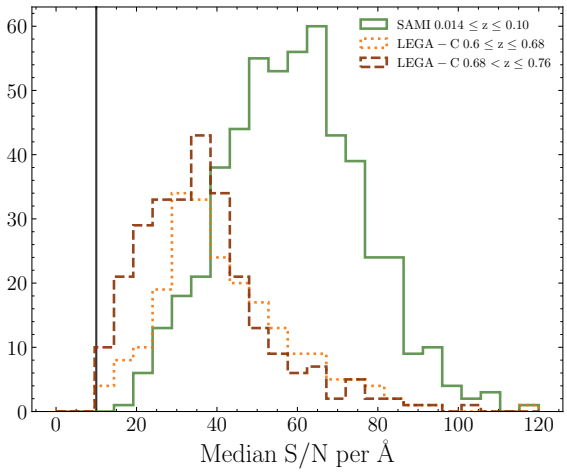

Figure 4.3 Median spectral S/N per Å in the rest-wavelength region 4427–4548 Å for SAMI (solid green) and LEGA-C ($z \in [0.60, 0.68]$ dotted orange, $z \in [0.68, 0.76]$ dashed brown) quiescent galaxies. The solid black line represents the S/N threshold (S/N≥ 10) of all three redshift samples. The median S/N for the three samples is $S/N_{SAMI} = 59$, and $S/N_{LEGA-C} = 39$ and 35 for $z \in [0.60, 0.68]$ and $z \in [0.68, 0.76]$ respectively.

of 15" diameter, comprised of 61 individual fibres each 1.6" in diameter. For the SAMI targets we use spectra integrated within 1 effective radius (R_e), and for the LEGA-C data we use spectra integrated along the entire slit. At $z = 0.7$ 1" corresponds to a physical scale of ~7.1 kpc which encompasses at least 50% of the total flux, but depending on the galaxy's apparent size the spectrum will also contain flux from outer regions ($R > R_e$). Therefore, despite the different apertures used in the two surveys, all galaxies are probed to at least $1R_e$, mitigating potential aperture bias in measurements between the two surveys. We emphasise, however, that we are not directly comparing stellar population parameters between the redshift bins, rather we are interested in how properties vary *within* redshift bins. Therefore, any systematic bias in stellar population measurements arising from the differences between the two instruments do not influence our analysis.

In Figure 4.3 we compare the spectral data quality of the quiescent samples between the two surveys by comparing the median spectral S/N per Å in the rest-wavelength range covered by all targets (4427–4548 Å). The median S/N for the three samples are $S/N_{SAMI} = 59$, and $S/N_{LEGA-C} = 39$ and 35 for $z \in [0.60, 0.68]$ and $z \in [0.68, 0.76]$ respectively. The black dotted line shows our adopted quality threshold at S/N ≥ 10. This minimum S/N requirement only affects 5 quiescent galaxies in the highest redshift LEGA-C bin which span in stellar mass from $\log M_* = 10.6$ to $11.3 M_\odot$. We therefore consider the effect of this quality cut on the overall mass-completeness of the sample to be negligible.

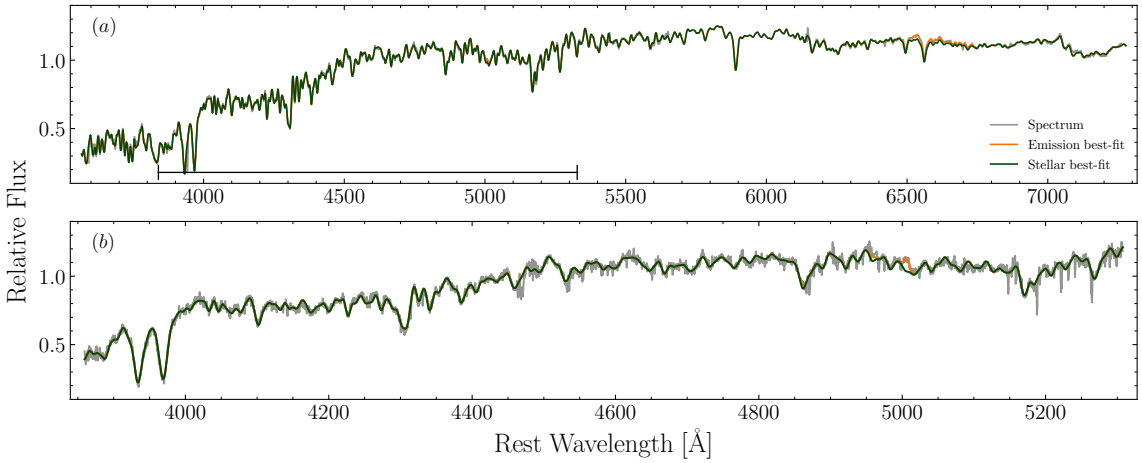

Figure 4.4 Example full spectral fits for SAMI galaxy ID=278109 (panel a) and LEGA-C galaxy ID=206573, mask ID=1 (panel b). In both panels the original spectrum is shown in grey, with the best-fit from the stellar templates in green and the best-fit emission templates in orange. By simultaneously fitting the stellar and gas components, we are able to recover absorption features masked by emission lines. The black horizontal line in panel a shows the wavelength range of panel b for ease of comparison. The fluxes are normalised such that the median flux across the spectrum is 1.

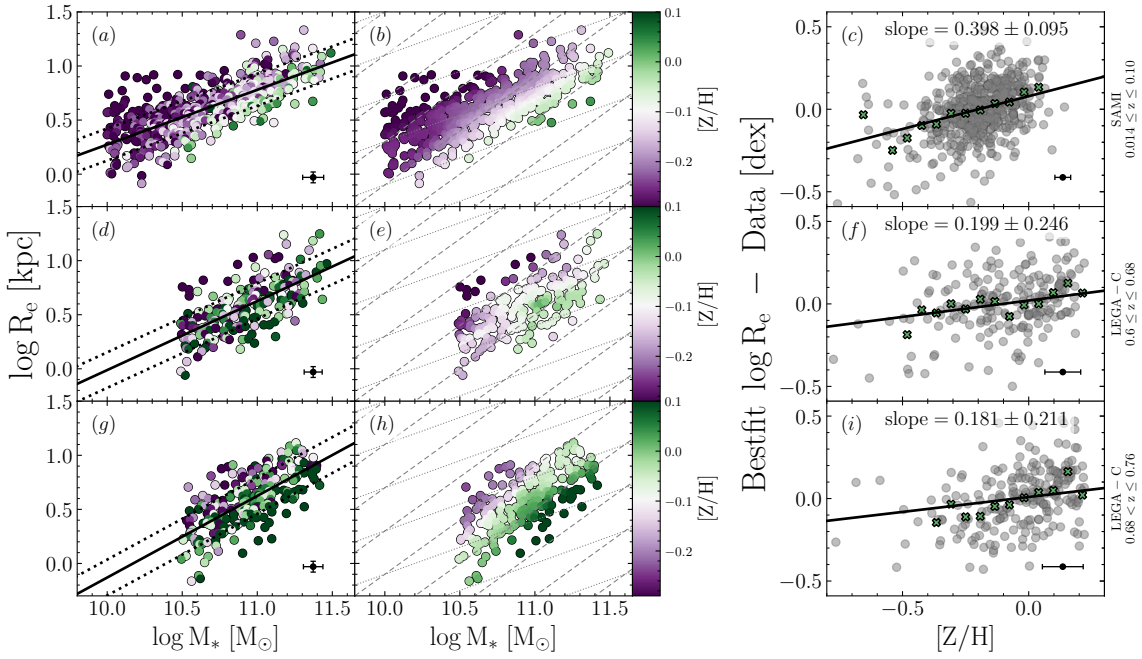

Figure 4.5 Stellar metallicity [Z/H] of quiescent galaxies in the stellar mass–size plane for three redshift bins. The top row shows the SAMI galaxies $0.014 \leq z \leq 0.10$, middle row the LEGA-C galaxies with $0.60 \leq z \leq 0.68$, and the bottom row the LEGA-C galaxies with $0.68 < z \leq 0.76$. The colour scale of the left column represents metallicity and the centre column shows the smoothed metallicity using the LOESS algorithm. The best-fits are shown in the left column (black solid line) with the fitted 1σ intrinsic scatter (black dotted lines). The median uncertainty on the mass, size and [Z/H] are shown by the example point in the bottom right corners of the left and right columns. In the centre column, the dashed lines show constant M_*/R_e and the dotted lines show constant surface density $\Sigma \propto M_*/R_e^2$. The right column shows the dependence of the residuals (defined as the perpendicular distance between the model minus the data) from the best-fit mass–size relation with metallicity. The black line in the right column is the best-fit relation to the residuals, with the slope written at the top of each panel. The crosses show the median value in independent bins with 3 or more galaxies. This Figure suggests that metallicity varies with M_*/R_e (dashed lines in the middle column) in all three redshift bins.

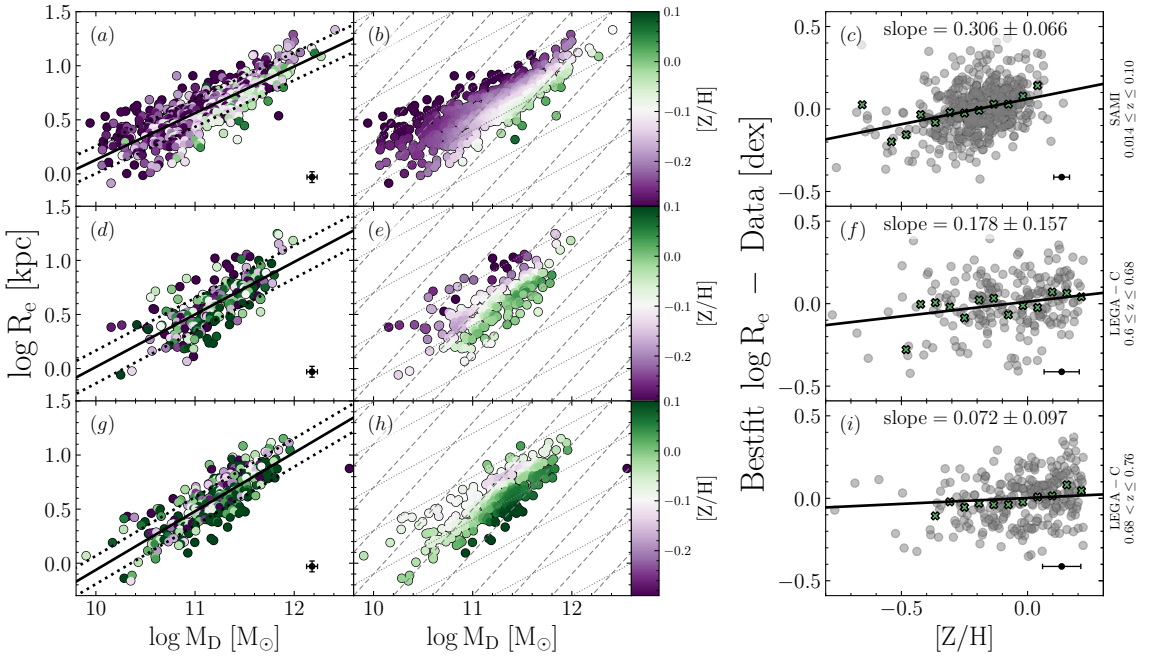

Figure 4.6 Stellar metallicity [Z/H] of quiescent galaxies in the dynamical mass–size plane for three redshift bins. The top row shows the SAMI galaxies $0.014 \leq z \leq 0.10$, middle row the LEGA-C galaxies with $0.60 \leq z \leq 0.68$, and the bottom row the LEGA-C galaxies with $0.68 < z \leq 0.76$. The colour scale of the left column represents metallicity and the centre column shows the smoothed metallicity using the LOESS algorithm. The best-fits are shown in the left column (black solid line) with the fitted 1σ intrinsic scatter (black dotted lines). The median uncertainty on the mass, size and [Z/H] are shown by the example point in the bottom right corner of the left and right columns. In the centre column, the dashed lines show constant M_D/R_e and the dotted lines show constant surface density $\Sigma \propto M_D/R_e^2$. The right column shows the dependence of the residuals (defined as the perpendicular distance between the model minus the data) from the best-fit mass–size relation with metallicity. The black line in the right column is the best-fit relation to the residuals, with the slope written at the top of each panel. The crosses show the median value in independent bins with 3 or more galaxies. This Figure suggests that metallicity varies with M_D/R_e (dashed lines in the middle column) in all three redshift bins.

4.3. Methodology

4.3.1. Stellar Population Measurements

Luminosity-weighted stellar population parameters for both the LEGA-C and SAMI galaxies are measured from full spectral fits using 350 theoretical templates based on the Extended Medium resolution INT Library of Empirical Spectra (E-MILES; Sánchez-Blázquez et al. 2006b; Vazdekis et al. 2016), isochrones from Girardi et al. (2000) and a Chabrier (2003) initial mass function. We use the full set of 350 templates which contain 50 age values ranging from 0.063 to 17.78 Gyr, 7 [Z/H] values ranging from −2.32 to +0.22, and have [α/Fe] values scaled to the solar neighbourhood (the "base" models; Vazdekis et al. 2016). The normalisation for the luminosity-weighting is calculated in the range from 3000–8000Å. We tested our analysis using the BaSTI isochrones (Pietrinferni et al. 2004, 2006) and found our results qualitatively unchanged. We fit the templates to the de-redshifted spectra using the Python implementation of the publicly available Penalized Pixel-Fitting software (pPXF; Cappellari & Emsellem 2004; Cappellari 2017). We do an initial fit to ensure that we have a good estimate of the S/N ratio per pixel and multiply the noise by a rescaling coefficient so

that the reduced χ^2 is unity. The median rescaling is 1.45 for the LEGA-C sample and 0.54 for the SAMI sample, with standard deviations of 0.31 and 0.21 respectively. We then use this improved estimate of the noise for the second (final) fit. The improved noise estimate is also used to measure the S/N per Å in the rest wavelength range 4427–4548 Å. This wavelength range was chosen because it is covered by all galaxies in the two samples. To account for dust reddening and any offsets to the continuum shape due to flux calibration, this final fit includes a 10^{th} degree multiplicative polynomial.

The final age and metallicity values are the weighted average of all the templates:

$$\log \text{Age} = \frac{\Sigma w_i \log \text{Age}_i}{\Sigma w_i} \tag{4.3}$$

$$[\text{Z/H}] = \frac{\Sigma w_i [\text{Z/H}]_i}{\Sigma w_i} \tag{4.4}$$

where w_i is the weight measured from pPXF for the i^{th} template, with single-burst age and metallicity values and $[\text{Z/H}]_i$ and age_i. Following McDermid et al. (2015) and González Delgado et al. (2015), the weighted average age is measured using the logarithm of the template ages because the template ages are sampled logarithmically.

All fits are done without linear regularisation, which imposes constraints on the weights of neighbouring templates (in age-metallicty space) to vary smoothly. While using linear regularisation produces more realistic star-formation histories, by construction reasonable degrees of regularisation do not significantly change the weighted average age and [Z/H] values (Chapter 3.3.2).

In addition to the stellar templates, we also include templates for common gas emission lines. We fix the flux ratios of the Balmer series from H_α to H_θ assuming a decrement based on Case B recombination (electron temperature $T = 10^4$ K and number density $n = 100\,\text{cm}^{-3}$; Dopita & Sutherland 2003), using the TIE_BALMER pPXF keyword. Any residual difference in flux from the fixed ratios is attributed to dust extinction, which is fit using a Calzetti et al. (2000) attenuation curve (via the GAS_REDDENING keyword). We also limit the ratios of the [OII] and [SII] doublets to lie within the theoretical ranges predicted by atomic physics (Osterbrock & Ferland 2006) using the LIMIT_DOUBLETS keyword. The [OIII], [OI] and [NII] doublets also have their flux ratios tied based on atomic physics. We show example fits in Figure 4.4 for SAMI galaxy ID=278109 and LEGA-C galaxy ID=206573 mask ID=1.

The fits are done using the full wavelength range available for each spectrum; the typical rest-wavelength range for the SAMI and LEGA-C spectra are ~3461–7077 Å and ~3723–5168 Å respectively. We tested the resulting age and metallicity values from fits to SAMI spectra that were restricted to use the rest wavelength range typical of the LEGA-C sample. While we found good agreement for both the age and metallicity values, the age values in the reduced wavelength range were on average 0.067 ± 0.064 dex younger than when fitted using the full SAMI wavelength range. This modest difference is expected given that the wavelength range 3723–5168 Å contains more and stronger stellar absorption features compared to the range 5168–7077 Å. Given we are interested in the age variations *within* each redshift bin, our results and interpretations are not affected by this minor discrepancy.

We check our stellar population measurements by comparing to other studies probing similar redshift ranges. We note that the absolute age of stellar population templates (and

Table 4.1 The Spearman correlation coefficient (ρ) and 1σ uncertainty for correlations between stellar population parameter ([Z/H] or Age) and structural parameter M, M/R_e and M/R_e^2 for both the stellar mass (M_*) and a dynamical mass estimate ($M_D \propto \sigma^2 R_e$). For each set of relations ([Z/H] or Age, M_* or M_D) we highlight in bold the structural parameter (M, M/R_e, M/R_e^2) with the highest Spearman correlation coefficient (if $\rho > 0.25$ and the difference to the next highest value is greater than $1\sigma_\rho$).

Parameter	Sample	M_*	M_*/R_e	M_*/R_e^2	M_D	M_D/R_e	M_D/R_e^2
[Z/H]	$0.014 \leq z_{SAMI} \leq 0.10$	0.55 ± 0.01	**0.66 ± 0.02**	0.36 ± 0.02	0.43 ± 0.01	**0.55 ± 0.01**	0.42 ± 0.02
[Z/H]	$0.60 \leq z_{LEGA-C} \leq 0.68$	0.26 ± 0.03	**0.37 ± 0.04**	0.23 ± 0.03	0.16 ± 0.03	**0.27 ± 0.03**	0.21 ± 0.04
[Z/H]	$0.68 < z_{LEGA-C} \leq 0.76$	0.27 ± 0.03	**0.46 ± 0.03**	0.29 ± 0.04	0.11 ± 0.03	0.30 ± 0.04	0.26 ± 0.04
Age	$0.014 \leq z_{SAMI} \leq 0.10$	0.08 ± 0.02	0.15 ± 0.02	0.13 ± 0.02	0.21 ± 0.01	0.34 ± 0.02	**0.40 ± 0.02**
Age	$0.60 \leq z_{LEGA-C} \leq 0.68$	0.12 ± 0.03	0.09 ± 0.04	0.01 ± 0.04	0.24 ± 0.03	**0.30 ± 0.03**	0.18 ± 0.04
Age	$0.68 < z_{LEGA-C} \leq 0.76$	0.11 ± 0.03	-0.07 ± 0.04	-0.11 ± 0.04	0.24 ± 0.03	0.26 ± 0.04	0.05 ± 0.04

thus resulting age measurements) are not well constrained (e.g. McDermid et al. 2015; Scott et al. 2017), therefore, differences in stellar population synthesis methods and models can induce systematic offsets in the absolute age and metallicity value assigned to each galaxy. However the rank order of galaxies relative to each other, and therefore scaling relations, should remain consistent. We find the age–M_* and [Z/H]–M_* relations are consistent in shape across all three redshift bins (with massive galaxies being older and more metal rich), in agreement with the study by Gallazzi et al. (2014) in a similar redshift range. Furthermore, in agreement with Choi et al. (2014), our measurements show negligible evolution in [Z/H] at fixed mass across the three redshift bins.

We estimate uncertainties for the age and metallicity measurements for both the LEGA-C and SAMI samples by randomly shuffling the residuals between the best-fit and the observed spectrum, which are then reassigned to the best-fit spectrum and refit. This process is repeated 100 times per galaxy, building up a distribution of values in age and metallicity. To ensure we preserve any wavelength dependence of the residuals in this process, the residuals are reassigned within wavelength bins approximately 500 Å wide. The distributions are approximately Gaussian and centred around the original fit value, so we take the standard deviations of the distributions as the uncertainties on the original age and metallicity measurements. The median uncertainties in the three redshift bins are $\sigma_{[Z/H]} = 0.03$, 0.07, and 0.07 dex for metallicity (shown in Figures 5 and 6) and $\sigma_{\log \mathrm{Age}} = 0.03$, 0.08, and 0.08 dex for log Age (shown in figures 9 and 10) for $0.014 \leq z_{SAMI} \leq 0.10$, $0.60 \leq z_{LEGA-C} \leq 0.68$, and $0.68 < z_{LEGA-C} \leq 0.76$ respectively.

For both the SAMI and LEGA-C stellar population fits, we allow for the full range of template ages (0.063 to 17.78 Gyr), despite the age of the Universe at $z = 0.76$ being ~ 7 Gyr. This is because the absolute age of stellar population templates is not well constrained (e.g. McDermid et al. 2015; Scott et al. 2017), and therefore we focus instead on the *relative* difference between age measurements and templates. Using the full set of templates also provides a key way to determine the reliability of our age measurements. 26 (5%) of LEGA-C age measurements are older than 8 Gyr, indicating that for 95% of the data the ages are constrained to be younger than the age of the Universe by the data alone, despite allowing for older templates. Additionally, these 26 galaxies have larger age uncertainties than the rest of the sample (mean $\sigma_{\log \mathrm{Age}} = 0.09$ dex for log Age ≥ 8 Gyr, compared to mean $\sigma_{\log \mathrm{Age}} = 0.06$ dex for log Age < 8 Gyr), therefore these 26 too-old galaxies are already down-weighted in the analysis.

4.3.2. Linear and Planar fits

All linear fits are done using a Bayesian approach as outlined by Hogg et al. (2010) for N points with Gaussian uncertainties on x and y ($\sigma_{x,n}$, $\sigma_{y,n}$), and intrinsic variance in the y-direction (λ^2). Therefore the log-likelihood $\log p$ for slope m and intercept b is:

$$\log p = -0.5 \sum_{n=1}^{N} \left(\frac{\Delta_n^2}{\Sigma_n^2} + \log \Sigma_n^2 \right) \tag{4.5}$$

Where

$$\Delta_n = y_n - m x_n - b \tag{4.6}$$

$$\Sigma_n = (-m, 1) \cdot \begin{pmatrix} \sigma_{x,n}^2 & 0 \\ 0 & \sigma_{y,n}^2 \end{pmatrix} \cdot (-m, 1)^T + \lambda^2 \tag{4.7}$$

The posterior function takes uniform priors on the angle of the line and the intercept, and a Jeffreys (1946) prior on the intrinsic scatter in the y-direction ($P(\sigma) \propto 1/\sigma$).

We first find the mode of the posterior function using the Differential Evolution numerical method (Storn & Price 1997; Price et al. 2005). This is followed by Markov Chain Monte Carlo integration of the posterior distribution to estimate the uncertainties on the model parameters, using the Python package EMCEE (Foreman-Mackey et al. 2013), which implements the affine-invariant ensemble sampler of Goodman & Weare (2010). A similar Bayesian approach is used for the plane fits in Section 4.4.1, with uniform priors on the slopes and intercepts and a Jeffreys (1946) prior on the intrinsic scatter in the z-direction (i.e. in metallicity). The 2 dimensional likelihood (equation 4.5) can be generalised to 3 dimensions with slopes m_1, m_2:

$$\Delta_n = z_n - m_1 y_n - m_2 x_n - b \tag{4.8}$$

$$\Sigma_n = (-m_1, -m_2, 1) \cdot \begin{pmatrix} \sigma_{x,n}^2 & 0 & 0 \\ 0 & \sigma_{y,n}^2 & 0 \\ 0 & 0 & \sigma_{z,n}^2 \end{pmatrix} \cdot (-m_1, m_2, 1)^T + \lambda^2 \tag{4.9}$$

For illustrative purposes we emphasise the presence/absence of residual trends by smoothing the colour distributions using the LOESS locally weighted regression algorithm (Cleveland & Devlin 1988; Cappellari et al. 2013) with a fraction of 0.4 points used in the local approximation. However all fits are done on the unsmoothed data. The LOESS algorithm takes into account the uncertainty on the stellar population parameter (age or metallicity), therefore highly uncertain points may have a significantly different value in the LOESS smoothed colour map compared to the unsmoothed data. We note that these smoothed colour scales are useful to highlight broad age and metallicity variations in the data, but should not be interpreted as reliable for individual datapoints.

4.3.3. Non-Parametric Measure of Correlation

In Table 4.1 we present the Spearman rank-order correlation coefficient along with its 1σ uncertainty for the relations between stellar population parameters age and [Z/H], and the

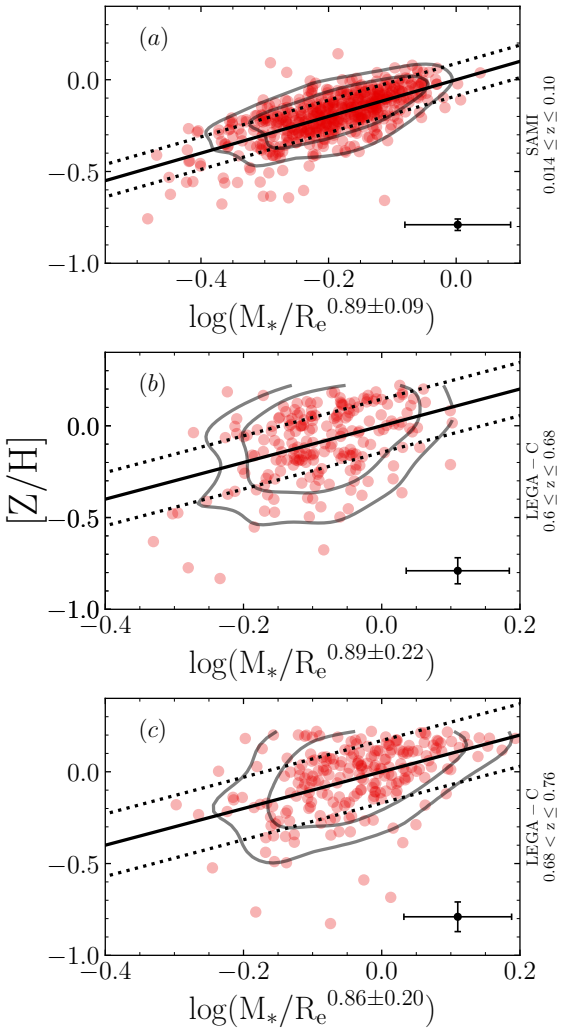

Figure 4.7 Stellar metallicity [Z/H] versus the best-fit linear combination of M_* and R_e for the three redshift bins. The top panel (a) shows the SAMI galaxies $0.014 \leq z \leq 0.10$, the middle panel (b) shows the LEGA-C galaxies with $0.60 \leq z \leq 0.68$, and the bottom panel (c) the LEGA-C galaxies with $0.68 < z \leq 0.76$. The best-fits are shown by the black solid line with the fitted 1σ intrinsic scatter (black dotted lines). The median uncertainty on the M_*, R_e and [Z/H] are shown by the example point in the bottom right corner of each panel. The best-fit ratio of coefficients between $\log M_*$ and $\log R_e$ is statistically consistent within $\sim 2\sigma$ across all three redshift bins and with a ratio of -1.

structural parameters of mass, gravitational potential, and surface-density using both M_* and M_D. We estimate the uncertainty on the Spearman coefficients by generating 1000 different datasets consistent with our original measurements. Specifically, each datapoint is sampled 1000 times from a gaussian distribution centered on the datapoint's "true" value and with a width equal to the uncertainty on that datapoint. For all relations the distribution of Spearman coefficients is consistent with Gaussian. We therefore use the standard deviation of the distribution as the uncertainty on the coefficient.

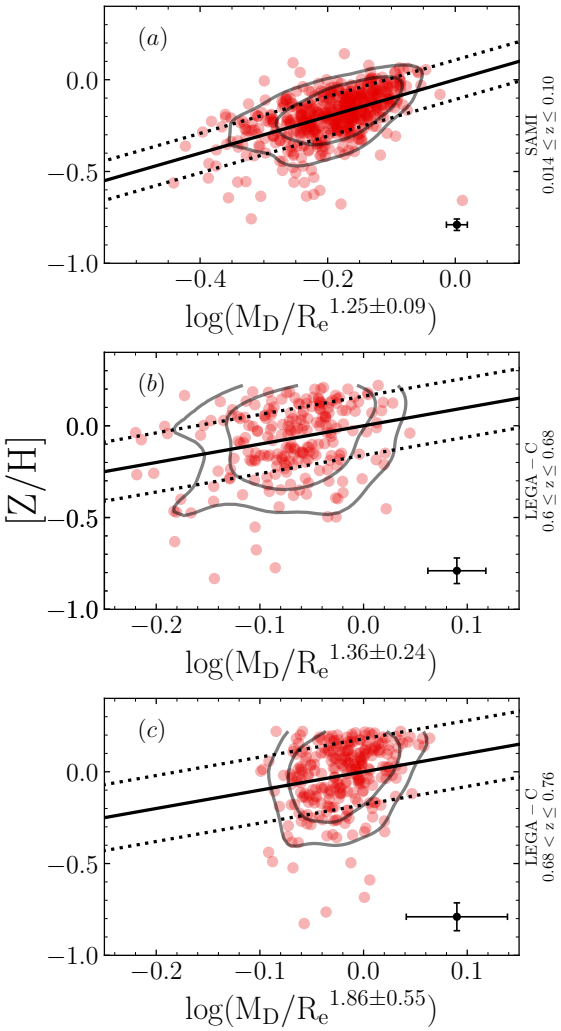

Figure 4.8 Stellar metallicity [Z/H] versus the best-fit linear combination of M_D and R_e for the three redshift bins. The top panel (a) shows the SAMI galaxies $0.014 \leq z \leq 0.10$, the middle panel (b) shows the LEGA-C galaxies with $0.60 \leq z \leq 0.68$, and the bottom panel (c) the LEGA-C galaxies with $0.68 < z \leq 0.76$. The best-fits are shown by the black solid line with the fitted 1σ intrinsic scatter (black dotted lines). The median uncertainty on the M_D, R_e and [Z/H] are shown by the example point in the bottom right corner of each panel. The best-fit ratio of coefficients between $\log M_D$ and $\log R_e$ is statistically consistent within $\sim 3\sigma$ across all three redshift bins and with a ratio of -1.

4.4. Results

4.4.1. Metallicity [Z/H]

We start by showing how luminosity-weighted [Z/H] varies in the mass–size plane using both the stellar mass M_* (Figure 4.5) and the dynamical mass proxy M_D (Figure 4.6). In all three redshift bins (rows) of Figures 4.5 and 4.6 we see significant dependence of metallicity on both mass and size. The LOESS-smoothed distributions (middle column) highlight that [Z/H] varies essentially along lines of constant M/R_e (dashed lines).

The right columns of Figures 4.5 and 4.6 quantify this variation by showing how the residuals from the best-fit mass–size relation trend with [Z/H], where the residuals are the perpendicular distance between the model minus the data. The low-redshift SAMI sample

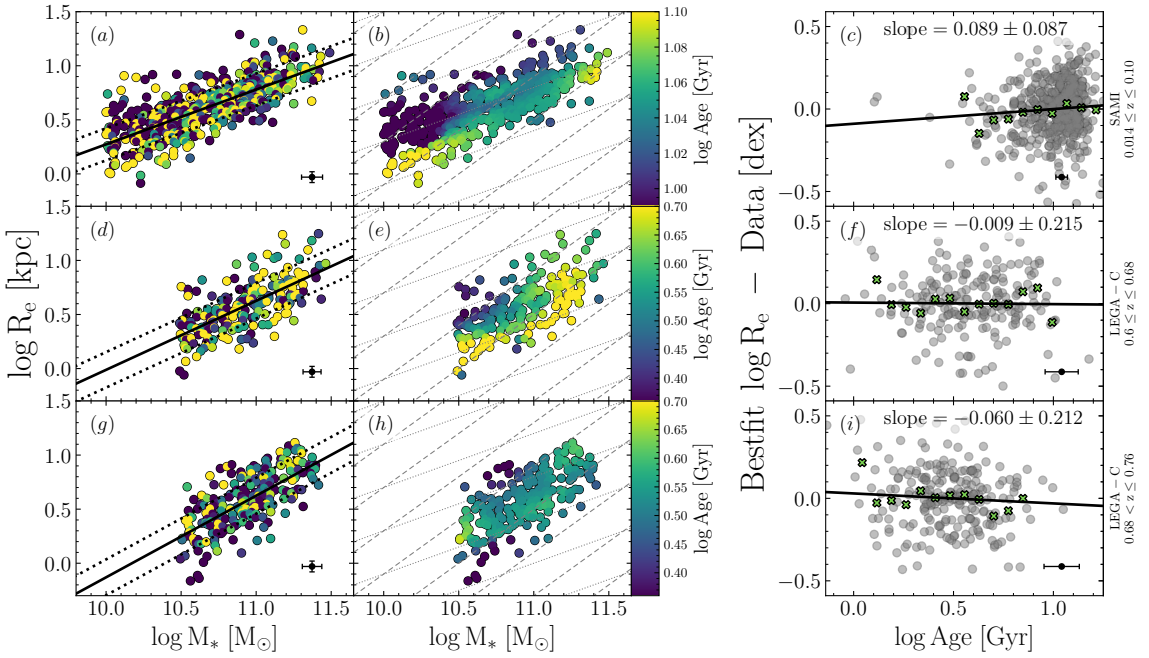

Figure 4.9 Stellar age in the stellar mass–size plane for quiescent galaxies in the three redshift bins. The top row shows the SAMI data with $0.014 \leq z \leq 0.10$, middle row the LEGA-C data with $0.60 \leq z \leq 0.68$, and the bottom row the LEGA-C data with $0.68 < z \leq 0.76$. The colour scale of the left column represents the stellar age, and the centre column shows the smoothed age using the LOESS algorithm. Note that the top row has a different colour scale range then the middle and bottom rows. The best-fits are shown in the left column (black solid line) with the fitted 1σ intrinsic scatter (black dotted lines). The median uncertainty on the mass, size and age are shown by the example point in the bottom right corner of the left and right columns. In the centre column the dashed lines show constant M_*/R_e and the dotted lines show constant surface mass density $\Sigma \propto M_*/R_e^2$. The right column shows the dependence of the residuals (defined as the perpendicular distance between the model minus the data) from the best-fit mass–size relation with age. The black line in the right column is the best-fit relation to the residuals, with the slope written at the top of each panel. The crosses show the median value in independent bins with 3 or more galaxies. This Figure illustrates that variations in age in the mass–size plane change with redshift.

shows the strongest trend between the mass–size residuals and [Z/H], with panel c in Figures 4.5 and 4.6 both having 3σ positive trends (i.e. smaller galaxies at fixed mass are more metal rich). The LEGA-C samples also show positive trends between the residuals and [Z/H], however with decreased statistical significance due to the smaller sample size compared to SAMI.

Table 4.1 further emphasises the dependence of [Z/H] on M/R_e. It shows that, for both M_* and M_D, the structural parameter leading to the highest Spearman correlation coefficient is M/R_e. For stellar mass, M_*/R_e is the highest coefficient by at least $2\sigma_\rho$ for all three redshift samples. Dynamical mass shows a similar result with [Z/H]–M_D/R_e being highest with over $3\sigma_\rho$ significance for the SAMI sample, although for the LEGA-C samples the [Z/H]–M_D/R_e coefficient is less than $2\sigma_\rho$ larger than [Z/H]–M_D/R_e^2. The [Z/H]–M_D/R_e coefficients are, however, all 2-$3\sigma_\rho$ larger than [Z/H]–M_D, indicating that at fixed mass [Z/H] has a significant dependence on R_e in all three redshift bins.

We further quantify the dependence of [Z/H] on both mass and size in Figures 4.7 and 4.8, which show [Z/H] fit as a linear combination of $\log M$ and $\log R_e$, [Z/H]= $a \log M + b \log R_e + c$. In Figure 4.7 the ratio of the coefficients of $\log M_*$ and $\log R_e$ in the best-fit

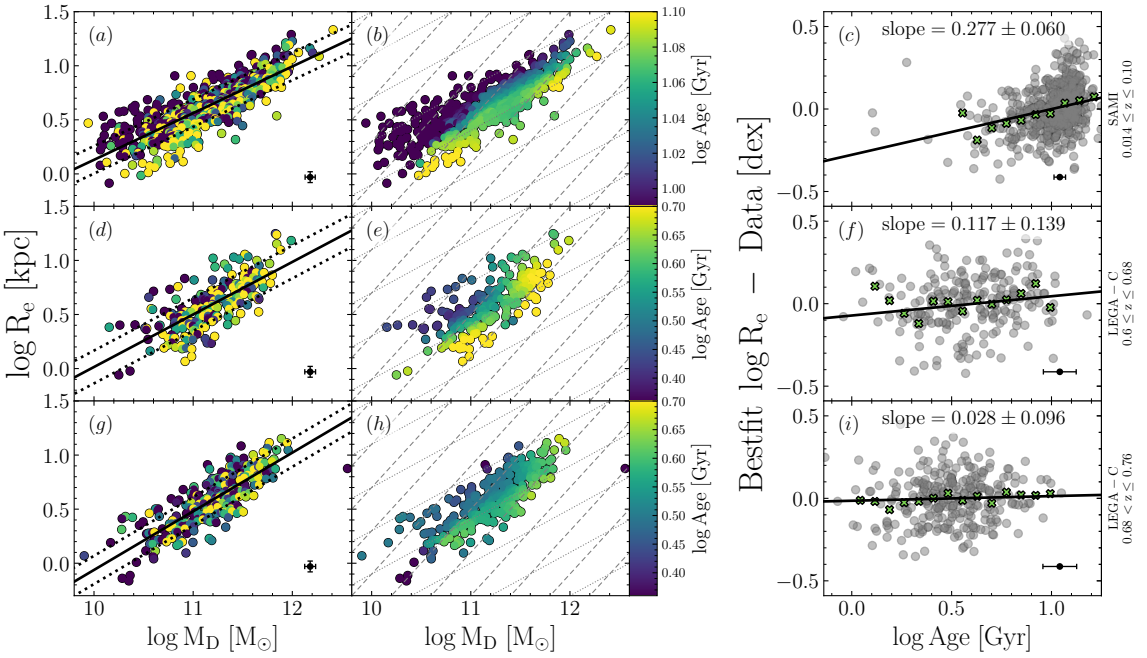

Figure 4.10 Stellar age in the dynamical mass–size plane for quiescent galaxies in the three redshift bins. The top row shows the SAMI data with $0.014 \leq z \leq 0.10$, middle row the LEGA-C data with $0.60 \leq z \leq 0.68$, and the bottom row the LEGA-C data with $0.68 < z \leq 0.76$. The colour scale of the left column represents the stellar age, and the centre column shows the smoothed age using the LOESS algorithm. Note that the top row has a different colour scale range then the middle and bottom rows. The best-fits are shown in the left column (black solid line) with the fitted 1σ intrinsic scatter (black dotted lines). The median uncertainty on the mass, size and age are shown by the example point in the bottom right corner of the left and right columns. In the centre column the dashed lines show constant M_D/R_e and the dotted lines show constant surface mass density $\Sigma \propto M_D/R_e^2$. The right column shows the dependence of the residuals (defined as the perpendicular distance between the model minus the data) from the best-fit mass–size relation with age. The black line in the right column is the best-fit relation to the residuals, with the slope written at the top of each panel. The crosses show the median value in independent bins with 3 or more galaxies. This Figure illustrates that variations in age in the mass–size plane change with redshift.

relations are $a/b = -0.89 \pm 0.09$, -0.89 ± 0.22, -0.86 ± 0.20 for $z \in [0.014, 0.10]$, $z \in [0.60, 0.68]$, and $z \in [0.68, 0.76]$ respectively. All three ratios are within 1–2σ uncertainty of -1, the ratio representing the gravitational potential ($\Phi \propto M_*/R_e$). Furthermore these ratios are significantly different from 0 (the ratio representing scaling solely with M_*) and 2 (scaling with surface density $\Sigma \propto M_*/R_e^2$).

We find a similar result in Figure 4.8 using the dynamical mass proxy M_D, however we note a slight difference in the optimal coefficient ratio when using M_* and M_D; the planar fits with M_* have ratios slightly above -1 (-0.86 to -0.89), while the fits with M_D all have ratios slightly below -1 (-1.25 ± 0.09, -1.36 ± 0.24, and -1.86 ± 0.55 for $z \in [0.014, 0.10]$, $z \in [0.60, 0.68]$, and $z \in [0.68, 0.76]$ respectively). Although, similarly to Figure 4.7, all three ratios with M_D are within 1–3σ of -1 representing the gravitational potential. For the highest redshift bin the ratio -1.86 ± 0.55 is closer to -2, although it is still consistent within 2σ to -1. Additionally, the Spearman coefficient in the highest redshift bin is slightly higher for [Z/H]–M_D/R_e ($\rho = 0.30 \pm 0.04$) than for M_D/R_e^2 ($\rho = 0.26 \pm 0.04$).

4.4.2. Age

We show how luminosity-weighted age varies in the mass–size plane using both the stellar mass M_* (Figure 4.9) and the dynamical mass proxy M_D (Figure 4.10). Unlike [Z/H] which shows clear results using either M_* or M_D, the age results are clearer when using M_D compared to M_*. We therefore focus on these the results with M_D (Figure 4.10), and note that the results with M_* are weaker but qualitatively consistent. Overall our results show that stellar age scales with mass and size differently across redshift. For a clear visual representation of the results, we can compare the smoothed colour scale in the middle column from the lowest to the highest redshift bin (middle column, top to bottom row of Figure 4.10). In the lowest redshift bin there is a significant variation in age perpendicular to the best-fit mass–size relation (panels b), approximately along lines of constant surfance density (dotted lines). This age trend is further highlighted by the right column (panels c) which shows the relation between age and the residuals (orthogonal distance between model − data) from the mass–size best-fit, which shows a positive trend (i.e. smaller galaxies at fixed mass are older). Additionally, Table 4.1 shows that the highest Spearman coefficient for the SAMI age relations with M_D is M_D/R_e^2. Figure 4.9b shows that age also varies perpendicular to the best-fit stellar mass–size plane at low redshift.

Unlike for the SAMI galaxies, neither LEGA-C redshift bins show a statistically significant trend with the mass–size plane residuals; the slopes in panels (f) and (i) in Figures 4.9 and 4.10 are all within 1σ of zero. From Table 4.1 the only LEGA-C age relation with a Spearman coefficient statistically different (at least $1\sigma_\rho$) from the next highest value is Age–M_D/R_e for $0.60 \leq z \leq 0.68$. For the highest redshift bin, $0.68 < z \leq 0.76$, the Spearman coefficient for age–M_D/R_e ($\rho = 0.26 \pm 0.04$) and age–M_D ($\rho = 0.24 \pm 0.03$) are consistent within the uncertainties. Therefore, the age goes from trending with surface density (M/R_e^2) at low redshift, to a mild trend with M/R_e in the intermediate redshift bin, to a weak trend with M or M/R_e in the highest redshift bin. The change in the correlation between age and Σ with redshift suggests the relation observed at $z \sim 0$ is built up over time and that at least one of the processes driving the evolution of mass, size and/or star formation history has a redshift dependence.

Similarly to Figures 4.7 and 4.8 for [Z/H], we performed planar fits to age as a linear combination of $\log M$ and $\log R_e$. Unlike [Z/H] however, for the LEGA-C age relations, we are unable to disentangle the weak trends between age–M and age–R_e from the strong M–R_e trend itself. As a result, in a planar fit to $\log \text{Age} = a \log M + b \log R_e + c$, $\log M$ and $\log R_e$ are not independent variables. Statistically this is a multicollinearity problem, and the result is that the posterior distributions of the planar fits indicate a wide range of parameter values are plausible, because the fit becomes $\log \text{Age} = (a + b) \log M + c$ and the coefficients a and b are unconstrained. Therefore we do not include these fits. We note, however, that a similar analysis for a larger subset of SAMI galaxies (Chapter 2) confirms that, at $z \sim 0$, the most precise predictor of log Age is surface mass density (whether photometric or spectroscopic).

We note in particular that in the $z \sim 0$ mass–size plane age trends along lines of constant $\Sigma \propto M/R^2$ (i.e. lines with slope = 0.5), which is remarkably similar to the slope of the quiescent population itself in the mass–size plane. This result is evident from the unsmoothed data (panel a), but clearest in the LOESS-smoothed data in panel b of Figure 4.10 which shows that the LOESS-smoothed age varies perpendicularly to the mass–size relation. In Section 4.5.2

we investigate how the $z \sim 0$ age–Σ relation relates to the slope of the quiescent population in the mass–size plane and show how it results from the build-up of the quiescent population over time.

4.5. Discussion

Our aim was to investigate how scaling relations between galaxy structure and global stellar metallicity and age change across ~6 Gyr, to understand the redshift dependence in stellar population evolution. We aimed to test two hypotheses:

1. The [Z/H]–M/R_e relation is consistent with the gravitational potential regulating the retention of stellar and supernova ejecta via its relation to the escape velocity; if this is true, there should be a relation at every redshift.

2. The $z \sim 0$ age–Σ relation is built up over time due to galaxies forming and evolving more compactly (diffusely) at higher (lower) redshifts; in this case, the age–Σ relation should be less prominent at intermediate redshifts than at $z \sim 0$.

Our results support both these hypotheses: (i) The metallicity of intermediate-redshift quiescent galaxies, like that of low-redshift quiescent (Chapter 2) and star-forming galaxies (Chapter 3), is strongly correlated with M/R_e (Section 4.4.1); we discuss this further in Section 4.5.1. (ii) At intermediate redshifts, there is no statistically significant correlation between global stellar age and surface mass density (Section 4.4.2). We show how the $z \sim 0$ age–Σ is consistent with the redshift-evolution of the mass–size plane in Section 4.5.2 and further discuss this hypothesis in Section 4.5.2.

4.5.1. The consistency of the [Z/H]–Φ relation across 6 Gyr

We find that from low to intermediate redshift ($z \leq 0.76$) the stellar metallicity of quiescent galaxies correlates more tightly with M/R_e than with other combinations of mass and size. This result is in agreement with the low-redshift results of Chapter 2 and Chapter 3 for the stellar metallicity of quiescent and star-forming galaxies respectively and D'Eugenio et al. (2018) for the gas-phase metallicity of star-forming galaxies. Our results also agree with Díaz-García et al. (2019), who showed that (at fixed mass) smaller quiescent galaxies are more metal-rich since $z \sim 1$. We note that, for non-zero uncertainty on R_e, M_*/R_e^x must have a higher observational uncertainty than M_* alone (for $x \neq 0$). Therefore, our result that the observed [Z/H]–$M_*/R^{\sim 1}$ relation is tighter than the relation with M_* alone means the relation with $M_*/R^{\sim 1}$ must be *intrinsically* tighter.

These studies (Chapters 2 and 3, D'Eugenio et al. 2018) built on earlier works (e.g. Worthey et al. 1992; Trager et al. 2000a) that proposed the global stellar and gas-phase metallicity of a galaxy is regulated by the gravitational potential (Φ), as the depth of the potential well determines the escape velocity required for metal-rich gas to be expelled from the system by supernova, active galactic nuclei (AGN) and/or stellar winds and thus avoid being recycled into later stellar generations. Our finding that the relation also exists at $0.60 \leq z \leq 0.76$ supports this hypothesis.

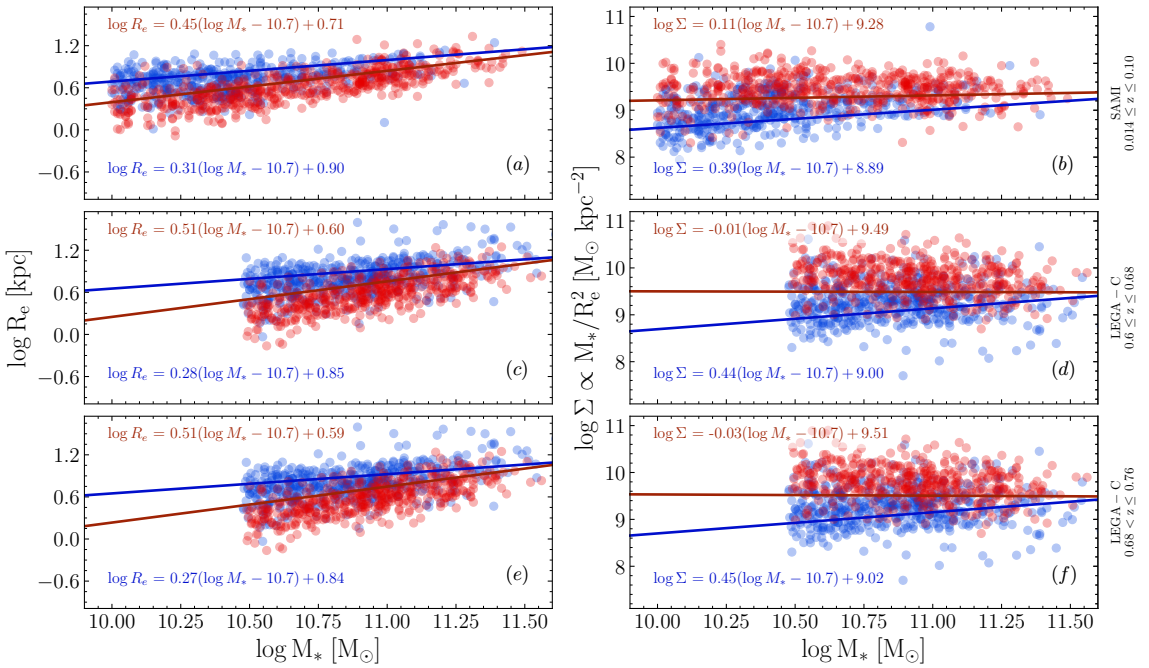

Figure 4.11 Mass–size (left column) and mass–surface density (right column) planes for the three redshifts bins. The top row shows the SAMI data with $0.014 \leq z \leq 0.10$, middle row the LEGA-C data with $0.60 \leq z \leq 0.68$, and the bottom row the LEGA-C data with $0.68 < z \leq 0.76$. The red points are quiescent galaxies and the blue points are star-forming galaxies. In the left columm, the solid red and blue lines are the redshift-dependent mass–size relations to the quiescent and star-forming populations based on the analysis of Mowla et al. (2019). The equations for these relations are written in each panel (in red at the top for quiescent galaxies and in blue at bottom for star-forming galaxies). In the right column, we show the same mass–size relations from Mowla et al. (2019) converted to the mass–surface density plane.

It is interesting to note that the ratio of coefficients of the best-fit planes for the three samples are all consistent within 1σ (for either M_* or M_D). If we simplify the complex process of metal production and outflows to a closed box model and assume the global stellar metallicity results from a balance between metal production determined by the stellar mass and metal retention determined by the gravitational potential and the strength and frequency of gas outflows, our results are consistent with there being no significant change in the balance of these processes from $0.014 \leq z \leq 0.76$. While we are unable to quantitatively test this hypothesis due to differences in the sample selection between the two surveys, future works focusing on the slope and scatter of the [Z/H]–Φ relation across redshift may shed light on this topic, and help place constraints on the strength and efficiency of feedback process in heating and expelling interstellar gas.

4.5.2. The build-up of the age–Σ relation over 6 Gyr

Unlike the metallicity results, we find a significant difference between the age distribution in the mass–size plane at intermediate redshift compared to low redshift. Chapters 2 and 3 found that the global age of both low-redshift early-type and star-forming galaxies tightly correlates with the surface density ($\Sigma \propto M/R_e^2$), whereas we find no significant correlation with Σ in either LEGA-C redshift sample. Comparing the results from the highest to lowest redshift bin, age changes from varying weakly with M and/or M/R_e ($0.68 < z \leq 0.76$), to weakly correlating with M/R_e ($0.6 \leq z \leq 0.68$), to a significant variation with M/R_e^2,

approximately *perpendicular* to the mass–size relation ($0.014 \leq z \leq 0.10$). This suggests that, unlike the [Z/H]–Φ relation, the $z \sim 0$ age–Σ does not reflect a causal relation, but is instead built up over time due to the fact that both age and Σ depend on the conditions of the Universe when a galaxy becomes quiescent. This hypothesis is supported by a number of studies linking age, Σ, and formation epoch. In particular, Kauffmann et al. (2003b, 2006) and Franx et al. (2008) showed that galaxy star formation histories are strongly correlated with surface mass density. This correlation between star formation history and surface density was further refined by Díaz-García et al. (2019) and Zolotov et al. (2015), who showed that central surface density correlates strongly with formation epoch and quenching epoch respectively. We build upon these previous work to relate the change across redshift of the age dependence on mass and size to the evolution of the mass–size relation in the following Section 4.5.2, and show that we can explain the $z \sim 0$ age–Σ relation as being due to the average surface density of galaxies in both the star-forming and quiescent populations decreasing with decreasing redshift.

Age in the mass–size and mass–surface density planes

It is well established that the median size of galaxies in both the quiescent and star-forming populations evolves significantly in the mass–size plane with redshift (Ferguson et al. 2004; Trujillo et al. 2007; Buitrago et al. 2008; Williams et al. 2010). Specifically, van der Wel et al. (2014) and Mowla et al. (2019) showed that for $0 \leq z \leq 3$, the slopes of the mass–size relations for both the quiescent and star-forming populations change little with redshift, but the intercepts decrease with increasing redshift such that high-redshift populations are smaller at fixed mass.

We illustrate this result in the left column of Figure 4.11, which shows our quiescent and star-forming populations in the mass–size plane for each redshift bin. The solid blue and red lines are the redshift-dependent best-fit stellar mass–size relations from Mowla et al. (2019). The left column of Figure 4.11 shows that, while our quiescent galaxy mass estimates are systematically slightly below the Mowla et al. (2019) relations, our samples are in overall good agreement.

Of crucial importance are the slopes of mass–size relations for the quiescent populations. In all three redshift bins the mass–size relation for the quiescent population is approximately $\log R_e \approx 0.5 \log M_*$ (specifically, 0.45, 0.51 and 0.51 for $z \in [0.014, 0.10]$, $z \in [0.60, 0.68]$ and $z \in [0.68, 0.76]$ respectively). This slope of ~0.5 in the mass–size plane means that, at fixed redshift, the quiescent population has an approximately constant surface–mass density regardless of stellar mass. For some redshift-dependent constant $k_1(z)$,

$$\log R_e = 0.5 \log M_* + k_1(z) \tag{4.10}$$

$$\log \Sigma = \log M_* - 2 \log R_e = -2k_1(z) \tag{4.11}$$

which implies that surface density does not change with stellar mass:

$$\frac{\delta \log \Sigma}{\delta \log M_*} = 0 \tag{4.12}$$

Indeed, in the right column of Figure 4.11 we show our samples in the stellar mass–surface density plane. The red and blue lines are the mass–size relations from Mowla et al. (2019)

converted to be in terms of mass and surface density. As expected given the mass–size relations in the left column, the slopes of the quiescent populations are all close to zero (0.11, -0.01, and -0.01 for $z \in [0.014, 0.10]$, $z \in [0.60, 0.68]$ and $z \in [0.68, 0.76]$). Furthermore, as expected, the intercepts in the mass–surface density plane increase with increasing redshift, such that the LEGA-C quiescent galaxies are more compact (higher Σ) than the lower redshift SAMI quiescent galaxies.

The individual evolutionary tracks of star-forming galaxies are expected to closely align with the star-forming population in the mass–size plane, a result supported by both observations and simulations (Lilly et al. 1998; Ravindranath et al. 2004; Trujillo et al. 2006; van Dokkum et al. 2015). Therefore the slope of ~0.3 for the star-forming sequence in the mass–size plane in all three redshift bins means that as galaxies build up their mass via in-situ star formation, they also increase their surface density. For some redshift-dependent constant $k_2(z)$,

$$\log R_e = 0.3 \log M_* + k_2(z) \tag{4.13}$$

$$\log \Sigma = \log M_* - 2 \log R_e = 0.4 \log M_* - 2k_2(z) \tag{4.14}$$

which implies surface density increases with increasing stellar mass:

$$\frac{\delta \log \Sigma}{\delta \log M_*} = 0.4 \tag{4.15}$$

Combining these two key results suggests that star-forming galaxies build their stellar mass, and at the same time increase their stellar surface density until they reach a redshift-dependent threshold surface density at which they quench. As this threshold surface density decreases with decreasing redshift, the quiescent population is built up to include galaxies that have quenched at a range of redshifts and, consequently, with a range of surface densities. In the $z \sim 0$ quiescent population, therefore, a galaxy's surface density reflects the redshift at which it quenched (luminosity-weighted age is closely tied to how long ago the galaxy quenched).

This connection between quenching and galaxy structure, in particular surface density, is in agreement with previous work. Franx et al. (2008) found a redshift-dependent threshold surface density above which galaxies have low sSFR (are quiescent) and below which the sSFR are high with little variation (are star-forming). Franx et al. (2008) also found that the surface density threshold increases with increasing redshift. Similarly, van der Wel et al. (2009) found that stellar velocity dispersion also shows a redshift-dependent threshold separating quiescent and star-forming galaxies. Additionally, González Delgado et al. (2014) found a threshold surface-mass density for low-redshift spheroidal galaxies that is nearly independent of stellar mass, in agreement with our results.

Recent work by Chen et al. (2020) provides a theoretical framework explaining the relation between surface density and quenching. Chen et al. (2020) showed that a galaxy model in which central black hole mass (and therefore strength of AGN feedback) is related to both the host galaxy's mass and size successfully explains key properties of star-forming and quenched galaxies. In the model larger star-forming galaxies at fixed mass have smaller central super-massive black holes (due to their lower central surface density). Therefore these extended galaxies evolve to higher stellar masses before the central AGN has strong enough feedback to shock-heat infalling gas from the halo, quenching star formation.

There remain two unanswered questions: (1) what leads to galaxies forming more compactly at higher redshifts? and (2) what leads to the decrease with time of the redshift-dependent threshold surface density at which star-forming galaxies quench? In relation to the first question, Franx et al. (2008) concluded that compact galaxies must have formed their stars earlier when the Universe was denser and had a higher gas fraction compared to the formation epoch of galaxies with lower surface densities. Wellons et al. (2015) used the Illustris simulations (Genel et al. 2014; Vogelsberger et al. 2014) to trace the star-formation and assembly histories of compact galaxies and found that another dominant mechanism for forming compact galaxies at high redshift are centrally-concentrated starbursts triggered by wet major mergers. Wellons et al. (2015) noted that this wet major merger mechanism is also intrinsically linked to the density and redshift evolution of the Universe; as the Universe expanded and the abundance of cold gas decreased, the likelihood of wet major mergers also decreased with decreasing redshift. While these explanations may underlie the change in the formation and evolution of galaxies across redshift (question 1), they do not explain the origin of the redshift-dependent surface density threshold at which star-forming galaxies quench (question 2). This changing threshold may be due a redshift-dependence of the complex balance between the supply and heating of inflowing gas and the feedback and outflows from star formation and AGN (e.g., Chen et al. 2020).

Clearly, this scenario of a redshift-dependent quenching surface-density requires that passive evolution does not significantly alter the inner structure of quiescent galaxies (inside $\sim$1 R_e); however, we note that if this assumption was incorrect, it would be even harder to explain the observed correlation between stellar population age and surface mass density.

The effect of mergers

Thus far we have only considered the evolution in the average properties of the quiescent and star-forming populations due to the addition (and loss) of new (and old) members. However individual galaxies also grow in mass and size through both minor (mass ratio $\lesssim 0.3$ e.g. Lambas et al. 2012) and major mergers (Oser et al. 2012; Bluck et al. 2012; Oogi & Habe 2013; Ownsworth et al. 2014). Indeed, the relative absence at low redshift of the very compact galaxies frequently observed at high redshift indicates individual galaxies must undergo significant mass–size evolution even after ceasing star formation (van Dokkum et al. 2010). Dry major mergers are expected to increase a galaxy's mass and size proportionally, whereas minor mergers significantly increase a galaxy's effective radius while contributing comparatively little to its stellar mass (Bezanson et al. 2009; Naab et al. 2009; Hopkins et al. 2009). Given these two relations, both major and minor mergers will increase a galaxy's mass but *decrease* its surface mass density and therefore move galaxies down and right in the mass–Σ plane. Specifically, based on results from Naab et al. (2009) and Bezanson et al. (2009):

$$\Delta \log R_{\mathrm{e,major}} \approx \Delta \log M_* \tag{4.16}$$

$$\Delta \log R_{\mathrm{e,minor}} \approx 2\Delta \log M_* \tag{4.17}$$

Therefore the changes in surface mass density are always negative (galaxies become more diffuse):

$$\Delta \log \Sigma_{\rm major} \approx -\Delta \log M_* \tag{4.18}$$

$$\Delta \log \Sigma_{\rm minor} \approx -3\Delta \log M_* \tag{4.19}$$

We can explore the implications of mergers on the build-up of the age–surface density relation by considering a hypothetical scenario in which galaxies quench at a surface density *independent* of redshift (i.e. there is no redshift evolution of the mass–size plane). If we consider only mass growth through mergers (i.e. no star-formation) and assume that older galaxies (those that formed earlier) will on average have undergone more mergers than younger galaxies, this would lead to older galaxies having on average a *lower* surface density than young galaxies at fixed mass—the opposite of the trend seen at $z \sim 0$. Therefore, while individual galaxy evolution through mergers will undoubtedly introduce scatter into the relation, it cannot be the cause of our age results; in fact, it suggests the original relation must be even stronger than observed today. In addition to increasing a galaxy's mass and size, mergers also influence global stellar population properties. In particular the old, metal rich stellar populations of massive compact galaxies are diluted with younger metal-poor stars when merging with smaller, more diffuse systems. Furthermore, mergers can also restart star-formation in quenched galaxies, lowering the mean stellar population age and metallicity. At $z < 1$ between 10–15% of quiescent galaxies are estimated to have undergone rejuvenated star formation (Thomas et al. 2010; Chauke et al. 2019), which may account for some of the intrinsic scatter in the age–Σ correlation.

4.6. Summary and Conclusions

In this study we aimed to test two key hypotheses on the origins of low redshift stellar population scaling relations:

1. The [Z/H]–$M/R_{\rm e}$ relation at $z \sim 0$ is due to the gravitational potential regulating the retention of stellar and supernova ejecta via its relation to the escape velocity. If so, there should also be a tight correlation between [Z/H] and $M/R_{\rm e}$ at intermediate ($z \sim 0.7$) redshifts.

2. The age–Σ relation at $z \sim 0$ is built up over time due to galaxies forming and evolving more compactly (diffusely) at higher (lower) redshifts. If true, at intermediate redshifts the age–Σ relation should be less prominent.

To achieve these goals, we used pPXF and the E-MILES library of synthetic stellar templates to measure global light-weighted stellar ages and metallicities for a representative sample of quiescent galaxies spanning 6 Gyr of cosmic history. The data consists of 524 quiescent galaxies with $0.014 \leq z \leq 0.10$ from the SAMI Galaxy Survey, and 492 quiescent galaxy split between $0.60 \leq z \leq 0.68$ and $0.68 < z \leq 0.76$ from the LEGA-C Survey. We quantified how the global stellar population parameters of age and metallicity vary in the mass–size plane between low ($0.014 \leq z \leq 0.10$) and intermediate ($0.60 \leq z \leq 0.76$) redshifts. Specifically,

we investigated whether the [Z/H]–M/R_e and age–M/R_e^2 relations found at low redshift in Chapter 2 for quiescent galaxies are also present in a sample with similar masses at a lookback time of 6 Gyr. We find the [Z/H]–M/R_e relation is also present at intermediate redshifts but the age–M/R_e^2 relation is not, in agreement with both our hypotheses.

Our conclusion that the [Z/H]–M/R_e also exists at $0.60 \leq z \leq 0.76$ extends our previous results at low redshift for stars (Chapters 2 and 3) and gas (D'Eugenio et al. 2018) and supports the theory that the depth of the gravitational potential well regulates the stellar and gas-phase metallicity by determining the escape velocity required for metal-rich gas to be expelled from the system and thus avoid being recycled into later stellar generations (e.g. Franx & Illingworth 1990).

To understand the change in the way age varies across the mass–size plane from low to intermediate redshift, we consider the evolution of the mass–size plane itself. Specifically, we show that the slope of ~0.5 for the quiescent population in the mass–size plane in this redshift range (Mowla et al. 2019) leads to flat slopes in the mass–surface density plane, with an intercept that decreases with decreasing redshift. This implies that star-forming galaxies reach a redshift-dependent threshold surface density at which they quench. Importantly this threshold is higher at higher redshifts, so that galaxies forming and evolving at higher redshifts reach a higher surface density before quenching compared to low-redshift star-forming galaxies. The age–surface density relation at $z \sim 0$ is therefore the result of the build-up of the low redshift quiescent and star-forming populations from galaxies that have formed, evolved, and quenched over a range of redshifts, and hence over a range of surface densities. Consequently, the age–surface density relation at $z \sim 0$ arises from the cumulative effect of the redshift-dependent processes that drive the evolution of the star-forming and quiescent populations in the mass–size plane.

Future spectroscopic surveys such as MOONRISE (Maiolino et al. 2020) will help to push this relation to higher redshift ($z \sim 1 - 2.5$) while the large sample size and mass range of the Hector survey (Bryant et al. 2020) at $z \sim 0$ will allow exploration of these relations in the low-mass regime.

CHAPTER 5

Conclusions

5.1. Summary

In this thesis we focussed on the link between galaxy structure and mean stellar population properties in order to understand what leads to the wide variety of properties observed in the low-redshift population; i.e. what drives the evolution of a galaxy's stellar population. The result of this thesis has been the identification, analysis, and interpretation of the origins of two specific scaling relations: (1) the [Z/H]–Φ relation, and (2) the age–Σ relation. In this Chapter we first summarise how each preceding Chapter refined our understanding of these two scaling relations and yielded additional results along the way. We then discuss areas for future work and finish with some concluding remarks.

5.1.1. Low Redshift Early-Type Galaxies

In Chapter 2 (Barone et al. 2018) we analysed how the stellar population parameters metallicity, age, and α-enhancement, measured from Lick indices (Scott et al. 2017) within $1R_e$, as well as $g-i$ colour, correlate with the galaxy structural properties of mass, gravitational potential ($\Phi \propto M/R$), and surface density ($\Sigma \propto M/R^2$) for 625 early-type galaxies from the SAMI galaxy survey (Croom et al. 2012). For each structural parameter we employed two mass estimators: a stellar mass based on photometric luminosity and colour (M_*) and a dynamical mass based on spectroscopic velocity dispersion σ and the virial theorem ($M_D \propto \sigma^2 R_e$).

Earlier studies identified that the residuals from the best-fit stellar population–mass relations correlate with galaxy size, in that smaller galaxies tend to be older and more metal-rich at fixed mass (e.g. McDermid et al. 2015; Scott et al. 2017; Li et al. 2018). Our contribution to this field was to quantify this residual dependence with size and relate it to structural properties. Through careful consideration of observational uncertainties, we determined that for all four stellar population parameters there were tighter correlations (i.e. lower scatter and less residual trend with size) compared to mass alone with either the galaxy's gravitational potential or its surface density. The main results from this chapter are:

(i) $g-i$ colour correlates best with Φ, in that the $g-i$ colour–Φ relation is both tighter and the red and blue sequences are better aligned with each other compared to the $g-i$ colour–mass relation.

(ii) Total metallicity [Z/H] correlates best with Φ.

(iii) Age correlates best with Σ, while $[\alpha/\mathrm{Fe}]$ correlates strongly with both Φ and Σ.

(iv) We showed that correlations with velocity dispersion (σ) are reproduced using the purely photometric estimator of the gravitational potential M_*/R_e.

From results (ii) and (iii) we made the following inferences. Based on result (ii) we inferred that the gravitational potential is the primary factor determining the retention of metals ejected in supernova and stellar winds, via its relation to the gas escape velocity. The correlation therefore reflects a causal relation and so there should also be a similar correlation in star-forming galaxies. We qualitatively discussed how this relation could be preserved through mergers using the simulation results of Boylan-Kolchin & Ma (2007). This study showed that, when accreting onto a host, low-density satellites are easily disrupted and so a large fraction of their mass is accreted by the host at large radii. Conversely, high-density satellites tend to survive multiple passes, so their mass is accreted closer to the centre of the host. Diffuse, low-metallicity satellites will therefore lower both the gravitational potential and metallicity of the host by adding low-metallicity material at large radii, maintaining the pre-existing [Z/H]–Φ correlation.

For result (iii) we proposed two possible explanations: (1) the age–Σ and $[\alpha/\mathrm{Fe}]$–Σ correlations are the result of compactness-driven quenching mechanisms and so these relations exist only in the quenched population, and/or (2) compact galaxies formed earlier with higher gas surface densities and so the correlations are fossil records of the $\Sigma_\mathrm{SFR} \propto \Sigma_\mathrm{gas}$ relation (Schmidt 1959; Kennicutt 1998; Federrath et al. 2017) in their disk-dominated star-forming progenitors, implying that there should also be a correlation in star-forming galaxies.

To investigate our hypotheses we formulated two tests that hinge on the relations found in star-forming galaxies: (1) based on our hypothesis for the origin of the [Z/H]–Φ correlation in early-type galaxies, the same relation *should* also exist in star-forming galaxies; and (2) we can distinguish between the two plausible explanations for the age–Σ relation in early-type galaxies (compactness-driven quenching mechanisms or a fossil record of the $\Sigma_\mathrm{SFR} \propto \Sigma_\mathrm{gas}$) by testing *whether* the same relation also exists in star-forming galaxies. The following Chapters build on the results of Chapter 2 and have the aim of testing these two hypotheses.

5.1.2. Low Redshift Star-Forming Galaxies

In Chapter 3 (Barone et al. 2020) we investigated whether the [Z/H]–Φ and age–Σ scaling relations presented in Chapter 2 for early-types also exist in star-forming galaxies. Specifically, we analysed how age and metallicity within $1R_e$, measured from full spectral fits, correlate with the galaxy structural properties stellar mass M_*, gravitational potential $\Phi \propto M_*/R_e$, and surface density $\Sigma \propto M_*/R_e^2$ for 2085 star-forming galaxies from the SSDS Legacy survey (York et al. 2000; Strauss et al. 2002).

We find that star-forming galaxies, like early-types, also show tight scaling relations between [Z/H]–Φ and age–Σ. Finding these trends in both studies (Chapters 2 and 3), despite the different samples, methods, and models used to derive not only the stellar population parameters but also the stellar masses and effective radii, suggests our results are robust. We discussed various mechanisms that could lead to these relations and rule out those disfavoured by observations.

For the [Z/H]–Φ relation we find our results are well described by the hypothesis of Chapter 2 that Φ regulates the retention of gas-phase metals. This result is also in strong agreement with D'Eugenio et al. (2018), who found that the gas-phase metallicity of star-forming galaxies also correlates best with the gravitational potential. We expanded upon the discussion presented in Chapter 2, in particular discussing evidence from Scott et al. (2009) and Møller & Christensen (2020) that the global relation originates on local scales within galaxies. In addition to furthering our discussion on this hypothesis, we rule out the following mechanisms:

- Do low-Φ galaxies produce fewer metals? To first order the total metal content reflects the number of generations of stars the galaxy has formed. However, we can rule out the [Z/H]–Φ relation being the result of the number of stellar generations due to the existence of a strong correlation between the star formation duration (predicted from [α/Fe]) and the gravitational potential in both late types (Ganda et al. 2007) and early types (Nelan et al. 2005; Thomas et al. 2005, 2010; Robaina et al. 2012; McDermid et al. 2015; Scott et al. 2017; Chapter 2)—specifically, at fixed mass, galaxies with a shallower potential have longer, rather than shorter, star formation durations compared to galaxies with deeper potentials, and thus produce more metals.

- Is the [Z/H]–Φ relation a result of a varying IMF? The slope of the high-mass end of the IMF significantly influences chemical abundance yields; in that more high-mass stars leads to greater chemical enrichment (e.g. Vincenzo et al. 2016). However, metallicity has been suggested to *anticorrelate* with the relative number of high-mass stars (Marks et al. 2012); indicating that variation in the high-mass end of the IMF is not the leading cause of the variation in metallicity. Additionally, recent works have found, using spatially resolved measurements, that IMF variations do not follow [Z/H] variations (Martín-Navarro et al. 2019).

We proposed in Chapter 2 that the age–Σ relation could be due to compactness-driven quenching mechanisms and/or it could be a fossil record of the $\Sigma_{SFR} \propto \Sigma_{gas}$ relation in disk-dominated star-forming progenitors. Assuming the mechanism(s) leading to this relation

is (are) the same for both early-type and star-forming galaxies, the relation must originate *before* quenching. However certain quenching mechanisms, such as gaseous inflows from the disk and mergers, while unlikely to be the dominant drivers of this relation, may further emphasize a pre-existing relation.

5.1.3. Age and Metallicity Relations over 6 Gyr

In Chapter 4 (Barone et al. 2022) we used the LEGA-C Survey (van der Wel et al. 2016) to analyse if (and how) the [Z/H]–Φ and age–Σ scaling relations evolve over a lookback time of 7 Gyr ($0.04 \leq z \leq 0.76$). We analysed full spectral fits of galaxies from LEGA-C within two redshift bins, $0.60 \leq z \leq 0.68$ and $0.68 < z \leq 0.76$, and compare to a similar-mass sample at $0.04 \leq z \leq 0.11$ from the SAMI survey. On the assumption that the gravitational potential regulates the retention rate of metals, this causal relation should affect all galaxies to some degree, and hence there should also be a [Z/H]–Φ correlation in the LEGA-C samples. However the slope and scatter of the relation may change depending upon changes in the strength of outflows and feedback processes with redshift. Conversely, the hypothesis for the age–Σ relation is that it results from compact galaxies having formed earlier than their diffuse counterparts. Hence, in the redshift range probed by LEGA-C, the relation should have had less time to build up and so should be less pronounced than at $z \sim 0$. The aim of this Chapter was to test these explicit hypotheses by determining the redshift dependence of the age–Σ and [Z/H]–Φ scaling relations.

We found and concluded that from low to intermediate redshift ($z \leq 0.76$), the stellar metallicity of quiescent galaxies correlates most tightly with the gravitational potential, compared with other combinations of mass and size. This supports the hypothesis that the gravitational potential regulates metal retention. Qualitatively, our results are consistent with there being no change in the slope of the relation, which could indicate (and provide constraints on) changes in the strength of feedback processes and outflows across this redshift range.

We also found a significant difference in how age varies in the mass–size plane at intermediate redshift compared to low redshift. Age changes from varying *along* the relation in the mass–size plane at $0.68 < z \leq 0.76$, to having no significant correlation in any direction at $0.6 \leq z \leq 0.68$, to a strong variation *perpendicular* to the mass–size relation (along lines of constant Σ) at $0.04 \leq z \leq 0.11$. We contextualised our results in terms of redshift evolution in the mass–size plane. We show that, based on previous results of the redshift evolution of star formation histories and the mass–size plane (Kauffmann et al. 2003b, 2006; Franx et al. 2008; Mowla et al. 2019), star-forming galaxies reach a redshift-dependent threshold surface density at which they quench, such that galaxies that quench at high redshift do so at a higher surface density. Hence the $z \sim 0$ quiescent population is built up from galaxies that have quenched at a range of redshifts and therefore a range of surface densities. The star-forming sequence also evolves in the mass–size plane, leading to a similar relation between age and surface density for star-forming galaxies at $z \sim 0$. The age–surface density relation at $z \sim 0$ is therefore a natural consequence of the cumulative redshift evolution of the galaxy population in the mass–size plane and does not reflect a causal relation between surface density and mean age (except indirectly, through the redshift-dependent surface density threshold for quenching).

5.2. Future Work

In this Section we propose further analyses which aim to test our two main claims: (1) that the [Z/H]–Φ relation is due to the gravitational potential regulating metal retention; and (2) that the $z \sim 0$ age–Σ relation is built up over time due to galaxies forming and evolving more compactly at earlier times.

5.2.1. Metallicity of the Circumgalactic Medium

To first order, stellar mass determines the amount of metals produced in a galaxy. Therefore two galaxies of the same stellar mass but different sizes (and gravitational potentials) will produce the same amount of metals (assuming a non-varying IMF). However, given that the shallower-potential galaxy loses a larger fraction of its metals in galactic outflows produced by star-formation and AGN feedback, we should see a relatively higher metal enrichment of the circumgalactic medium around shallower-potential (larger) galaxies relative to deeper-potential (smaller) galaxies of the same stellar mass.

Using observations of the circumgalactic medium probed by background quasars along the line-of-sight, we can look into whether the structure and dynamics, and in particular the gravitational potential, of the host galaxy correlates with the gas-phase metallicity of its circumgalactic medium. Currently this program is limited by the small sample sizes of circumgalactic medium observations (e.g. 47 galaxies in Pointon et al. 2019). As the metallicity of the circumgalactic medium is sensitive to both internal star-formation processes and environmental factors such as inflows and tidal interactions with neighbours (Tumlinson et al. 2017), larger data sets (of a few hundreds or thousands, e.g. Anand et al. 2021) are likely needed to control for these potentially confounding effects and determine whether the trend we predict exists.

5.2.2. Metallicity of Extreme Systems

The galaxies studied in this thesis are all in the mass range $\sim 10^9$–$10^{11}\,M_\odot$, with sizes typical of galaxies of that mass. By analysing the [Z/H]–Φ relation in extreme systems such as dwarf, ultra-diffuse and extremely compact (blue and red nugget) galaxies, as well as globular clusters, we can further test the origin of the relation and put tighter constraints on the strength and effectiveness of outflows in ejecting metals. Existing data from surveys such as the SAGES Legacy Unifying Globulars and GalaxieS survey (SLUGGS; Usher et al. 2012) and the multi-band photometric Systematically Measuring Ultra-diffuse Galaxies survey (SMUDGes; Zaritsky et al. 2019) can be used to test whether the relation between metallicity and the depth of the gravitational potential also exists in these systems with star-formation and assembly histories radically different from the sample used in this thesis. If our hypothesis of the gravitational potential regulating metal retention is correct these systems should still show a [Z/H]–Φ correlation. The slope and/or scatter of the relation in these extreme systems compared to more typical galaxies may reveal clues to their formation history.

5.2.3. Build-up of the Age–Surface Density Relation over Cosmic Time

The origin of the redshift-dependent surface-density threshold at which star-forming galaxies quench, which we infer from the age–surface density relation, remains unclear. To answer this question we need to look more closely at the redshift range between the low-redshift SAMI survey and the redshift range of LEGA-C ($0.60 \leq z \leq 0.76$). The presently ongoing Middle Ages Galaxy Properties with Integral Field spectroscopy (MAGPI; Foster et al. 2021) survey is observing galaxies in the intermediate redshift range of $0.25 \leq z \leq 0.35$. It will therefore provide a valuable sample to observe the age–surface density relation as it builds up from no correlation, as seen in LEGA-C at $z \sim 0.7$, to the strong correlation seen at $z \sim 0$. Furthermore, the MAGPI Survey has a strong simulations component, with the cosmological hydrodynamical simulations EAGLE (Schaye et al. 2015; Crain et al. 2015), Illustris-TNG (Pillepich et al. 2018; Naiman et al. 2018; Springel et al. 2018; Nelson et al. 2019), HORIZON-AGN (Dubois et al. 2016), and Magneticum (Teklu et al. 2015; Schulze et al. 2018), as well as the chemo-dynamical simulations of Taylor & Kobayashi (2015, 2017), all providing data that can be directly compared with MAGPI. Studying how age correlates with surface density in this crucial redshift range and comparing the observations to a wide variety of simulations should provide constraints on how star-formation and AGN feedback influences the stellar mass and size growth of galaxies.

5.3. Concluding Remarks

The way the age surface-density relation builds up suggests that quenching occurs without substantial structural change in the stellar distribution. The universality of the metallicity-potential relation poses strong constraints to theoretical models, precisely where our lack of physical understanding is most acute (e.g. stellar feedback, wind mass loading, dark-matter haloes). Understanding these issues will help clarify how the Universe we live in came to be, and how galaxies will continue to evolve over the next Hubble time.

Despite at times being somewhat confounding, these last four years of research have been incredibly rewarding. We followed a trail of interesting hypotheses and results that have, slowly but surely, furthered our understanding of this focused but significant aspect of galaxy evolution. With new observational surveys and improved simulations in progress, we can look forward to clarifying the remaining questions over the coming years.

Bibliography

Abazajian, K. N., et al. 2009, ApJS, 182, 543 (ADS entry)

Abbott, T. M. C., et al. 2021, ApJS, 255, 20 (ADS entry)

Allen, J. T., et al. 2015, MNRAS, 446, 1567 (ADS entry)

Almaini, O., et al. 2017, MNRAS, 472, 1401 (ADS entry)

Alpher, R. A., Bethe, H., & Gamow, G. 1948, Physical Review, 73, 803 (ADS entry)

Amorisco, N. C. 2017, MNRAS, 464, 2882 (ADS entry)

Anand, A., Nelson, D., & Kauffmann, G. 2021, MNRAS, 504, 65 (ADS entry)

Andrews, S. K., Driver, S. P., Davies, L. J. M., Kafle, P. R., Robotham, A. S. G., & Wright, A. H. 2017, MNRAS, 464, 1569 (ADS entry)

Baldwin, J. A., Phillips, M. M., & Terlevich, R. 1981, PASP, 93, 5 (ADS entry)

Balogh, M. L., Morris, S. L., Yee, H. K. C., Carlberg, R. G., & Ellingson, E. 1999, ApJ, 527, 54 (ADS entry)

Barone, T. M., D'Eugenio, F., Colless, M., & Scott, N. 2020, ApJ, 898, 62 (ADS entry)

Barone, T. M., et al. 2018, ApJ, 856, 64 (ADS entry)

—. 2022, MNRAS, 512, 3828 (ADS entry)

Barro, G., et al. 2013, ApJ, 765, 104 (ADS entry)

Bastian, N., Covey, K. R., & Meyer, M. R. 2010, ARA&A, 48, 339 (ADS entry)

Baum, W. A. 1959, PASP, 71, 106 (ADS entry)

Bell, E. F. 2003, ApJ, 586, 794 (ADS entry)

—. 2008, ApJ, 682, 355 (ADS entry)

Bell, E. F., et al. 2012, ApJ, 753, 167 (ADS entry)

Bennett, C. L., et al. 2003, ApJS, 148, 1 (ADS entry)

Bernardi, M., Sheth, R. K., Nichol, R. C., Schneider, D. P., & Brinkmann, J. 2005, AJ, 129, 61 (ADS entry)

Berndt, R. M. 1948, Oceania, 19, 16 (Link)

Bertone, G., & Tait, T. M. P. 2018, Nature, 562, 51 (ADS entry)

Bessel, F. W. 1838, MNRAS, 4, 152 (ADS entry)

Bezanson, R., van Dokkum, P. G., Tal, T., Marchesini, D., Kriek, M., Franx, M., & Coppi, P. 2009, ApJ, 697, 1290 (ADS entry)

Bland-Hawthorn, J., et al. 2011, Optics Express, 19, 2649 (ADS entry)

Bluck, A. F. L., Conselice, C. J., Buitrago, F., Grützbauch, R., Hoyos, C., Mortlock, A., & Bauer, A. E. 2012, ApJ, 747, 34 (ADS entry)

Bluck, A. F. L., Mendel, J. T., Ellison, S. L., Moreno, J., Simard, L., Patton, D. R., & Starkenburg, E. 2014, MNRAS, 441, 599 (ADS entry)

Boardman, N., et al. 2020, MNRAS, 498, 4943 (ADS entry)

Boecker, A., Leaman, R., van de Ven, G., Norris, M. A., Mackereth, J. T., & Crain, R. A. 2020, MNRAS, 491, 823 (ADS entry)

Boylan-Kolchin, M., & Ma, C.-P. 2007, MNRAS, 374, 1227 (ADS entry)

Brinchmann, J., Charlot, S., White, S. D. M., Tremonti, C., Kauffmann, G., Heckman, T., & Brinkmann, J. 2004, MNRAS, 351, 1151 (ADS entry)

Brüggen, M., & Kaiser, C. R. 2002, Nature, 418, 301 (ADS entry)

Bruzual, A. G. 1983, ApJ, 273, 105 (ADS entry)

Bruzual, G., & Charlot, S. 2003, MNRAS, 344, 1000 (ADS entry)

Bryant, J. J., Bland-Hawthorn, J., Fogarty, L. M. R., Lawrence, J. S., & Croom, S. M. 2014, MNRAS, 438, 869 (ADS entry)

Bryant, J. J., et al. 2015, MNRAS, 447, 2857 (ADS entry)

Bryant, J. J., et al. 2020, in Society of Photo-Optical Instrumentation Engineers (SPIE) Conference Series, Vol. 11447, Society of Photo-Optical Instrumentation Engineers (SPIE) Conference Series, 1144715 (ADS entry)

Buitrago, F., Trujillo, I., Conselice, C. J., Bouwens, R. J., Dickinson, M., & Yan, H. 2008, ApJ, 687, L61 (ADS entry)

Bundy, K., et al. 2015, ApJ, 798, 7 (ADS entry)

Burbidge, E. M., Burbidge, G. R., Fowler, W. A., & Hoyle, F. 1957, Reviews of Modern Physics, 29, 547 (ADS entry)

Calzetti, D. 2001, PASP, 113, 1449 (ADS entry)

—. 2013, Star Formation Rate Indicators (arXiv e-prints), 419 (ADS entry)

Calzetti, D., Armus, L., Bohlin, R. C., Kinney, A. L., Koornneef, J., & Storchi-Bergmann, T. 2000, ApJ, 533, 682 (ADS entry)

Cappellari, M. 2002, MNRAS, 333, 400 (ADS entry)

—. 2017, MNRAS, 466, 798 (ADS entry)

Cappellari, M., & Emsellem, E. 2004, PASP, 116, 138 (ADS entry)

Cappellari, M., Verolme, E. K., van der Marel, R. P., Verdoes Kleijn, G. A., Illingworth, G. D., Franx, M., Carollo, C. M., & de Zeeuw, P. T. 2002, ApJ, 578, 787 (ADS entry)

Cappellari, M., et al. 2006, Monthly Notices of the Royal Astronomical Society, 366, 1126

Cappellari, M., et al. 2011, MNRAS, 413, 813 (ADS entry)

—. 2012, Nature, 484, 485 (ADS entry)

—. 2013, MNRAS, 432, 1862

Ceverino, D., & Klypin, A. 2009, ApJ, 695, 292 (ADS entry)

Chabrier, G. 2003, PASP, 115, 763 (ADS entry)

Chang, Y.-Y., van der Wel, A., da Cunha, E., & Rix, H.-W. 2015, ApJS, 219, 8 (ADS entry)

Charlot, S., & Fall, S. M. 2000, ApJ, 539, 718 (ADS entry)

Charlot, S., Worthey, G., & Bressan, A. 1996, ApJ, 457, 625 (ADS entry)

Chauke, P., et al. 2018, ApJ, 861, 13 (ADS entry)

—. 2019, ApJ, 877, 48 (ADS entry)

Chen, Z., et al. 2020, ApJ, 897, 102 (ADS entry)

Cheung, E., et al. 2012, ApJ, 760, 131 (ADS entry)

Choi, J., Conroy, C., Moustakas, J., Graves, G. J., Holden, B. P., Brodwin, M., Brown, M. J. I., & van Dokkum, P. G. 2014, ApJ, 792, 95 (ADS entry)

Cimatti, A., et al. 2008, A&A, 482, 21 (ADS entry)

Cleveland, W. S., & Devlin, S. J. 1988, Journal of the American Statistical Association, 83, 596 (Link)

Cohn, J. D. 2018, MNRAS, 478, 2291 (ADS entry)

Conroy, C. 2013, ARA&A, 51, 393 (ADS entry)

Conroy, C., Gunn, J. E., & White, M. 2009, ApJ, 699, 486 (ADS entry)

Conroy, C., & van Dokkum, P. 2012a, ApJ, 747, 69 (ADS entry)

Conroy, C., & van Dokkum, P. G. 2012b, The Astrophysical Journal, 760, 71 (ADS entry)

Cook, B. A., Conroy, C., Pillepich, A., Rodriguez-Gomez, V., & Hernquist, L. 2016, ApJ, 833, 158 (ADS entry)

Cortese, L., et al. 2016, MNRAS, 463, 170 (ADS entry)

Crain, R. A., et al. 2015, MNRAS, 450, 1937 (ADS entry)

Croom, S. M., et al. 2012, MNRAS, 421, 872 (ADS entry)

—. 2021a, MNRAS, 505, 2247 (ADS entry)

—. 2021b, MNRAS, 505, 991 (ADS entry)

Curtis, H. D. 1917, PASP, 29, 206 (ADS entry)

da Cunha, E., Charlot, S., & Elbaz, D. 2008, MNRAS, 388, 1595 (ADS entry)

Daddi, E., et al. 2007, ApJ, 670, 156 (ADS entry)

—. 2010, ApJ, 713, 686 (ADS entry)

Davies, L. J. M., et al. 2015, MNRAS, 447, 1014 (ADS entry)

de Graaff, A., et al. 2020, ApJ, 903, L30 (ADS entry)

—. 2021, ApJ, 913, 103 (ADS entry)

De Lucia, G., et al. 2007, MNRAS, 374, 809 (ADS entry)

Dekel, A., et al. 2009, Nature, 457, 451 (ADS entry)

D'Eugenio, F., Colless, M., Groves, B., Bian, F., & Barone, T. M. 2018, MNRAS, 479, 1807 (ADS entry)

D'Eugenio, F., et al. 2020, MNRAS, 497, 389 (ADS entry)

Di Matteo, P., Pipino, A., Lehnert, M. D., Combes, F., & Semelin, B. 2009, A&A, 499, 427 (ADS entry)

Díaz-García, L. A., et al. 2019, A&A, 631, A158 (ADS entry)

Diemer, B., Sparre, M., Abramson, L. E., & Torrey, P. 2017, ApJ, 839, 26 (ADS entry)

Dopita, M. A. 1976, ApJ, 209, 395 (ADS entry)

Dopita, M. A., & Sutherland, R. S. 2003, Astrophysics of the diffuse universe (Springer) (ADS entry)

Doroshkevich, A. G. 1970, Astrofizika, 6, 581 (ADS entry)

Dressler, A., & Gunn, J. E. 1983, ApJ, 270, 7 (ADS entry)

Dressler, A., Smail, I., Poggianti, B. M., Butcher, H., Couch, W. J., Ellis, R. S., & Oemler, Augustus, J. 1999, ApJS, 122, 51 (ADS entry)

Driver, S. P., et al. 2011, MNRAS, 413, 971 (ADS entry)

—. 2018, MNRAS, 475, 2891 (ADS entry)

Dubois, Y., Peirani, S., Pichon, C., Devriendt, J., Gavazzi, R., Welker, C., & Volonteri, M. 2016, MNRAS, 463, 3948 (ADS entry)

Einstein, A. 1916, Annalen der Physik, 354, 769 (ADS entry)

—. 1917, Sitzungsberichte der Königlich Preußischen Akademie der Wissenschaften (Berlin, 142 (ADS entry)

Eldridge, J. J., Stanway, E. R., Xiao, L., McClelland , L. A. S., Taylor, G., Ng, M., Greis, S. M. L., & Bray, J. C. 2017, PASA, 34, e058 (ADS entry)

Epinat, B., et al. 2012, A&A, 539, A92 (ADS entry)

Faber, S. M. 1973, ApJ, 179, 731 (ADS entry)

Faber, S. M., Friel, E. D., Burstein, D., & Gaskell, C. M. 1985, ApJS, 57, 711 (ADS entry)

Faisst, A. L., Capak, P. L., Emami, N., Tacchella, S., & Larson, K. L. 2019, ApJ, 884, 133 (ADS entry)

Falcón-Barroso, J., Sánchez-Blázquez, P., Vazdekis, A., Ricciardelli, E., Cardiel, N., Cenarro, A. J., Gorgas, J., & Peletier, R. F. 2011, A&A, 532, A95

Faucher-Giguère, C.-A. 2018, MNRAS, 473, 3717 (ADS entry)

Federrath, C., et al. 2017, MNRAS, 468, 3965 (ADS entry)

Ferguson, H. C., et al. 2004, ApJ, 600, L107 (ADS entry)

Ferreras, I., et al. 2019, MNRAS, 489, 608 (ADS entry)

Foreman-Mackey, D., Hogg, D. W., Lang, D., & Goodman, J. 2013, PASP, 125, 306 (ADS entry)

Förster Schreiber, N. M., et al. 2006, ApJ, 645, 1062 (ADS entry)

—. 2009, ApJ, 706, 1364 (ADS entry)

Foster, C., et al. 2021, PASA, 38, e031 (ADS entry)

Franx, M., & Illingworth, G. 1990, ApJ, 359, L41 (ADS entry)

Franx, M., van Dokkum, P. G., Förster Schreiber, N. M., Wuyts, S., Labbé, I., & Toft, S. 2008, ApJ, 688, 770 (ADS entry)

Freeman, K. C. 1970, ApJ, 160, 811 (ADS entry)

Friedmann, A. 1924, Zeitschrift fur Physik, 21, 326 (ADS entry)

Gallazzi, A., Bell, E. F., Zibetti, S., Brinchmann, J., & Kelson, D. D. 2014, The Astrophysical Journal, 788, 25

Gallazzi, A., Charlot, S., Brinchmann, J., & White, S. D. M. 2006, MNRAS, 370, 1106 (ADS entry)

Gallazzi, A., Charlot, S., Brinchmann, J., White, S. D. M., & Tremonti, C. A. 2005, MNRAS, 362, 41 (ADS entry)

Gamow, G. 1946, Physical Review, 70, 572 (ADS entry)

Ganda, K., et al. 2007, MNRAS, 380, 506 (ADS entry)

García-Burillo, S., et al. 2014, A&A, 567, A125 (ADS entry)

Genel, S., et al. 2014, MNRAS, 445, 175 (ADS entry)

Girardi, L., Bressan, A., Bertelli, G., & Chiosi, C. 2000, A&AS, 141, 371 (ADS entry)

Gladders, M. D., Oemler, A., Dressler, A., Poggianti, B., Vulcani, B., & Abramson, L. 2013, ApJ, 770, 64 (ADS entry)

Goddard, D., et al. 2017, MNRAS, 465, 688 (ADS entry)

González Delgado, R. M., et al. 2014, A&A, 562, A47 (ADS entry)

—. 2015, A&A, 581, A103 (ADS entry)

Goodman, J., & Weare, J. 2010, Communications in Applied Mathematics and Computational Science, Vol. 5, No. 1, p. 65-80, 2010, 5, 65 (ADS entry)

Graves, G. J., Faber, S. M., & Schiavon, R. P. 2009a, ApJ, 693, 486 (ADS entry)

—. 2009b, ApJ, 698, 1590 (ADS entry)

Green, A. W., et al. 2018, MNRAS, 475, 716 (ADS entry)

Greene, J. E., et al. 2019, ApJ, 874, 66 (ADS entry)

Greggio, L., & Renzini, A. 1983, A&A, 118, 217 (ADS entry)

Gunn, J. E., & Gott, J. Richard, I. 1972, ApJ, 176, 1 (ADS entry)

Guo, Y., et al. 2016, ApJ, 833, 37 (ADS entry)

Guth, A. H. 1981, Phys. Rev. D, 23, 347 (ADS entry)

Hamacher, D. W. 2018, The Australian Journal of Anthropology, 29, 89 (ADS entry)

Hamacher, D. W., & Banks, K. 2018, arXiv e-prints, arXiv:1806.02462 (ADS entry)

Hamacher, D. W., Barsa, J., Passi, S., & Tapim, A. 2019, Proc. R. Soc. Vic., 131, 24 (Link)

Hamacher, D. W., & Frew, D. J. 2010, Journal of Astronomical History and Heritage, 13, 220 (ADS entry)

Hamacher, D. W., & Norris, R. P. 2010, WGN, Journal of the International Meteor Organization, 38, 87 (ADS entry)

—. 2011a, Journal of Astronomical History and Heritage, 14, 31 (ADS entry)

—. 2011b, Journal of Astronomical History and Heritage, 14, 103 (ADS entry)

Hao, C.-N., Kennicutt, R. C., Johnson, B. D., Calzetti, D., Dale, D. A., & Moustakas, J. 2011, ApJ, 741, 124 (ADS entry)

Hertzsprung, E. 1911, Publikationen des Astrophysikalischen Observatoriums zu Potsdam, 63 (ADS entry)

Hill, D. T., et al. 2011, MNRAS, 412, 765 (ADS entry)

Hinshaw, G., et al. 2009, ApJS, 180, 225 (ADS entry)

Hirschmann, M., Naab, T., Ostriker, J. P., Forbes, D. A., Duc, P.-A., Davé, R., Oser, L., & Karabal, E. 2015, MNRAS, 449, 528 (ADS entry)

Hogg, D. W., Bovy, J., & Lang, D. 2010, arXiv e-prints, arXiv:1008.4686 (ADS entry)

Hopkins, P. F., Bundy, K., Murray, N., Quataert, E., Lauer, T. R., & Ma, C.-P. 2009, MNRAS, 398, 898 (ADS entry)

Hubble, E. 1929a, Proceedings of the National Academy of Science, 15, 168 (ADS entry)

Hubble, E. P. 1929b, ApJ, 69, 103 (ADS entry)

Jeffreys, H. 1946, Proc. R. Soc. Lond., 186, 453–461

Johansson, P. H., Naab, T., & Ostriker, J. P. 2012, ApJ, 754, 115 (ADS entry)

Jorgensen, I. 1997, MNRAS, 288, 161 (ADS entry)

Kassin, S. A., et al. 2012, ApJ, 758, 106 (ADS entry)

Kauffmann, G., Heckman, T. M., De Lucia, G., Brinchmann, J., Charlot, S., Tremonti, C., White, S. D. M., & Brinkmann, J. 2006, MNRAS, 367, 1394 (ADS entry)

Kauffmann, G., White, S. D. M., Heckman, T. M., Ménard, B., Brinchmann, J., Charlot, S., Tremonti, C., & Brinkmann, J. 2004, MNRAS, 353, 713 (ADS entry)

Kauffmann, G., et al. 2003a, MNRAS, 341, 33 (ADS entry)

—. 2003b, MNRAS, 341, 54 (ADS entry)

—. 2003c, MNRAS, 346, 1055 (ADS entry)

Kelvin, L. S., et al. 2012, MNRAS, 421, 1007 (ADS entry)

—. 2014, MNRAS, 444, 1647 (ADS entry)

Kennicutt, R. C., & Evans, N. J. 2012, ARA&A, 50, 531 (ADS entry)

Kennicutt, Jr., R. C. 1998, ApJ, 498, 541 (ADS entry)

Kewley, L. J., Dopita, M. A., Sutherland, R. S., Heisler, C. A., & Trevena, J. 2001, ApJ, 556, 121 (ADS entry)

Kirshner, R. P. 1991, QJRAS, 32, 233 (ADS entry)

Kish, George, . 1978, A Source book in geography (Cambridge) (Link)

Kobayashi, C. 2004, MNRAS, 347, 740 (ADS entry)

Kormendy, J., & Ho, L. C. 2013, ARA&A, 51, 511 (ADS entry)

Kriek, M., van Dokkum, P. G., Franx, M., Illingworth, G. D., & Magee, D. K. 2009, ApJ, 705, L71 (ADS entry)

Kriek, M., van Dokkum, P. G., Whitaker, K. E., Labbé, I., Franx, M., & Brammer, G. B. 2011, ApJ, 743, 168 (ADS entry)

Kroupa, P. 2001, MNRAS, 322, 231 (ADS entry)

La Barbera, F., Ferreras, I., Vazdekis, A., de la Rosa, I. G., de Carvalho, R. R., Trevisan, M., Falcón-Barroso, J., & Ricciardelli, E. 2013, MNRAS, 433, 3017 (ADS entry)

Labbé, I., et al. 2005, ApJ, 624, L81 (ADS entry)

Lambas, D. G., Alonso, S., Mesa, V., & O'Mill, A. L. 2012, A&A, 539, A45 (ADS entry)

Lang, P., et al. 2014, ApJ, 788, 11 (ADS entry)

Law, D. R., Steidel, C. C., Erb, D. K., Larkin, J. E., Pettini, M., Shapley, A. E., & Wright, S. A. 2007, ApJ, 669, 929 (ADS entry)

—. 2009, ApJ, 697, 2057 (ADS entry)

Le Fèvre, O., et al. 2003, in Society of Photo-Optical Instrumentation Engineers (SPIE) Conference Series, Vol. 4841, Instrument Design and Performance for Optical/Infrared Ground-based Telescopes, ed. M. Iye & A. F. M. Moorwood, 1670–1681 (ADS entry)

Lee, H.-c., Worthey, G., Trager, S. C., & Faber, S. M. 2007, ApJ, 664, 215 (ADS entry)

Leja, J., Carnall, A. C., Johnson, B. D., Conroy, C., & Speagle, J. S. 2019, ApJ, 876, 3 (ADS entry)

Lemaître, G. 1927, Annales de la Société; Scientifique de Bruxelles, 47, 49 (ADS entry)

—. 1931, Nature, 127, 706 (ADS entry)

Leslie, S. K., et al. 2020, ApJ, 899, 58 (ADS entry)

Li, H., et al. 2017, ApJ, 838, 77 (ADS entry)

—. 2018, MNRAS, 476, 1765 (ADS entry)

Li, Z., & Han, Z. 2007, A&A, 471, 795 (ADS entry)

Lian, J., Thomas, D., Maraston, C., Goddard, D., Comparat, J., Gonzalez-Perez, V., & Ventura, P. 2018, MNRAS, 474, 1143 (ADS entry)

Lilly, S., et al. 1998, ApJ, 500, 75 (ADS entry)

Lilly, S. J., & Carollo, C. M. 2016, ApJ, 833, 1 (ADS entry)

Lilly, S. J., Le Fevre, O., Hammer, F., & Crampton, D. 1996, ApJ, 460, L1 (ADS entry)

Linde, A. D. 1982, Physics Letters B, 108, 389 (ADS entry)

Liu, Y., et al. 2016, ApJ, 818, 179 (ADS entry)

Madau, P., & Dickinson, M. 2014, ARA&A, 52, 415 (ADS entry)

Madau, P., Pozzetti, L., & Dickinson, M. 1998, ApJ, 498, 106 (ADS entry)

Magoulas, C., et al. 2012, MNRAS, 427, 245 (ADS entry)

Maiolino, R., et al. 2020, The Messenger, 180, 24 (ADS entry)

Malmquist, K. G. 1922, Meddelanden fran Lunds Astronomiska Observatorium Serie I, 100, 1 (ADS entry)

Marks, M., Kroupa, P., Dabringhausen, J., & Pawlowski, M. S. 2012, MNRAS, 422, 2246 (ADS entry)

Martín-Navarro, I., Brodie, J. P., van den Bosch, R. C. E., Romanowsky, A. J., & Forbes, D. A. 2016, ApJ, 832, L11 (ADS entry)

Martín-Navarro, I., La Barbera, F., Vazdekis, A., Falcón-Barroso, J., & Ferreras, I. 2015a, MNRAS, 447, 1033 (ADS entry)

Martín-Navarro, I., Vazdekis, A., Falcón-Barroso, J., La Barbera, F., Yıldırım, A., & van de Ven, G. 2018, MNRAS, 475, 3700 (ADS entry)

Martín-Navarro, I., et al. 2015b, ApJ, 806, L31 (ADS entry)

—. 2019, A&A, 626, A124 (ADS entry)

Matteucci, F. 1994, A&A, 288, 57 (ADS entry)

—. 2012, Chemical Evolution of Galaxies (Springer) (ADS entry)

Matteucci, F., & Greggio, L. 1986, A&A, 154, 279 (ADS entry)

McDermid, R. M., et al. 2015, MNRAS, 448, 3484 (ADS entry)

McKee, C. F., & Ostriker, J. P. 1977, ApJ, 218, 148 (ADS entry)

McLure, R. J., et al. 2018, MNRAS, 479, 25 (ADS entry)

Medling, A. M., et al. 2018, MNRAS, 475, 5194 (ADS entry)

Mei, S., et al. 2006, ApJ, 639, 81 (ADS entry)

Møller, P., & Christensen, L. 2020, MNRAS, 492, 4805 (ADS entry)

Moore, B., Katz, N., Lake, G., Dressler, A., & Oemler, A. 1996, Nature, 379, 613 (ADS entry)

Morokuma-Matsui, K., & Baba, J. 2015, MNRAS, 454, 3792 (ADS entry)

Mortlock, A., McLure, R. J., Bowler, R. A. A., McLeod, D. J., Mármol-Queraltó, E., Parsa, S., Dunlop, J. S., & Bruce, V. A. 2017, MNRAS, 465, 672 (ADS entry)

Mowla, L. A., et al. 2019, ApJ, 880, 57 (ADS entry)

Murphy, E. J., et al. 2011, ApJ, 737, 67 (ADS entry)

Muzzin, A., et al. 2013a, ApJS, 206, 8 (ADS entry)

—. 2013b, ApJ, 777, 18 (ADS entry)

Naab, T., Johansson, P. H., & Ostriker, J. P. 2009, ApJ, 699, L178 (ADS entry)

Naiman, J. P., et al. 2018, MNRAS, 477, 1206 (ADS entry)

Navarro, J. F., Frenk, C. S., & White, S. D. M. 1996, ApJ, 462, 563 (ADS entry)

Nelan, J. E., Smith, R. J., Hudson, M. J., Wegner, G. A., Lucey, J. R., Moore, S. A. W., Quinney, S. J., & Suntzeff, N. B. 2005, ApJ, 632, 137 (ADS entry)

Nelson, D., et al. 2019, MNRAS, 490, 3234 (ADS entry)

Newton, I. 1687, Philosophiae Naturalis Principia Mathematica. Auctore Js. Newton (Londini : Jussu Societatis Regiae ac Typis Josephi Streater) (ADS entry)

Norris, M. A., Escudero, C. G., Faifer, F. R., Kannappan, S. J., Forte, J. C., & van den Bosch, R. C. E. 2015, MNRAS, 451, 3615 (ADS entry)

Norris, R. P. 2016, PASA, 33, e039 (ADS entry)

Norris, R. P., & Hamacher, D. W. 2015, Australian Aboriginal Astronomy - An Overview (Springer), 2215 (ADS entry)

Omand, C. M. B., Balogh, M. L., & Poggianti, B. M. 2014, MNRAS, 440, 843 (ADS entry)

Oogi, T., & Habe, A. 2013, MNRAS, 428, 641 (ADS entry)

Oser, L., Naab, T., Ostriker, J. P., & Johansson, P. H. 2012, ApJ, 744, 63 (ADS entry)

Oser, L., Ostriker, J. P., Naab, T., Johansson, P. H., & Burkert, A. 2010, ApJ, 725, 2312 (ADS entry)

Osterbrock, D. E., & Ferland, G. J. 2006, Astrophysics of gaseous nebulae and active galactic nuclei (University Science Books) (ADS entry)

Owers, M. S., et al. 2017, MNRAS, 468, 1824 (ADS entry)

Ownsworth, J. R., Conselice, C. J., Mortlock, A., Hartley, W. G., Almaini, O., Duncan, K., & Mundy, C. J. 2014, MNRAS, 445, 2198 (ADS entry)

Pagel, B. E. J., & Tautvaisiene, G. 1995, MNRAS, 276, 505 (ADS entry)

Pak, M., et al. 2021, ApJ, 906, 43 (ADS entry)

Parikh, T., et al. 2018, MNRAS, 477, 3954 (ADS entry)

Peacock, J. A., et al. 2001, Nature, 410, 169 (ADS entry)

Peletier, R. F., et al. 2007, MNRAS, 379, 445 (ADS entry)

Peng, C. Y., Ho, L. C., Impey, C. D., & Rix, H.-W. 2010, AJ, 139, 2097 (ADS entry)

Penzias, A. A., & Wilson, R. W. 1965, ApJ, 142, 419 (ADS entry)

Percival, W. J., et al. 2001, MNRAS, 327, 1297 (ADS entry)

Perlmutter, S., et al. 1999, ApJ, 517, 565 (ADS entry)

Pietrinferni, A., Cassisi, S., Salaris, M., & Castelli, F. 2004, ApJ, 612, 168 (ADS entry)

—. 2006, ApJ, 642, 797 (ADS entry)

Pillepich, A., et al. 2014, MNRAS, 444, 237 (ADS entry)

—. 2018, MNRAS, 475, 648 (ADS entry)

Pipino, A., D'Ercole, A., Chiappini, C., & Matteucci, F. 2010, MNRAS, 407, 1347 (ADS entry)

Planck Collaboration et al. 2020a, A&A, 641, A6 (ADS entry)

—. 2020b, A&A, 641, A10 (ADS entry)

Poggianti, B. M., & Barbaro, G. 1997, A&A, 325, 1025 (ADS entry)

Pointon, S. K., Kacprzak, G. G., Nielsen, N. M., Muzahid, S., Murphy, M. T., Churchill, C. W., & Charlton, J. C. 2019, ApJ, 883, 78 (ADS entry)

Press, W. H., Flannery, B. P., Teukolsky, S. A., Vetterling, W. T., & Gould, H. 1987, American Journal of Physics, 55, 90 (Link)

Press, W. H., Teukolsky, S. A., Vetterling, W. T., & Flannery, B. P. 1992, Numerical Recipes in FORTRAN (2Nd Ed.): The Art of Scientific Computing (New York, NY, USA: Cambridge University Press)

Price, K., Storn, R. M., & Lampinen, J. A. 2005, Differential Evolution – A practical approach to global optimization (Springer Berlin, Heidelberg)

Prochaska, J. X., et al. 2017, ApJ, 837, 169 (ADS entry)

Ranalli, P., Comastri, A., & Setti, G. 2003, A&A, 399, 39 (ADS entry)

Ravindranath, S., et al. 2004, ApJ, 604, L9 (ADS entry)

Reichard, T. A., Heckman, T. M., Rudnick, G., Brinchmann, J., Kauffmann, G., & Wild, V. 2009, ApJ, 691, 1005 (ADS entry)

Renzini, A., & Peng, Y.-j. 2015, ApJ, 801, L29 (ADS entry)

Riess, A. G., Casertano, S., Yuan, W., Macri, L. M., & Scolnic, D. 2019, ApJ, 876, 85 (ADS entry)

Riess, A. G., et al. 1998, AJ, 116, 1009 (ADS entry)

Robaina, A. R., Hoyle, B., Gallazzi, A., Jiménez, R., van der Wel, A., & Verde, L. 2012, MNRAS, 427, 3006 (ADS entry)

Robertson, H. P. 1928, The London, Edinburgh, and Dublin Philosophical Magazine and Journal of Science, 5, 835 (Link)

Rodriguez-Gomez, V., et al. 2016, MNRAS, 458, 2371 (ADS entry)

Rogers, A. B., et al. 2014, MNRAS, 440, 3714 (ADS entry)

Rose, J. A. 1985, AJ, 90, 1927 (ADS entry)

—. 1994, AJ, 107, 206 (ADS entry)

Rubin, V. C., & Ford, W. Kent, J. 1970, ApJ, 159, 379 (ADS entry)

Russell, H. N. 1914, Popular Astronomy, 22, 275 (ADS entry)

Said, K., Colless, M., Magoulas, C., Lucey, J. R., & Hudson, M. J. 2020, MNRAS, 497, 1275 (ADS entry)

Sakamoto, K., Aalto, S., Combes, F., Evans, A., & Peck, A. 2014, ApJ, 797, 90 (ADS entry)

Salim, S., et al. 2007, ApJS, 173, 267 (ADS entry)

Salpeter, E. E. 1955, ApJ, 121, 161 (ADS entry)

Sánchez-Blázquez, P., Gorgas, J., Cardiel, N., & González, J. J. 2006a, A&A, 457, 809 (ADS entry)

Sánchez-Blázquez, P., et al. 2006b, MNRAS, 371, 703 (ADS entry)

—. 2014, A&A, 570, A6 (ADS entry)

Sandage, A. 1972, ApJ, 176, 21 (ADS entry)

Schawinski, K., Thomas, D., Sarzi, M., Maraston, C., Kaviraj, S., Joo, S.-J., Yi, S. K., & Silk, J. 2007a, MNRAS, 382, 1415 (ADS entry)

Schawinski, K., et al. 2007b, ApJS, 173, 512 (ADS entry)

Schaye, J., et al. 2015, MNRAS, 446, 521 (ADS entry)

Schiavon, R. P. 2007, ApJS, 171, 146 (ADS entry)

Schmidt, M. 1959, ApJ, 129, 243 (ADS entry)

Schulze, F., Remus, R.-S., Dolag, K., Burkert, A., Emsellem, E., & van de Ven, G. 2018, MNRAS, 480, 4636 (ADS entry)

Scott, N., et al. 2009, MNRAS, 398, 1835 (ADS entry)

—. 2013, MNRAS, 432, 1894 (ADS entry)

—. 2017, MNRAS, 472, 2833 (ADS entry)

—. 2018, MNRAS, 481, 2299 (ADS entry)

Scoville, N., et al. 2007, ApJS, 172, 38 (ADS entry)

Selin, H., & Sun, X. 2000, Astronomy across cultures : the history of non-Western astronomy (Springer; 2000th edition) (ADS entry)

Sellwood, J. A., & Binney, J. J. 2002, MNRAS, 336, 785 (ADS entry)

Serra, P., & Trager, S. C. 2007, MNRAS, 374, 769 (ADS entry)

Sersic, J. L. 1968, Atlas de Galaxias Australes (Observatorio Astronomico, Universidad Nacional de Cordoba) (ADS entry)

Shapley, H., & Curtis, H. D. 1921, Bulletin of the National Research Council, 2, 171 (ADS entry)

Shapley, H., & Shapley, M. B. 1919, ApJ, 50, 107 (ADS entry)

Sharp, R., et al. 2006, in Proc. SPIE, Vol. 6269, Society of Photo-Optical Instrumentation Engineers (SPIE) Conference Series, 62690G (ADS entry)

Sharp, R., et al. 2015, MNRAS, 446, 1551 (ADS entry)

Shen, S., Madau, P., Guedes, J., Mayer, L., Prochaska, J. X., & Wadsley, J. 2013, ApJ, 765, 89 (ADS entry)

Shen, S., Mo, H. J., White, S. D. M., Blanton, M. R., Kauffmann, G., Voges, W., Brinkmann, J., & Csabai, I. 2003, MNRAS, 343, 978 (ADS entry)

Shull, J. M., & McKee, C. F. 1979, ApJ, 227, 131 (ADS entry)

Simard, L., Mendel, J. T., Patton, D. R., Ellison, S. L., & McConnachie, A. W. 2011, ApJS, 196, 11 (ADS entry)

Smoot, G. F., et al. 1992, ApJ, 396, L1 (ADS entry)

Spiniello, C., Trager, S., Koopmans, L. V. E., & Conroy, C. 2014, Monthly Notices of the Royal Astronomical Society, 438, 1483 (ADS entry)

Springel, V., et al. 2018, MNRAS, 475, 676 (ADS entry)

Stanway, E. R., & Eldridge, J. J. 2018, MNRAS, 479, 75 (ADS entry)

Storn, R., & Price, K. 1997, Journal of Global Optimization, 11, 341 (Link)

Stott, J. P., et al. 2016, MNRAS, 457, 1888 (ADS entry)

Straatman, C. M. S., et al. 2018, ApJS, 239, 27 (ADS entry)

Strauss, M. A., et al. 2002, The Astronomical Journal, 124, 1810 (ADS entry)

Strigari, L. E., Bullock, J. S., Kaplinghat, M., Simon, J. D., Geha, M., Willman, B., & Walker, M. G. 2008, Nature, 454, 1096 (ADS entry)

Swinbank, A. M., Smail, I., Sobral, D., Theuns, T., Best, P. N., & Geach, J. E. 2012, ApJ, 760, 130 (ADS entry)

Szomoru, D., Franx, M., & van Dokkum, P. G. 2012, ApJ, 749, 121 (ADS entry)

Tacconi, L. J., et al. 2010, Nature, 463, 781 (ADS entry)

—. 2013, ApJ, 768, 74 (ADS entry)

Tantalo, R., Chiosi, C., & Bressan, A. 1998, A&A, 333, 419 (ADS entry)

Taylor, E. N., et al. 2011, MNRAS, 418, 1587 (ADS entry)

Taylor, P., & Kobayashi, C. 2015, MNRAS, 448, 1835 (ADS entry)

—. 2017, MNRAS, 471, 3856 (ADS entry)

Tegmark, M., et al. 2006, Phys. Rev. D, 74, 123507 (ADS entry)

Teklu, A. F., Remus, R.-S., Dolag, K., Beck, A. M., Burkert, A., Schmidt, A. S., Schulze, F., & Steinborn, L. K. 2015, ApJ, 812, 29 (ADS entry)

Thomas, D., Greggio, L., & Bender, R. 1998, MNRAS, 296, 119 (ADS entry)

Thomas, D., Maraston, C., Bender, R., & Mendes de Oliveira, C. 2005, ApJ, 621, 673 (ADS entry)

Thomas, D., Maraston, C., & Johansson, J. 2011, MNRAS, 412, 2183 (ADS entry)

Thomas, D., Maraston, C., Schawinski, K., Sarzi, M., & Silk, J. 2010, MNRAS, 404, 1775 (ADS entry)

Thomas, D., et al. 2013, MNRAS, 431, 1383 (ADS entry)

Tinsley, B. M. 1980, Fund. Cosmic Phys., 5, 287 (ADS entry)

Trager, S. C., Faber, S. M., Worthey, G., & González, J. J. 2000a, AJ, 120, 165 (ADS entry)

—. 2000b, AJ, 119, 1645 (ADS entry)

Trager, S. C., & Somerville, R. S. 2009, MNRAS, 395, 608 (ADS entry)

Trager, S. C., Worthey, G., Faber, S. M., Burstein, D., & González, J. J. 1998, ApJS, 116, 1 (ADS entry)

Tripicco, M. J., & Bell, R. A. 1995, AJ, 110, 3035 (ADS entry)

Trujillo, I., Conselice, C. J., Bundy, K., Cooper, M. C., Eisenhardt, P., & Ellis, R. S. 2007, MNRAS, 382, 109 (ADS entry)

Trujillo, I., et al. 2006, ApJ, 650, 18 (ADS entry)

Tsujimoto, T., Nomoto, K., Yoshii, Y., Hashimoto, M., Yanagida, S., & Thielemann, F. K. 1995, MNRAS, 277, 945 (ADS entry)

Tumlinson, J., Peeples, M. S., & Werk, J. K. 2017, ARA&A, 55, 389 (ADS entry)

Usher, C., et al. 2012, MNRAS, 426, 1475 (ADS entry)

van de Sande, J., et al. 2017, ApJ, 835, 104 (ADS entry)

—. 2018, Nature Astronomy, 2, 483 (ADS entry)

—. 2021, MNRAS, 505, 3078 (ADS entry)

van den Bergh, S. 1976, ApJ, 206, 883 (ADS entry)

van der Wel, A., Bell, E. F., van den Bosch, F. C., Gallazzi, A., & Rix, H.-W. 2009, ApJ, 698, 1232 (ADS entry)

van der Wel, A., Holden, B. P., Zirm, A. W., Franx, M., Rettura, A., Illingworth, G. D., & Ford, H. C. 2008, ApJ, 688, 48 (ADS entry)

van der Wel, A., et al. 2012, ApJS, 203, 24 (ADS entry)

—. 2014, ApJ, 788, 28 (ADS entry)

—. 2016, ApJS, 223, 29 (ADS entry)

—. 2021, ApJS, 256, 44 (ADS entry)

van Dokkum, P., Conroy, C., Villaume, A., Brodie, J., & Romanowsky, A. J. 2017, ApJ, 841, 68 (ADS entry)

van Dokkum, P. G., & Conroy, C. 2010, Nature, 468, 940 (ADS entry)

van Dokkum, P. G., et al. 2008, ApJ, 677, L5 (ADS entry)

—. 2010, ApJ, 709, 1018 (ADS entry)

—. 2011, ApJ, 743, L15 (ADS entry)

—. 2015, ApJ, 813, 23 (ADS entry)

Vaughan, S. P., Davies, R. L., Zieleniewski, S., & Houghton, R. C. W. 2018, MNRAS, 479, 2443 (ADS entry)

Vazdekis, A., Koleva, M., Ricciardelli, E., Röck, B., & Falcón-Barroso, J. 2016, MNRAS, 463, 3409 (ADS entry)

Vazdekis, A., Sánchez-Blázquez, P., Falcón-Barroso, J., Cenarro, A. J., Beasley, M. A., Cardiel, N., Gorgas, J., & Peletier, R. F. 2010, MNRAS, 404, 1639 (ADS entry)

Vazdekis, A., et al. 2015, MNRAS, 449, 1177 (ADS entry)

Veilleux, S., & Osterbrock, D. E. 1987, ApJS, 63, 295 (ADS entry)

Vincenzo, F., Matteucci, F., Belfiore, F., & Maiolino, R. 2016, MNRAS, 455, 4183 (ADS entry)

Virtanen, P., et al. 2020, Nature Methods, 17, 261 (ADS entry)

Visvanathan, N., & Sandage, A. 1977, ApJ, 216, 214 (ADS entry)

Vogelsberger, M., et al. 2014, MNRAS, 444, 1518 (ADS entry)

Wake, D. A., van Dokkum, P. G., & Franx, M. 2012, ApJ, 751, L44 (ADS entry)

Walker, A. G. 1937, Proceedings of the London Mathematical Society, 42, 90 (ADS entry)

Weiner, B. J., et al. 2006, ApJ, 653, 1027 (ADS entry)

Wellons, S., et al. 2015, MNRAS, 449, 361 (ADS entry)

—. 2016, MNRAS, 456, 1030 (ADS entry)

Whitaker, K. E., van Dokkum, P. G., Brammer, G., & Franx, M. 2012, ApJ, 754, L29 (ADS entry)

Whitaker, K. E., et al. 2017, ApJ, 838, 19 (ADS entry)

White, S. D. M. 1984, ApJ, 286, 38 (ADS entry)

White, S. D. M., & Rees, M. J. 1978, MNRAS, 183, 341 (ADS entry)

Williams, R. J., Quadri, R. F., Franx, M., van Dokkum, P., Toft, S., Kriek, M., & Labbé, I. 2010, ApJ, 713, 738 (ADS entry)

Wisnioski, E., et al. 2011, MNRAS, 417, 2601 (ADS entry)

—. 2015, ApJ, 799, 209 (ADS entry)

—. 2019, ApJ, 886, 124 (ADS entry)

Woo, J., Carollo, C. M., Faber, S. M., Dekel, A., & Tacchella, S. 2017, MNRAS, 464, 1077 (ADS entry)

Woo, J., Dekel, A., Faber, S. M., & Koo, D. C. 2015, MNRAS, 448, 237 (ADS entry)

Woo, J., & Ellison, S. L. 2019, MNRAS, 487, 1927 (ADS entry)

Worthey, G. 1992, PhD thesis, California Univ., Santa Cruz. (ADS entry)

—. 1994, ApJS, 95, 107 (ADS entry)

Worthey, G., Faber, S. M., & Gonzalez, J. J. 1992, ApJ, 398, 69 (ADS entry)

Worthey, G., Faber, S. M., Gonzalez, J. J., & Burstein, D. 1994, ApJS, 94, 687 (ADS entry)

Worthey, G., & Ottaviani, D. L. 1997, ApJS, 111, 377 (ADS entry)

Wright, E. L., et al. 2010, AJ, 140, 1868 (ADS entry)

Wright, S. A., Larkin, J. E., Law, D. R., Steidel, C. C., Shapley, A. E., & Erb, D. K. 2009, ApJ, 699, 421 (ADS entry)

Wu, P.-F., et al. 2018, ApJ, 868, 37 (ADS entry)

—. 2020, ApJ, 888, 77 (ADS entry)

Wuyts, S., et al. 2011, ApJ, 742, 96 (ADS entry)

Yano, M., Kriek, M., van der Wel, A., & Whitaker, K. E. 2016, ApJ, 817, L21 (ADS entry)

Yi, S. K. 2003, ApJ, 582, 202 (ADS entry)

York, D. G., et al. 2000, AJ, 120, 1579 (ADS entry)

Zaritsky, D., et al. 2019, ApJS, 240, 1 (ADS entry)

Zolotov, A., et al. 2015, MNRAS, 450, 2327 (ADS entry)

Zwicky, F. 1937, ApJ, 86, 217 (ADS entry)